PULSE PROFILE CHANGES IN SWIFT J0243.6+6124, MXB 0656–072 AND GRO J1008–57

A THESIS SUBMITTED TO
THE GRADUATE SCHOOL OF NATURAL AND APPLIED SCIENCES
OF
MIDDLE EAST TECHNICAL UNIVERSITY

BY

ÇAĞATAY KEREM DÖNMEZ

IN PARTIAL FULFILLMENT OF THE REQUIREMENTS
FOR
THE DEGREE OF DOCTOR OF PHILOSOPHY
IN
PHYSICS

JUNE 2025

Approval of the thesis:

PULSE PROFILE CHANGES IN SWIFT J0243.6+6124, MXB 0656–072 AND GRO J1008–57

submitted by **ÇAĞATAY KEREM DÖNMEZ** in partial fulfillment of the requirements for the degree of **Doctor of Philosophy in Physics Department, Middle East Technical University** by,

Prof. Dr. Naci Emre Altun
Dean, Graduate School of **Natural and Applied Sciences** _____

Prof. Dr. Seçkin Kürkcüoğlu
Head of Department, **Physics** _____

Prof. Dr. Altan Baykal
Supervisor, **Physics, METU** _____

Assist. Prof. Dr. Muhammed Miraç Serim
Co-supervisor, **Physics, METU** _____

Examining Committee Members:

Prof. Dr. Sacit Özdemir
Astronomy and Space Sciences, Ankara University _____

Prof. Dr. Altan Baykal
Physics, METU _____

Prof. Dr. Sıtkı Çağdaş İnam
Electrical and Electronics Engineering, Başkent University _____

Assoc. Prof. Dr. Mehmet Atakan Gürkan
Physics, METU _____

Assoc. Prof. Dr. Sinan Kaan Yerli
Physics, METU _____

Date:18.06.2025

I hereby declare that all information in this document has been obtained and presented in accordance with academic rules and ethical conduct. I also declare that, as required by these rules and conduct, I have fully cited and referenced all material and results that are not original to this work.

Name, Surname: Çağatay Kerem Dönmez

Signature :

ABSTRACT

PULSE PROFILE CHANGES IN SWIFT J0243.6+6124, MXB 0656–072 AND GRO J1008–57

Dönmez, Çağatay Kerem
Ph.D., Department of Physics
Supervisor: Prof. Dr. Altan Baykal
Co-Supervisor: Assist. Prof. Dr. Muhammed Miraç Serim

June 2025, 116 pages

This thesis investigates pulse profile variations in three Be-type high-mass X-ray binary pulsars, Swift J0243.6+6124, MXB 0656–072, and GRO J1008–57, focusing on their spin frequency evolution and accretion-related transitions. Using data from NICER/XTI, RXTE/PCA, Fermi/GBM and Swift/BAT, timing analyses are performed to identify pulse profile structure changes across different luminosity levels. Theoretical models of accretion column geometry (the Becker model) and accretion torque (Ghosh & Lamb model) are tested against observations.

For Swift J0243.6+6124, a previously unreported transition in the pulse profile is discovered at $\sim 7 \times 10^{36}$ erg s^{-1}, consistent with the theoretical luminosity threshold L_{coul} between pure pencil beam and hybrid beam regimes. At higher luminosities, the data support the predicted L_{crit} transition to fan beam geometry, allowing the neutron star's magnetic field strength to be constrained to 4.7–5.3 $\times 10^{12}$ G.

MXB 0656–072 shows consistent single-peaked profiles across its 2007–2008 Type I outbursts. Torque–luminosity modelling of the spin frequencies shows that the Ghosh

& Lamb model successfully reproduces the spin frequency evolution, and resulting a magnetic field estimate of $\sim 4.2 \times 10^{12}$ G, in line with earlier cyclotron line detections.

Pulse profiles of GRO J1008–57 remain double-peaked and stable despite flux variation by a factor of 75. The absence of transitions in pulse profiles challenges the Becker model unless implausibly high magnetic fields or neutron star parameters are assumed. As a whole, the results demonstrate that analysing pulse profiles and spin evolution provides key insights into the accretion mechanisms in Be-type X-ray binaries.

Keywords: Neutron Stars, Accreting Pulsars, X-Ray Binaries, Accretion Columns

ÖZ

SWIFT J0243.6+6124, MXB 0656–072 VE GRO J1008–57'DEKİ ATIM PROFİLİ DEĞİŞİMLERİ

Dönmez, Çağatay Kerem
Doktora, Fizik Bölümü
Tez Yöneticisi: Prof. Dr. Altan Baykal
Ortak Tez Yöneticisi: Dr. Öğr. Üyesi Muhammed Miraç Serim

Haziran 2025, 116 sayfa

Bu tez çalışmasında Swift J0243.6+6124, MXB 0656–072, ve GRO J1008–57 adlı üç Be tipi yüksek kütleli X-ışını çiftindeki atım profili değişimleri, dönme frekanslarının evrimi ve kütle aktarımı ile ilişkili geçişlerine odaklanarak incelenmiştir. Farklı parlaklık düzeylerinde atım profillerinde meydana gelen yapısal değişimleri saptamak amacıyla, NICER/XTI, RXTE/PCA, Fermi/GBM ve Swift/BAT verileri üzerinden zamanlama analizleri yapılmıştır. Kütle aktarım sütunu geometrisi (Becker modeli) ve kütle aktarım torkuna (Ghosh & Lamb modeli) dair kuramsal veriler, gözlemlerle karşılaştırılarak test edilmiştir.

Swift J0243.6+6124 kaynağında, $\sim 7 \times 10^{36}\,\mathrm{erg\,s^{-1}}$ parlaklıkta daha önce rapor edilmemiş bir atım profili geçişi saptanmıştır. Bu geçiş, saf kalem ışınımı ile hibrit ışınım rejimleri arasında kuramsal olarak öngörülen L_{coul} eşiğiyle örtüşmektedir. Daha yüksek parlaklıklarda ise veriler, pervane ışınım geometrisine geçişin gerçekleştiği L_{crit} eşik parlaklığını desteklemiş ve bu da atarcanın manyetik alanının $4.7–5.3 \times 10^{12}\,\mathrm{G}$ aralığında sınırlandırılmasına imkan tanımıştır.

MXB 0656–072, 2007–2008'deki Tip I parlamaları boyunca tutarlı bir şekilde tek tepeli bir atım profil yapısı sergilemiştir. Dönme frekanslarının tork–parlaklık modeliyle incelenmesi, Ghosh & Lamb modelinin dönme frekansı evrimini başarıyla yeniden oluşturabildiğini göstermiştir. Bu modelleme üzerinden elde edilen $\sim 4.2 \times 10^{12}$ G büyüklüğündeki manyetik alan tahmini ise daha önceki siklotron çizgi tespitlerinden elde edilen tahminler ile uyumludur.

GRO J1008–57'nin atım profilleri, kaynak akısındaki 75 katlık değişime rağmen kayda değer bir şekil değişikliğine uğramadan çift tepe yapısını korumaktadır. Fakat atım profillerinde herhangi bir geçişin gözlemlenmemiş olması, gerçekçi olmayan manyetik alanlar ya da nötron yıldızı parametreleri varsayılmadıkça Becker modelinin bu kaynağı açıklamakta yetersiz kaldığını düşündürmektedir. Genel olarak tüm bu kaynaklardan elde edilen sonuçlar, atım profilleri ve dönme frekansı evrimi analizlerinin Be tipi X-ışını çiftlerindeki madde aktarım mekanizmalarına dair önemli ipuçları sağladığını göstermektedir.

Anahtar Kelimeler: Nötron Yıldızları, Kütle Aktarımı Yapan Atarcalar, X-Işını Çiftleri, Yığılma Sütunları

to my family

ACKNOWLEDGMENTS

I would like to express my heartfelt gratitudes to my supervisor, Prof. Dr. Altan Baykal. His insightful guidance, constant encouragement, patience, and unwavering confidence in me throughout my PhD studies have been invaluable to me. I am thankful to Prof. Dr. Sıtkı Çağdaş İnam for his positive outlook, guidance, and constructive feedback which have significantly contributed to my academic development. I also appreciate their valuable comments and advice of the other esteemed members of my thesis committee, Prof. Dr. Sacit Özdemir, Assoc. Prof. Sinan Kaan Yerli, and Assoc. Prof. Mehmet Atakan Gürkan.

I am deeply indebted to my co-supervisor, Assist. Dr. Muhammed Miraç Serim, and Dr. Danjela Serim. To me, they are more than just advisors or colleagues: Along with Prof. Baykal, I truly felt like I was part of an "academic family" with them. Their generosity in sharing their expertise and their endless guidance—both academic and emotional—played a crucial role in helping me complete my studies.

I also acknowledge the support of the Scientific and Technological Research Council of Turkey (TÜBİTAK) through the research project MFAG 118F037.

This long doctoral journey was possible not only through academic support but also thanks to the presence of valuable friends, both at METU and beyond. Through our laughs and jokes, sorrows and occasional quarrels, their support in good times and bad will always be remembered. Although there are too many to mention by name, I am confident they know how much they mean to me. As an exception, I would like to thank Eray Canlar, for his significance throughout my doctoral journey, his unwavering support, and his exceptional ability to listen to me, even when the topic was physics, a field (*once*) completely foreign to him!

Above all, I would like to thank my beloved family for their unconditional love and steadfast support throughout my life.

TABLE OF CONTENTS

ABSTRACT v

ÖZ vii

ACKNOWLEDGMENTS x

TABLE OF CONTENTS xi

LIST OF TABLES xiv

LIST OF FIGURES xv

LIST OF ABBREVIATIONS xvii

CHAPTERS

1 INTRODUCTION 1

1.1 Neutron Stars 1

1.1.1 High-Mass X-Ray Binaries 3

1.1.1.1 Be-Type High Mass X-Ray Binaries (BeXBs) 3

2 ACCRETION IN X-RAY BINARIES 9

2.1 Accretion via winds 10

2.2 Accretion via disk 12

2.3 Accretion Columns 15

2.3.1 Becker Model 16

2.3.1.1 Mathematical Framework of the Becker Model 16

2.3.2 Mushtukov Model 22
2.3.3 Accretion Mound 24
3 DATA ANALYSIS AND METHODS 27
3.1 Data Acquisition and Reduction 27
3.1.1 NICER/XTI Data Reduction 28
3.1.2 RXTE/PCA 30
3.1.3 Fermi/GBM 31
3.1.4 Swift/BAT 32
3.2 Timing Analysis 32
3.2.1 Nominal period estimations: Periodograms 34
3.2.2 Pulse Timing 36
3.2.3 Intrinsic spin frequency evolution 39
4 SWIFT J0243.6+6124 43
4.1 Introduction 43
4.2 Observations 46
4.3 Timing Analysis 47
5 MXB 0656–072 57
5.1 Introduction 57
5.2 Observations 58
5.3 Timing Analysis 59
5.3.1 Torque–luminosity correlation 61
6 GRO J1008–57 67
6.1 Introduction 67

6.2 Observations 69
6.3 Timing Analysis 70
7 DISCUSSION 77
7.1 Swift J0243.6+6124 77
7.2 MXB 0656–072 79
7.3 GRO J1008–57 82
8 CONCLUSION 87
REFERENCES 91
APPENDIX 109
A Lists of Observations Used 109
CURRICULUM VITAE 115

LIST OF TABLES

TABLES

Table 3.1 Summary of the data sets used in the thesis. 28

Table 4.1 Timing parameters of Swift J0243.6+6124 for four different intervals. 50

Table 6.1 Timing parameters of the timing model to fit Fermi/GBM frequencies of GRO J1008–57. 71

Table 7.1 Estimated magnetic field strength and corresponding transition luminosities of GRO J1008–57. 83

Table 8.1 Summary of the key findings. 88

Table A.1 The list of NICER/XTI observations of Swift J0243.6+6124. 109

Table A.2 The list of RXTE/PCA observations of MXB 0656–072. 111

Table A.3 The list of NICER/XTI observations of GRO J1008–57. 114

LIST OF FIGURES

FIGURES

Figure 1.1 Illustration of a pulsar. 2

Figure 1.2 Illustration of a BeXB system. 4

Figure 1.3 An example spectrum of a BeXB. 4

Figure 1.4 A light curve demonstrating Type I and II outbursts. 5

Figure 1.5 The Corbet diagram. 7

Figure 2.1 An illustration of wind accretion in X-ray binaries. 10

Figure 2.2 An illustration of disk accretion in X-ray binaries. 13

Figure 2.3 Pencil and fan beams. 16

Figure 2.4 A schematic summarizing the Becker model. 17

Figure 2.5 Schematic of the Mushtukov model. 23

Figure 2.6 Schematic of an accretion mound. 25

Figure 4.1 Spin frequency history and the synthetic pulse timing results of Swift J0243.6+6124. 51

Figure 4.2 The spin frequency history of Swift J0243.6+6124 constructed over the full 2017–2018 outburst. 52

Figure 4.3 Time-sorted pulse profiles of Swift J0243.6+6124. 53

Figure 4.4 Luminosity-sorted pulse profiles of Swift J0243.6+6124. 54

Figure 4.5 Torque modelling of Swift J0243.6+6124, step 1. 55

Figure 4.6 Torque modelling of Swift J0243.6+6124, step 2. 55

Figure 5.1 Luminosity-sorted pulse profiles of MXB 0656–072. 60

Figure 5.2 Time of arrivals of pulses from RXTE/PCA observations of MXB 0656–072. 62

Figure 5.3 Spin frequency history of MXB 0656–072. 62

Figure 5.4 Torque modelling of MXB 0656–072, step 1. 63

Figure 5.5 Torque modelling of MXB 0656–072, step 2. 65

Figure 6.1 Pulse frequency and pulsed flux history of GRO J1008–57 by Fermi/GBM. 68

Figure 6.2 NICER/XTI daily count rates of GRO J1008–57. 70

Figure 6.3 Timing model of the spin frequencies of GRO J1008–57. 72

Figure 6.4 Time of arrivals of GRO J1008–57. 73

Figure 6.5 Spin frequency evolution of GRO J1008–57. 74

Figure 6.6 Fermi/GBM spin frequency history of GRO J1008–57, highlighting the orbitally corrected part. 75

Figure 6.7 Luminosity-sorted pulse profiles of GRO J1008–57. 75

Figure 7.1 The parameter space of solution of Equation (7.1). 80

Figure 7.2 Variation of the magnetic field strength of MXB 0656–072 with distance. 82

Figure 7.3 The parameter space of solution of Equation (7.5). 85

Figure 8.1 Accretion column versus accretion mound geometry. 89

LIST OF ABBREVIATIONS

ABBREVIATIONS

ASM	All Sky Monitor
BAT	Burst Alert Telescope
BeXB	Be/X-ray binary
CALDB	Calibration Database
CGRO	Compton Gamma Ray Observatory
CRSF	cyclotron resonance scattering feature
DR2	Data Release 2
EDR3	Early Data Release 3
FPM	Focal Plane Module
GBM	Gamma-ray Burst Monitor
GTI	good time interval
HEASARC	High Energy Astrophysics Science Archive Research Center
HEXTE	High Energy X-ray Timing Experiment
HMXB	high-mass X-ray binary
HXD	Hard X-ray Detector
Insight-HXMT	Hard X-ray Modulation Telescope
ISO	International Organization for Standardization
ISS	International Space Station
IXPE	Imaging X-ray Polarimetry Explorer
JPL	Jet Propulsion Laboratory
LAT	Large Area Telescope

LMXB	low-mass X-ray binary
MJD	Modified Julian Date
MPU	Measurement and Power Unit
MNRAS	Monthly Notices of the Royal Astronomical Society
NASA	National Aeronautics and Space Administration
NICER	Neutron Star Interior Composition Explorer
OSSE	Oriented Scintillation Spectrometer Experiment
PCU	proportional counter unit
QPO	quasi-periodic oscillation
RPD	radiation pressure dominated
RXTE	Rossi X-ray Timing Explorer
SAA	Southern Atlantic Anomaly
SAS	Small Astronomy Satellite 3
SGXB	Supergiant X-ray binary
SNR	signal-to-noise ratio
ToA	time of arrival
ULX	ultraluminous X-ray source
ULXP	ultraluminous X-ray pulsar
UVOT	Ultraviolet/Optical Telescope
VLA	Karl G. Jansky Very Large Array
XRT	X-Ray Telescope
XTI	X-ray Timing Instrument

DECLARATION

Hereby, I declare that this thesis describes my own original work, except where explicitly stated. No part of this work has previously been submitted, either in the same or different form, to this or any other university in connection with a higher degree or qualification.

The results presented in this thesis are published in two separate articles. The findings of Swift J0243.6+6124 are published as the article *"Timing analysis of Swift J0243.6+6124 with NICER and Fermi/GBM during the decay phase of the 2017–2018 outburst"* in Monthly Notices of the Royal Astronomical Society (MNRAS) [1], in collaboration with M. M. Serim, D. Serim, L. Ducci, A. Baykal and A. Santangelo. The findings of MXB 0656–072 are published as the article *"Pulse frequency variations and timing noise of MXB 0656–072 during the 2007–2008 Type I outbursts and implications for its magnetic field"* in Astronomy and Astrophysics (A&A) [2], in collaboration with M. M. Serim, D. Serim, Y. Tuo, L. Ducci, A. Baykal and A. Santangelo. The findings of GRO J1008–57 are not yet published in a peer reviewed journal. Both publications investigate the timing and timing noise properties of the examined sources. Within the scope of this thesis, I conducted torque–luminosity modelling, and analysed pulse morphologies and their evolution with respect to time and luminosity in the aforementioned sources.

CHAPTER 1

INTRODUCTION

The evolutionary path of X-ray binaries begins with a binary system where at least one of the stars is sufficiently massive. The more massive star evolves first, undergoing nuclear fusion at a much faster rate. If it has a mass greater than around 8 solar masses ($M_{\odot}$), it undergoes a core-collapse supernova, leaving behind a neutron star or a black hole. The fate of the binary after the supernova depends on its orbital configuration prior to the explosion: the binary may either stay gravitationally bound or become disrupted [3]. If the system survives, the lower-mass companion may continue to evolve. Depending on its mass, the long-term evolution can lead to mass transfer onto the neutron star, either via stellar winds of the companion or via a process known as Roche-lobe overflow.

The subsequent evolution of the binary is governed by the nature of the mass transfer. Mass accretion regulates the rotational behaviour of the neutron star by exerting torques through interactions with its strong magnetic field ($\sim 10^{12}$ G). Meanwhile, orbital dynamics may be affected by gravitational wave radiation over long timescales. As a result, the orbit may gradually shrink, leading to a more compact and more interactive system [4, 5].

1.1 Neutron Stars

Neutron stars in X-ray binaries are among the most fascinating and extreme laboratories of astrophysics. These compact remnants of massive stars often possess magnetic fields in excess of 10^{12} G and spin periods ranging from milliseconds to several seconds. Most of the deductions about the physical conditions of neutron stars arise from

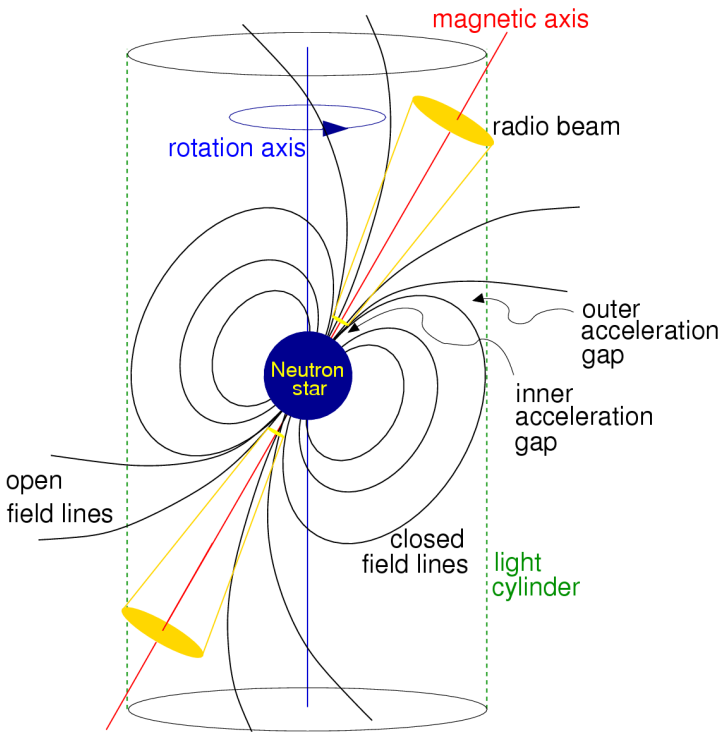


Figure 1.1: Illustration of a pulsar, showing the misalignment between the rotation and magnetic axes. [6]

the study of a subset known as *pulsars*. The dipolar magnetic field configuration of pulsars is misaligned with their spin axis. As a result of the inclined orientation of the field, the emission from the polar caps is observed as periodic pulses (see Figure 1.1). This property allows us to examine the rotation dynamics of pulsars, which opens many doors to understand physics regarding the environmental conditions due to the torque sources and in some cases even inner composition of a pulsar can be extrapolated. The pulsars in binary systems generally reside in complex environments where they interact with their stellar companions in ways that give rise to accretion and relativistic plasma flows. Studying such objects provides insights into the late stages of stellar evolution, strong-field gravity, the physics of superfluidity, interactions at very strong magnetic fields, and accretion-driven variability across a wide range of timescales and energies [7, 8, 9].

1.1.1 High-Mass X-Ray Binaries

The nature of the evolution of binary systems depends largely on the companion. The less massive companions evolve slowly, filling their Roche lobe when they reach the giant phase. On the other hand, the more massive companions can deliver matter without filling their Roche lobes. They can expel matter through strong winds or by forming a decretion disk around themselves which can interact with the pulsar. Therefore, the pulsars in binary systems are divided into subgroups considering the companion in the system: high-mass (HMXBs) and low-mass (LMXBs) X-ray binaries. The LMXBs host a companion star of spectral type later than A-type, whereas the HMXBs have very massive O- or B- type companions [10]. The HMXBs are further divided into smaller groups: Be/X-ray binaries (BeXBs), Supergiant X-ray binaries (SGXBs) and recently, some ultraluminous X-ray sources (ULXs) are shown to contain pulsars.

In this thesis study, all of the examined sources (Swift J0243.6+6124, MXB 0656–072 and GRO J1008–57) belong to the BeXB category.

1.1.1.1 Be-Type High Mass X-Ray Binaries (BeXBs)

BeXBs host a fast rotating B-type star that is not in the supergiant phase (Figure 1.2). Such stars also exhibit spectral lines of emission, leading to them being named as *Be*-type. Hydrogen, helium, and iron helium emission lines can be observed in their spectra [11]. Figure 1.3 illustrates an example of such Hα and He emission of X Persei. In addition, when compared with B type stars, Be-type stars show excess infrared emission in their spectra. These properties are interpreted as evidence for the presence of an equatorial disk formation around the Be star. To form a circumstellar disk, a Be star should spin very fast, close to the critical velocity at which the centrifugal acceleration mv^2/R matches the star's gravity. In such a case, the weak equatorial balance can be disrupted to form a disk by ejecting matter. There are alternative models to examine different physical conditions which can lead to angular momentum transport on the equatorial plane [12, 13, 14, 15, 16]. Even though the physical origins are still debated, the expelled matter is expected to form a circumstellar disk on the equatorial

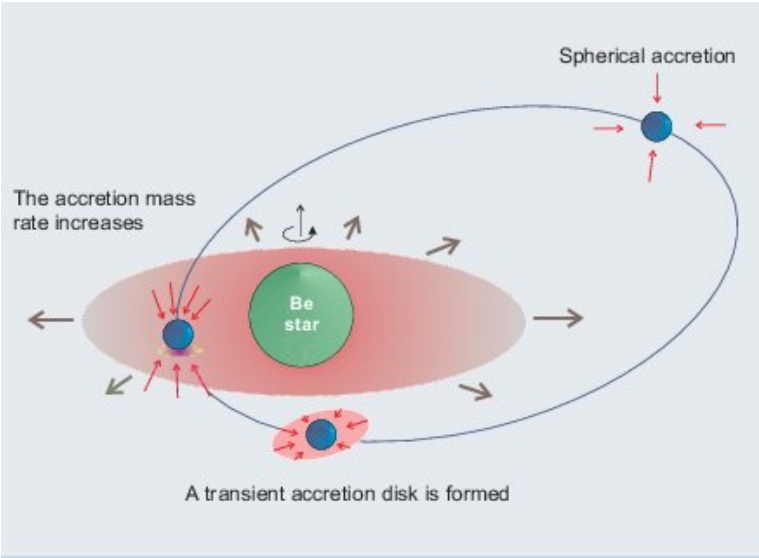


Figure 1.2: Illustration of a BeXB system [18].

plane, and it is gradually fed by the continuous expulsion of matter from the Be star [17], regardless of the mechanism driving such a wind.

Pulsars in BeXBs revolve at relatively eccentric orbits ($e > 0.3$) around their companion. Around the periastron passages, the pulsar interacts with the equatorial disk of the Be star, leading to periodic capture of matter from this disk. The captured matter follows the direct accretion scheme of a pulsar entering into dense region (see Section 2.1 for more detailed discussion). As the gravitational energy of the matter in accretion is converted into radiation, periodic X-ray emission bursts are observed at the orbital phases corresponding to periastron passages. Such periodic bursts are

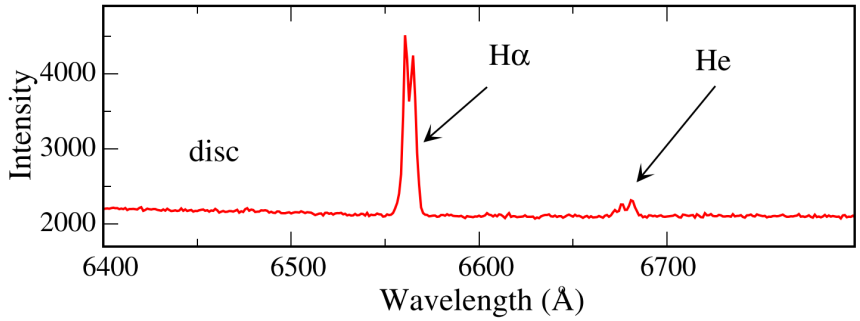


Figure 1.3: An example spectrum illustrating Hα and He emissions observed from the BeXB system X Persei [10].

referred to as Type I outbursts. The Type I outbursts typically lead to an almost one order of magnitude increase in the X-ray luminosity and last for a small fraction of the orbital period (0.2–0.3 P_{orb}) [10]. The BeXBs that are at quiescence and are at Type I outburst phases generally have X-ray luminosity below 10^{37} erg s^{-1}, meaning that the accretion column does not reach the stage of local dominant radiation pressure. Therefore, during the Type I outbursts, the pulsations should be generated by a pencil or hybrid beam geometry (see Section 2.3 for accretion column physics).

Besides the Type I outbursts, BeXBs also experience significantly larger flux enhancements (3-4 orders of magnitude in X-ray luminosity). In some cases, the luminosity even exceeds the Eddington limit for a pulsar under the isotropic assumption (e.g., Swift J0243.6+6124 [19]). These events, classified as Type II outbursts, do not seem to have an orbital preference and they last much longer when compared to Type I outbursts (Figure 1.4). Even though the underlying mechanism of these drastic events are not yet clear, they are generally attributed to possible changes in the equatorial disk of the Be star, because the only process that can trigger large flux enhancements on such timescales is expected to arise from the equatorial disk–pulsar interaction. Con-

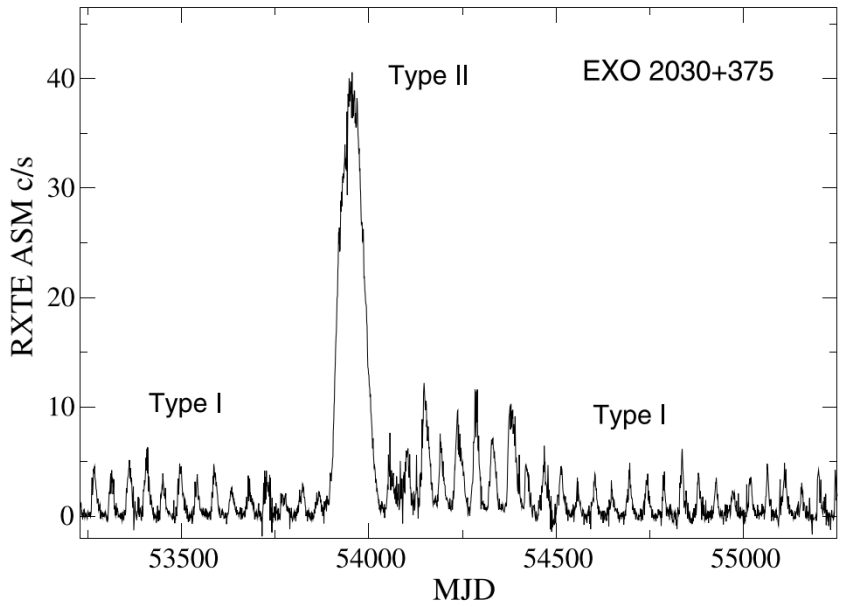


Figure 1.4: The light curve of EXO 2030+375 shows the periodic nature of Type I outbursts, along with a giant Type II outburst for comparison. However, many systems do not exhibit persistent Type I outbursts [10]

sequently, the captured matter may also form another disk (the accretion disk) around the pulsar, apart from the equatorial disk of the Be companion, because the strong spin-up rates observed in Type II outbursts cannot be explained through inefficient wind accretion processes. Moreover, the correlation between spin-up rates and luminosity, and the observations of quasi-periodic oscillations (QPOs) in the light curve, point towards disk formation. In many cases, optical observations indicate changes in Hα equivalent width, implying possible disruption of the equatorial disk of the Be star. For example, the $H\alpha$ equivalent width of 4U 0115+63 switches from negative to positive following a Type II outburst, leading to interpretations of the fading away of the disk after the burst [20]. However, this is not always the case. Even though the $H\alpha$ equivalent width gets affected by a Type II event, it may not lead to the gradual disappearance of the disk [10].

Almost all known BeXBs exhibit X-ray pulsations that are interpreted as the existence of a pulsar in the system because of the timescales of the pulsations. The periods of pulsars in BeXBs vary in the range from seconds to minutes. The current models on the rotational evolution of pulsars [21] can accommodate pulsar periods in the range 1–1000 s. The spin periods of pulsars P_{spin} in BeXB systems are shown to correlate with their orbital periods P_{orb} [22]. The P_{spin} vs. P_{orb} distribution of different binary pulsar populations is known as the Corbet diagram (Figure 1.5. BeXBs exhibit a positive correlation in the Corbet diagram, which is explained by their proximity to the long-term equilibrium period driven by accretion. The long-term accretion leads to the stabilization of pulsar rotation as an interplay of positive and negative torques experienced (See Chapter 2 for propeller and accretor phases). At the equilibrium period, the magnetospheric boundary rotates close to the Keplerian velocity. Reaching such an equilibrium is closely related to the accretion rate, thus, the experienced torques. On the other hand, the mass accretion rate should be inversely proportional to the distance of the pulsar from its companion (i.e., the binary separation distance), since both the wind and equatorial disk density should be lower at long distances. Therefore, binaries with long periods and large separations have a lower accretion rate, meaning that they will reach an equilibrium state on longer timescales.

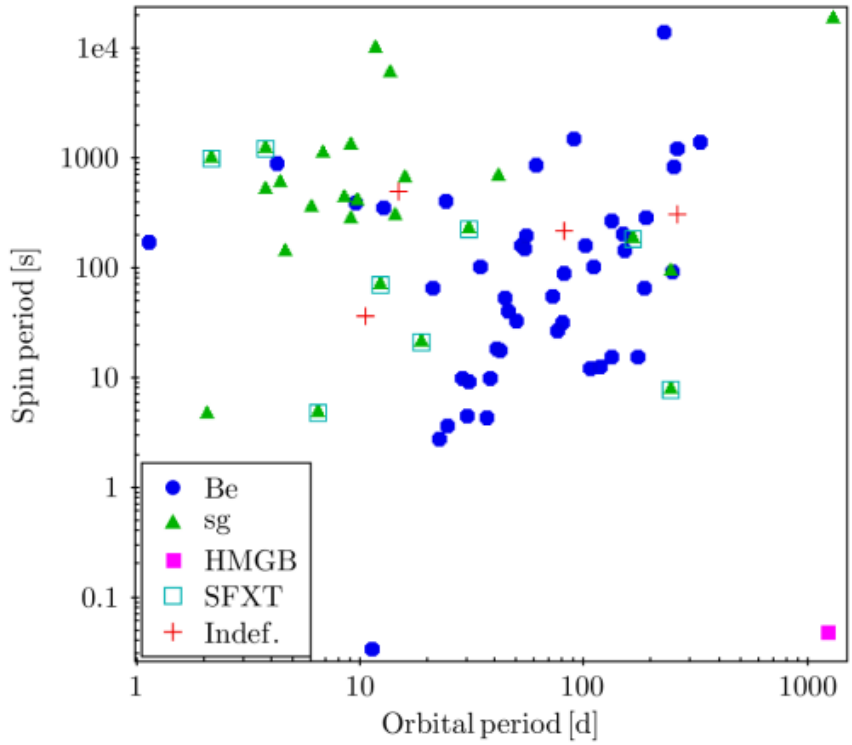


Figure 1.5: The Corbet diagram of 75 HMXBs. The labels in the legend respectively stand for BeXBs, SGXBs, high mass gamma-ray binaries, supergiant fast X-ray transients, and other unclassified HMXBs [23].

CHAPTER 2

ACCRETION IN X-RAY BINARIES

Pulsars in binary systems can steal and accumulate matter from their companion stars. In high-mass X-ray binaries (HMXBs), the donor star is typically either an OB supergiant or a Be-type star. In supergiant systems, mass transfer generally occurs through the capture of the companion's fast, radiatively driven stellar wind [24, 25, 26], A simplified case involves a massive companion losing its outer layers through a stellar wind, part of which is captured by the pulsar. However, in closer binary configurations where the evolved companion fills its Roche lobe, mass transfer can proceed through Roche lobe overflow instead [27]. This case typically leads to higher and more stable accretion rates compared to the more stochastic wind-fed scenario. In contrast, in Be/X-ray binaries (BeXBs), mass transfer results from occasional accretion from a circumstellar disk of a Be star (see Section 1.1.1.1 on the discussion of BeXBs) [28, 10]. In low mass X-ray binaries (LMXBs), the evolved low mass companion fills its Roche lobe. The material overflowing through the inner Lagrangian point L_1 is captured by the pulsar [29, 5].

After being captured by the pulsar, the infalling matter forms a disk as it spirals around the pulsar due to its angular momentum. The strong magnetosphere of the pulsar halts further inward motion, causing the disk to be truncated at an inner radius. The interaction between the incoming matter and the pulsar's magnetosphere guides the material toward its polar caps.

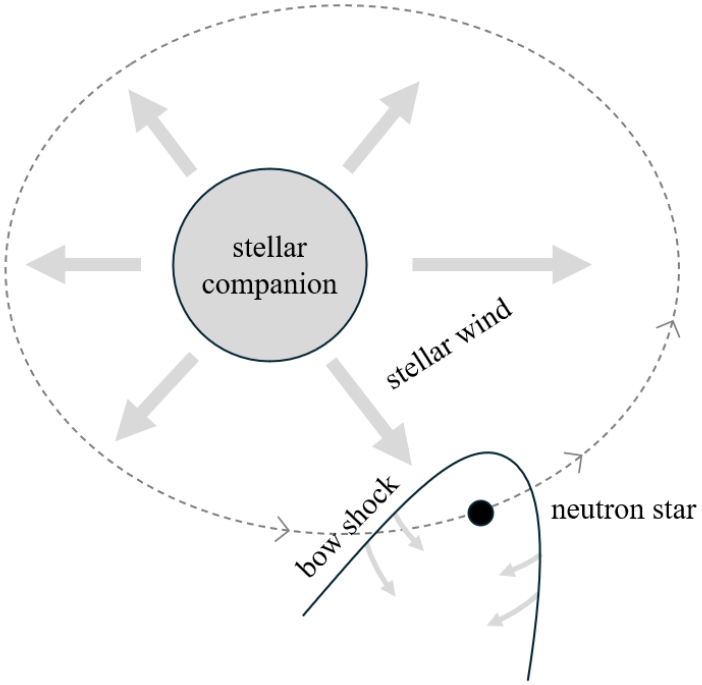


Figure 2.1: An illustration of wind accretion in X-ray binaries. Adapted from [31].

2.1 Accretion via winds

The wind accretion refers to the physical process of capturing matter expelled in the form of a stellar wind by the companion star. This form of accretion is relatively inefficient compared to disk accretion, as only a fraction of the radially diverging wind becomes gravitationally bound to the pulsar. The pulsar captures wind material with local density ρ as it travels through the surrounding medium. Bondi and Hoyle [30] examined such an accretion process involving a compact object travelling at a steady speed through a region of dense matter.

Stellar winds from the companion star are typically radial in nature, and both the wind's density and speed decrease as the gas moves farther away. Denoting the distance from the companion as r, the companion's radius as r_c, and the terminal wind velocity at its surface as v_∞, the wind velocity v_w is expected to decay radially in the form of a power law

$$v_w(r) = v_\infty \left(1 - \frac{r_c}{r}\right)^\beta , \tag{2.1}$$

where the power law index β typically ranges between ~ 0.8 and 1.2, and is associated

with the acceleration of the wind due to the radiation pressure of the star.

Wind capture also depends on the relative velocity (v_{rel}) between the stellar wind and the motion of the pulsar. At any point along its orbit, the pulsar's velocity corresponds to its local orbital velocity, v_{orb}. Then, the relative velocity can be described as

$$v_{rel} = \sqrt{v_w^2 + v_{orb}^2}. \tag{2.2}$$

When the wind velocity is sufficiently low, the interaction with the pulsar takes place at a region known as the accretion radius,

$$r_{acc} = \frac{2\,GM_*}{v_{rel}^2}, \tag{2.3}$$

where G is the constant of gravitation and M_* is the neutron star mass [1]. Accretion occurs when the wind velocity relative to the compact object is sufficiently low, allowing the material to be gravitationally captured within a region defined by the accretion radius. Bondi and Hoyle [30] approximated the accretion rate $\dot{M}$ for this interaction as

$$\dot{M} = \pi r_{acc}^2 \rho\, v_{rel} \tag{2.4}$$

and when Equation (2.4) and (2.3) are combined, the mass accretion rate becomes

$$\dot{M} = \frac{4\pi G^2 M_*^2 \rho}{v_{rel}^3}. \tag{2.5}$$

The observed X-ray luminosity L_X is linked to the accretion rate through

$$L_X = \eta \frac{GM_*\dot{M}}{r_*}, \tag{2.6}$$

where $\eta \sim 0.1$–1 is a dimensionless parameter representing the accretion efficiency and r_* is the radius of the pulsar. Applying Equation (2.5), the resulting X-ray luminosity takes the form

$$L_X = \eta \frac{4\pi G^3 M_*^3 \rho}{r_* v_{rel}^3}. \tag{2.7}$$

Studies of wind accretion under varying conditions suggest the possibility of distinct accretion regimes. For instance, if the magnetospheric radius r_m—where the accretion flow is disrupted by the magnetic field of the pulsar and begins to follow the field lines—is smaller than both the corotation radius r_c (see Equation (2.9) below) and accretion radius r_{acc}, the captured material is redirected by magnetic field lines toward

[1] Throughout the chapter, the subscript "$_*$" is used to denote the parameters of the pulsar.

the polar caps. Such an accretion regime is both expected and observed in high-luminosity accreting pulsars [24, 32]. If the pulsar's magnetosphere rotates faster than the local Keplerian frequency at the magnetospheric radius (i.e., $r_m > r_c$), the magnetic field lines act as a fan, inhibiting accretion by ejecting the incoming matter. This regime is known as the *propeller regime* [33]. On the other hand, Shakura et al. [34, 35] investigated conditions at low accretion rates and discussed the possibility of the formation of a quasi-spherical shell around the pulsar's magnetosphere. At the magnetospheric boundary, the accretion proceeds through the formation of a quasi-stationary convective shell. From this shell, matter is expected to penetrate the pulsar's magnetosphere via plasma instabilities, such as Rayleigh–Taylor and Kelvin–Helmholtz instabilities). This regime has been proposed to explain low-luminosity states and flaring behaviour in wind-fed X-ray binaries.

2.2 Accretion via disk

In LMXBs, disk accretion is the main mechanism of mass transfer. The companion star in a LMXB gradually evolves and fills its Roche lobe, and the matter overflowing at the inner Lagrangian point L_1 falls toward the pulsar. Due to its angular momentum, the infalling matter circulates around the pulsar before reaching its magnetosphere and forms an accretion disk [21, 31]. Disk accretion is also possible in HMXBs, depending on the conditions of the binary system. In BeXBs, for instance, an accretion disk may form when the pulsar interacts with the Be star's circumstellar disk. The strong magnetosphere of a pulsar will prevents matter from entering this region, causing the accretion disk to be truncated at an inner radius. The disk truncation is expected to occur roughly where the ram pressure of the infalling matter balances the outwards magnetic pressure of the pulsar. This radius is known as the *Alfvén radius*, defined as

$$r_A = k \left(\frac{\mu^4}{2GM_* \dot{M}^2} \right)^{1/7}, \tag{2.8}$$

where $k \sim 0.5$ is a dimensionless constant, $\mu = B_* r_*^3$ is the magnetic dipole moment of the neutron star and B_* is the magnetic field strength of the neutron star. Typically, the Alfvén radius r_A and the magnetospheric radius r_m are very similar and often

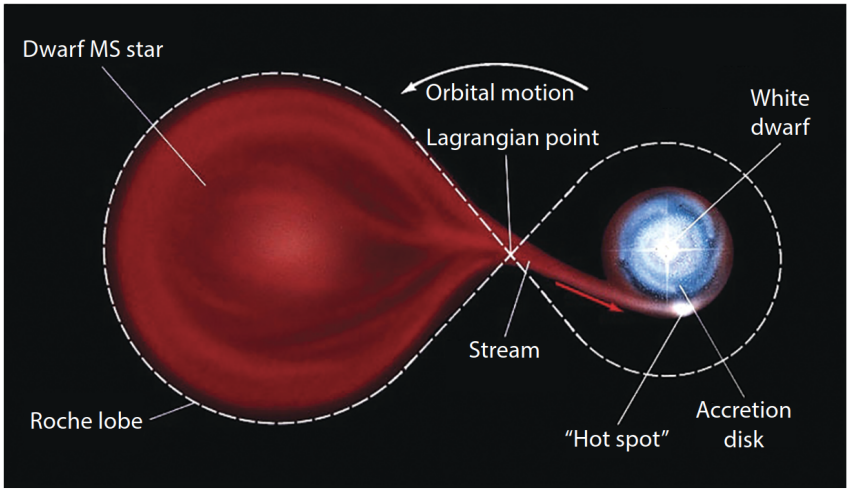


Figure 2.2: An illustration of disk accretion in X-ray binaries via Roche robe overflow [27].

used interchangeably; but r_m may differ slightly due to system-specific properties such as disk geometry or mode of accretion. More specifically, the relation is given by $r_m = \xi r_A$, where ξ is dimensionless factor in the range $\sim$0.5–1 [29].

Another important radius in the disk is the *corotation radius*, at which the local Keplerian rotation rate of the matter matches the pulsar's spin:

$$R_c = \left(\frac{GM_*}{\Omega^2}\right)^{1/3} = \left(\frac{GM_* P_{spin}^2}{4\pi^2}\right)^{1/3}. \tag{2.9}$$

Here, $\Omega = 2\pi/P_{spin}$ is the angular velocity of the pulsar, with P_{spin} representing its spin period.

Even though the exact geometry of the dipolar field of a pulsar at large distances remains uncertain (e.g., open field lines [36] or threading the disk over a wide range of radii [37]), theoretical models predict that there should be a region of the inner disk inside the Alfvén radius at which the locally vertical (poloidal) component of the dipole field B_z threads the disk. Such a region is the main are of interaction for the torque experienced by the pulsar. For a simple description of disk accretion scheme, the prescription given by Ghosh & Lamb [37] is presented in this thesis. Nevertheless, it should be noted that a variety of models exist in the literature, proposing different physical processes and geometries [38, 36, 39].

The reasoning for presenting the Ghosh & Lamb model is its wide acceptance, owing to its coherent description of observational results from many known X-ray binaries. The model assumes that the magnetic field line penetrates the disk over a large region. As a result, the torque interactions occur not only at the magnetospheric boundary but also across a wide range of radii. This extended interaction enables sustained angular momentum exchange, which can lead to spin-up or spin-down torques, depending on the relative rotation between the pulsar and the inner disk. Accordingly, the model introduces the fastness parameter ω_s to compare the angular velocity of the pulsar, Ω, to the Keplerian angular velocity at the magnetospheric radius, $\Omega_K(r_m)$, serving as a dimensionless diagnostic parameter:

$$\omega_s = \frac{\Omega}{\Omega_K(r_m)} = \left(\frac{r_m}{r_c}\right)^{3/2} \tag{2.10}$$

- When $\omega_s < 1$, the inner disk rotates faster than the pulsar. In this case, the torque exerted on the pulsar will causes it to spin up.
- At $\omega_s = 1$, the pulsar and the disk are in corotation.
- If $\omega_s > 1$, the pulsar spins faster than the disk at the magnetospheric radius, and the interaction causes the pulsar to lose angular momentum and spin down.

At the interaction region within the disk, the magnetic field lines are twisted due to the differential rotation between the Keplerian disk and the pulsar. The bending of the vertical component of the field gives rise to a toroidal magnetic field B_ϕ. In the Ghosh & Lamb model, this magnetic interaction continues beyond the Alfvén radius, with field lines connecting the pulsar to the disk over an extended region ($r_m < r < r_{out}$). The model formulated the net torque exerted on the pulsar as

$$N = n(\omega_s)\,\dot{M}\sqrt{GM_* r_m}\,, \tag{2.11}$$

where $n(\omega_s)$ is a dimensionless torque function given by

$$n(\omega_s) \approx 1.39\,\frac{1-\omega_s\left[4.03(1-\omega_s)^{0.173}-0.878\right]}{1-\omega_s}. \tag{2.12}$$

As explained in 3.2, X-ray observations allow us to measure the spin frequency of the pulsar. The torque acting on the pulsar is related to the change in its spin frequency,

$\dot{\nu}$, as

$$\dot{\nu} = \frac{N}{2\pi I_*} = \frac{n(\omega_s)\dot{M}\sqrt{GM_* r_m}}{2\pi I_*} \tag{2.13}$$

where I_* is the pulsar's moment of inertia. One can convert Equation (2.13) into form with observable/predictable quantities using accretion luminosity $L_X = \frac{GM_*\dot{M}}{r_*}$ and Equation (2.8):

$$\left(\frac{\dot{\nu}}{\nu_{12}}\right) \approx 1.4\ n(\omega_s) \left(\frac{M_*}{M_{1.4}}\right)^{-3/7} \left(\frac{I_*}{I_{45}}\right)^{-1} \left(\frac{r_*}{r_6}\right)^{6/7} \left(\frac{L_X}{L_{37}}\right)^{6/7} \left(\frac{\mu}{\mu_{30}}\right)^{2/7}. \tag{2.14}$$

This equation is normalized for typical pulsar parameters: ν_{12} = 10^{-12} Hz s^{-1}, $M_{1.4}$ is 1.4 solar mass ($1.4M_\odot$), I_{45} = 10^{45} g cm^2, r_6 = 10^6 cm, L_{37} = 10^{37} erg s^{-1}, and μ_{30} = 10^{30} G cm^3. Among those parameters, luminosity is the most dominant, as it can vary by several orders of magnitude during an accretion episode, while the others remain largely constant. The impact of typical pulsar parameters (e.g., mass) is relatively minor compared to the major changes in luminosity. Therefore, during outbursts, we observationally expect a correlation of

$$\dot{\nu} \propto L_X^{6/7}. \tag{2.15}$$

This power-law relationship is a key observational prediction of the model. Furthermore, it can be used to investigate the intrinsic spin evolution of pulsars (see Section 3.2.3 for details).

2.3 Accretion Columns

All accretion models, whether involving disk or wind accretion, are primarily formulated based on a dipolar magnetic field, as it is the dominant component at larger distances where matter–field interaction takes place. In the standard picture, matter is channelled along magnetic field lines toward the pulsar's polar caps for accretion. As it nears the surface, the material forms an *accretion column*. Mainly, the physics of the column structure is governed by the balance of local gravitational force, radiation pressure due to accretion, magnetic pressure and ram pressure of the accreted gas.

2.3.1 Becker Model

This section presents the accretion column model developed by Becker et al. [40]. This accretion column model aims to describe the relevant physical processes as a basis for understanding the data analysis results discussed later in the thesis. It approximates the physical conditions within the column using a roughly cylindrical geometry, where the ram pressure of the infalling matter is balanced by radiation pressure and Coulomb interactions, depending on the accretion rate. At different accretion rates—and hence at different X-ray luminosity levels—the direction of photon diffusion changes, allowing for a switch between pencil and fan beam modes (Figure 2.3). The luminosity level at which this transition occurs is referred to as the *critical luminosity*. The key feature of this model is the assumption of a scale height within the accretion column where the cyclotron resonant scattering feature (CRSF) is imprinted. A schematic detailing the changes in accretion column geometry with at different luminosity levels are presented in Figure 2.4.

2.3.1.1 Mathematical Framework of the Becker Model

As the incoming matter is funnelled toward the polar caps, it predominantly travels under free-fall conditions. The free-fall velocity of the matter v_{ff} upon reaching the pulsar's surface can be calculated as

$$v_{ff} = \sqrt{\frac{2GM_*}{r_*}}. \tag{2.16}$$

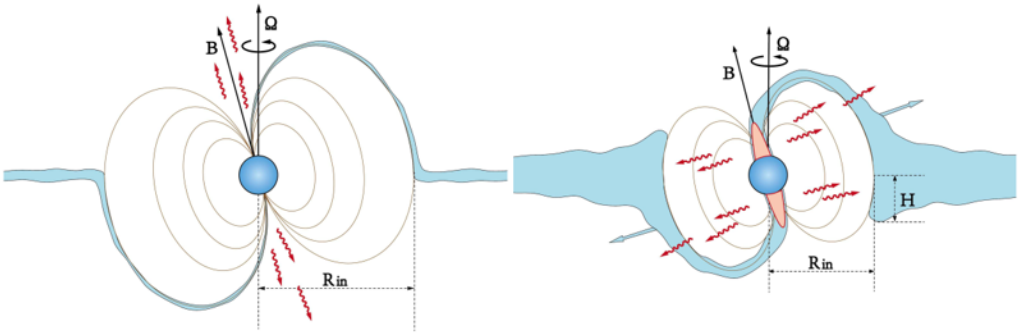


Figure 2.3: Pencil (left) and fan (right) beams, indicated by red wavy arrows [41].

As matter begins to accumulate in the polar cap regions, newly infalling material enters the region of accumulated plasma and experiences a shock. In an advection-dominated shock, the matter is expected to slow down to a post-shock velocity v_{ps}, determined by the Rankine–Hugoniot relations:

$$v_{ps} = \frac{1}{7} v_{ff} \tag{2.17}$$

Assuming that the incoming matter decelerates at a constant rate a after experiencing a shock at a height H above the surface, and reaches the surface over a dynamical timescale t_{dyn}, one can establish the kinematic equations to derive the deceleration rate, a:

$$H = \frac{v_{ps}^2}{2a} \quad \Rightarrow \quad a = \frac{v_{ps}^2}{2H} = \frac{GM_*}{49Hr_*} \tag{2.18}$$

As the gravitational energy of the infalling matter is converted into radiation, an outward radiation pressure begins to build up. Equilibrium is achieved when this pressure

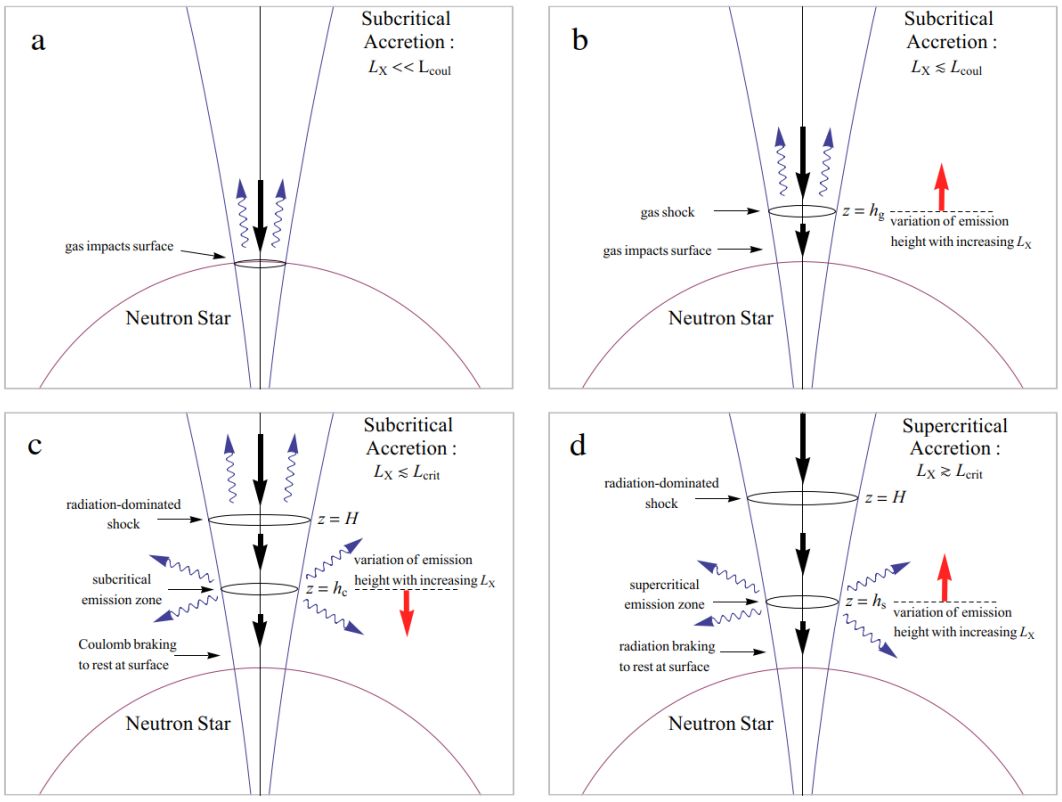


Figure 2.4: A schematic summarizing the Becker model. The panels show the changes in the geometry and the emission processes of the accretion column with increasing luminosity [40].

reaches the well-known *Eddington limit:*

$$L_{\text{Edd}} = \frac{4\pi G M_* m_p c}{\sigma_T} \tag{2.19}$$

$\sigma_T = 6.653 \times 10^{-29}$ m^{-2} is the Thomson cross-section. However, it is important to note that photons do not escape solely in the radial direction; they can also escape transversely in what is known as the *fan beam* mode. Consequently, the model accounts for this by modifying the Eddington limit to include direction-dependent Thomson scattering cross-sections $\sigma_{\parallel}$ and $\sigma_{\perp}$, corresponding to the parallel and perpendicular directions to the magnetic field axis. By applying a further correction for the geometry of the accretion flow, the effective Eddington limit is redefined as

$$L^*_{Edd} = L_{Edd} \frac{\sigma_{\perp}}{\sigma_{\parallel}} \frac{\pi r_0^2}{4\pi r_*^2} = \frac{G M_* m_p c}{\sigma_{\parallel}} \frac{\pi r_0^2}{r_*^2}, \tag{2.20}$$

where $m_p = 1.673 \times 10^{-24}$ g is the proton mass, c is the speed of light, and r_0 is the radius of the accretion column.

Returning back to the deceleration rate after the post-radiation shock, a, it is counterbalanced by the local gravitational force. However, in addition to local gravity

$$g_{local} = \frac{G M_*}{r_*^2}, \tag{2.21}$$

there is also an upward force due to radiation pressure. To account for both effects, the model approximates an effective gravity, corrected for radiation pressure, as:

$$g_{eff} = \left(\frac{L_X}{L^*_{Edd}} - 1 \right) \frac{G M_*}{r_*^2}. \tag{2.22}$$

If the deceleration rate in Equation (2.18) matches the effective gravity, then the effective radial motion of the infalling matter ceases. Under this condition, radiation primarily diffuses sideways through the column walls instead of escaping radially, thereby giving rise to the fan beam mode. Thus, using Equations (2.18) and (2.22), one can derive the critical luminosity L_{crit}, which defines the transition to fan beam mode in terms of the effective Eddington limit as

$$L_{crit} = L^*_{Edd} \left(1 + \frac{R_*}{49H} \right) \tag{2.23}$$

Bolometric X-ray luminosities below and above this value is referred to as *subcritical* and *supercritical* luminosity levels, respectively. Transverse diffusion still occurs

below the threshold, but it is not the dominant mode. In the supercritical regime, radiation is expected to escape predominantly in the transverse direction, forming a fan beam. In the subcritical regime, particularly near the critical luminosity threshold, a hybrid mode combining both pencil and fan beams is expected, whereas a pure pencil beam mode is anticipated at substantially lower luminosity levels.

This balance condition in the sinking region can also be interpreted in terms of the relative timescales of radial motion, t_{dyn}, and transverse diffusion, t_{diff}. When the timescale for transverse motion is shorter than that of radial motion, radiation escapes sideways, leading to fan beam emission. By equating these two timescales, the model predicts that a radiation-dominated shock occurs at a height

$$H = \frac{\dot{M}\sigma_T}{2\pi m_p c}. \tag{2.24}$$

Using the accretion luminosity L_x,

$$L_X = \frac{GM_*\dot{M}}{r_*} \tag{2.25}$$

the scale height of the radiation dominated shock, H, can be expressed in terms of observable or predictable quantities:

$$H = 1.14 \times 10^5 \text{ cm} \left(\frac{M_*}{M_{1.4}}\right)^{-1} \left(\frac{r_*}{r_6}\right) \left(\frac{L_X}{L_{37}}\right) \tag{2.26}$$

The radiation-dominated shock height marks the upper boundary of the sinking region. In the supercritical regime, the Becker model assumes that the CRSF forms within this boundary region, at altitudes lower than H). As stated previously, the key aspect of this model is the assumption of a scale height at which the CRSF is imprinted on the spectrum. One formed, a CRSF provides a direct estimate of the magnetic field strength as

$$E_{cyc} \approx 11.6 \text{ keV} \left(\frac{B_*}{B_{12}\,(1+z)}\right) \tag{2.27}$$

where B_{12} = 10^{12} G, and z is the gravitational redshift [42].

In the supercritical regime, the scale height h_{super} is expected to lie at altitudes where photons have sufficient time to diffuse through the column walls, resulting in fan beam emission. At heights above h_{super}, photons will not have enough time to diffuse transversely, thus photon escape becomes primarily radial. Below this height, high

opacity due to dense gas region again inhibits transverse motion. Therefore, in the supercritical regime, the CRSF is expected to emerge at the height

$$h_{super} \approx 2.3 \times 10^3 \text{ cm} \left(\frac{M_*}{M_{1.4}}\right)^{-1} \left(\frac{r_*}{r_6}\right) \left(\frac{L_X}{L_{37}}\right). \tag{2.28}$$

On the other hand, in the subcritical regime, emission is concentrated in the region where Coulomb interactions become sufficiently dominant to effectively decelerate the infalling matter. In this case, the CRSF is expected to form within this region, around the scale height

$$h_{sub} \approx 1.48 \times 10^5 \text{ cm} \left(\frac{B_*}{B_{12}}\right)^{-4/7} \left(\frac{L_X}{L_{37}}\right)^{-5/7}. \tag{2.29}$$

The difference in the X-ray luminosity dependence of the emission heights h_{sub} and h_{super} gives rise to important observational implications, to be discussed at the end of this section.

The transitional luminosity level from the subcritical to the supercritical regime, as given in Equation (2.23), can be recast in terms of observable or predictable parameters by considering the following:

i) the association between the column radius and the Alfvén radius [43],

ii) the fact that most of the emission occurs at energies lower than E_{cyc}, allowing the ratio $\sigma_T/\sigma_\parallel$ to serve as a rough estimate of the emission ratio,

iii) the approximation that the mean spectral energy is thermal in nature.

With these assumptions, the critical luminosity level L_{crit} can be approximated as

$$L_{crit} \approx 1.49 \times 10^{37} \text{ erg s}^{-1} \left(\frac{M_*}{M_{1.4}}\right)^{29/30} \left(\frac{r_*}{r_6}\right)^{1/10} \left(\frac{B_*}{B_{12}}\right)^{16/15}. \tag{2.30}$$

Equation (2.30) can account for a bimodal distribution of positive and negative correlations between cyclotron energies and X-ray luminosities observed in different pulsars. Furthermore, as the beam pattern transitions from a hybrid mode to a pure fan beam, there should be observational signatures in the pulse profile across this luminosity threshold, reflecting the change in emission geometry. Finally, since the dominant photon interaction mechanisms also vary, these changes should result in luminosity-dependent variations in the spectral index distribution.

It should be noted that the transition between pencil and fan beam geometries is expected in nearly all of the accretion column models, as the calculations consistently rely on the local balance between the ram pressure of infalling matter and dominant radiation pressure at high luminosities. However, the assumption of a scale height for the CRSF feature enhances the predictive power of the model about the spectral behaviour.

For example, the negative correlation between the CRSF scale height and luminosity in the subcritical regime (see Equation (2.29)) implies that the boundary region contracts as luminosity increases. This results in greater optical depth and consequently, harder X-ray emission [44]. In contrast, the positive correlation in the supercritical regime suggests the opposite behaviour.

Thus, L_{crit} signifies not only a pulse profile transition but also a spectral transition in the Becker model. As the model offers strong observational predictions, it can be tested across different systems. In this thesis, we examine the sources Swift J0243.6+6124, MXB 0656–072, and GRO J1008–57 to test the model and understand the physics behind the emission of these sources thoroughly.

In the subcritical accretion regime, when the accretion rate is too low to generate sufficient radiation pressure or enable effective Coulomb interactions at the boundary region, the infalling matter is expected to decelerate through a gas-mediated shock near the stellar surface. This defines an additional regime in which all the emission from the pulsed region is expected to be emitted in the pencil beam mode. This case defines another transitional regime, between hybrid and full pencil beam emission, occurring around a threshold luminosity of

$$L_{coul} \approx 1.17 \times 10^{37} \text{ erg s}^{-1} \left(\frac{M_*}{M_{1.4}}\right)^{11/8} \left(\frac{r_*}{r_6}\right)^{-13/24} \left(\frac{B_*}{B_{12}}\right)^{-1/3}. \tag{2.31}$$

In this thesis, we present observational evidence consistent with the expected transition at L_{coul}, based on the changes in the pulse profile morphology in Swift J0243.6+6124. Furthermore, the ratio of the transitional levels L_{crit} and L_{coul} depends on the magnetic field strength of the source:

$$\frac{L_{crit}}{L_{coul}} \approx 1.27 \left(\frac{B_*}{B_{12}}\right)^{7/5} \tag{2.32}$$

The above expression is simplified using typical pulsar parameters (M_* = 1.4$M_\odot$, R_* = 10 km). Identifying both transitional levels allows for a distance-independent estimation of a magnetic field strength, providing an alternative to relying on the CRSF energy in the X-ray spectrum.

2.3.2 Mushtukov Model

There are alternative models that examine the accretion column under different physical conditions and geometries. Apart from the Becker model, one of the key studies that focus on the transition effects is the Mushtukov model [45]. This model calculates the critical accretion luminosity L_{crit} for magnetized neutron stars, incorporating the effects of exact Compton scattering cross-sections in strong magnetic fields, resonant scattering, photon polarization, and accretion geometry. In this section, a brief description of this model is introduced.

According to Mushtukov et al. [45], as the infalling matter heats the polar cap to create a hotspot at that area, it generates a local radiation pressure. Thus, it exerts a force that decelerates the infalling matter with the radiative acceleration g_R:

$$g_R = \frac{\kappa_{eff}}{c} F \tag{2.33}$$

where κ_{eff} is the effective opacity, and F is the radiative flux from the hotspot. Assuming isotropic emission and a hotspot area S, the flux is given by

$$F = \frac{L_X}{2S}. \tag{2.34}$$

Considering the free fall velocity (v_{ff}) of the incoming matter, stopping the flow within a height $h/2$ above the pulsar surface requires a deceleration g

$$g = \frac{v_{ff}^2}{h}, \tag{2.35}$$

is to be balanced by the radiation deceleration g_R in Equation (2.33). The balance condition yields

$$\frac{\kappa_{eff}}{c} F_{crit} = \frac{v_{ff}^2}{h}, \tag{2.36}$$

and solving F_{crit} from the Equation (2.36) leads to

$$F_{crit} = \frac{c v_{ff}^2}{\kappa_{eff} h}. \tag{2.37}$$

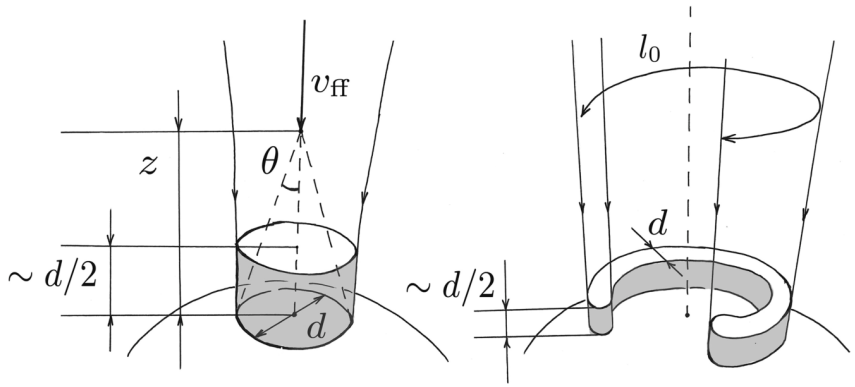


Figure 2.5: Schematic of the Mushtukov model [45], showing the expected geometries of the accretion column by the accretion via wind (left) and disk (right).

At this stage, the critical flux F_{crit} corresponds to the emission from the hotspot. However, determining the flux received at the observer requires an assumption about the emission geometry. Assuming that the hotspot has a circular shape with a surface area $S = \pi d^2/4$, where d is the diameter of the hotspot, Mushtukov et al. [45] further assume that the stopping height $h/2$ is comparable to the hotspot diameter d, i.e., $h \approx 2d$. Under this assumption, L_{crit} becomes

$$L_{crit} = 2SF_{crit} = \frac{\pi d^2}{2}\frac{cv_{ff}^2}{\kappa_{eff}d} = \frac{c\pi d}{\kappa_{eff}}\frac{GM_*}{R}. \tag{2.38}$$

If the typical pulsar parameters are introduced, L_{crit} can be expressed as

$$L_{crit} \approx 3.7 \times 10^{36} \left(\frac{\kappa_T}{\kappa_{eff}}\right) \frac{d}{d_5}\frac{R_6}{R_*}\frac{M_*}{M_{1.4}} \quad \text{erg s}^{-1} \tag{2.39}$$

where $\kappa_T \approx 0.34\,\text{cm}^2\,\text{g}^{-1}$ is the Thomson opacity for solar composition plasma, and d_5 is 10^5 cm.

In the case of disk accretion, matter approaches the neutron star more closely, becoming confined within a narrow magnetic funnel. The width of this accretion stream is determined by how far the accretion disk penetrates into the neutron star's magnetosphere [46]. Utilising the Shakura & Sunyaev disk model [38], the Mushtukov model hypothesizes that the magnetospheric radius of the pulsar resides in a region where Kramer opacity and gas pressure are dominant. The hotspot in the disk case is not a

circle but a closed ring, whose area S_D can be approximated as

$$S_D = l_0\, d \approx 3 \times 10^9\, \Lambda^{-7/8} \left(\frac{M_*}{M_{1.4}}\right)^{-13/20} \left(\frac{R_*}{R_6}\right)^{19/10} \left(\frac{B_*}{B_{12}}\right)^{-1/2} \left(\frac{L_X}{L_{37}}\right)^{2/5} \text{cm}^2, \tag{2.40}$$

where l_0 and d is the base length and the width of the ring, and Λ is a constant related to the accretion flow geometry ($\Lambda < 1$ in disk accretion).

Mushtukov model has its own considerations about L_{crit}. For instance, L_{crit} is not monotonic in magnetic field strength. It is minimum at around a few $\times$ 10^{36} erg s^{-1}, when the CRSF energy is around $\sim$10 keV (implying B $\sim$ 10^{12} G). For smaller B, L_{crit} increases to $\sim$$10^{37}$ erg s^{-1} regardless of other parameters. For larger B, L_{crit} increases again, this time due to smaller Compton scattering cross-sections.

Despite its promising framework, one of the main caveats of the Mushtukov model is that determining L_{crit} is not straightforward. Although Equation (2.38) and Equation (2.39) appear explicit, both d and κ_{eff} ultimately depend on L_{crit}. As a result, the expression for the critical luminosity is implicitly self-dependent, and the calculation of L_{crit} requires numerical iterations, which complicates its application.

2.3.3 Accretion Mound

Apart from the Becker and Mushtukov models, it should be noted that there are alternative models that probe different possible conditions in the accretion column (e.g., Basko & Sunyaev [47]; Arons, Klein & Lea [48]; Harding & Lai [49]; Becker & Wolff) [50]; Mukherjee, Bhattacharya & Mignone [51]; Postnov et al. [52]; Staubert et al. [42]).

For example, Heindl et al. [53] considers a growth of the sinking region in the shape of an "accretion mound" (see Figure 2.6) at low luminosities. The structure of the mound is determined by the balance between ram pressure from infalling matter, gravity, and magnetic pressure. Instead of a simple cylindrical structure, accretion mounds are shaped with non-uniform emission regions at varying altitudes [54]. As a result, the direction in which radiation escapes from the accretion mound is influenced by the mound's shape, along with other parameters such as the gravitational bending around the pulsar [42]. Accretion mounds emit X-rays that often feature distinct

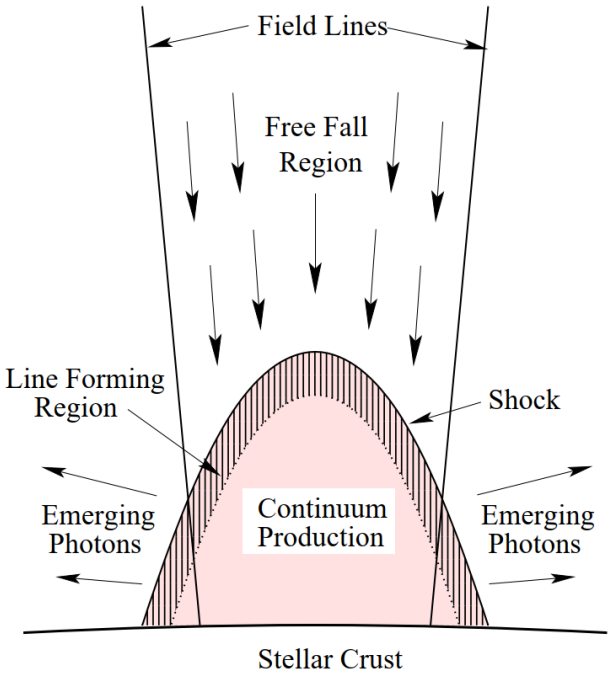


Figure 2.6: Schematic of an accretion mound [53].

CRSFs, reflecting the magnetic field's geometry and magnitude in those regions [51]. In general, determining the structure of accretion mounds require numerical solutions of magnetohydrodynamical equilibrium equations [51, 55]. Even though the model is not analytical and not readily applicable without complex simulations, the results appear to be consistent with observational inferences from some sources, such as 4U 0115+63, Vela X–1, and GX 301–2 [53].

CHAPTER 3

DATA ANALYSIS AND METHODS

3.1 Data Acquisition and Reduction

X-ray observations are conducted with various space observatories with a wide variation of detector design and specification. In addition, the data gathered via such space observatories carry complexities since they are constantly affected by the space weather, detector performances deteriorate and malfunctions occur over time. Therefore, obtaining the data is only the first step: Available data are mostly in a preprocessed, raw form, and are not suitable for any direct analysis. Processing the raw data is essential for creating calibrated and filtered data products suitable for further analysis. For these reasons, each X-ray mission has its own tools, pipelines and calibration databases for its own raw data, depending on unique detectors and environmental space conditions on its path. The final data products have standardized formats regardless of the observatory, thus, these can be manipulated with common tools. The process to reach final data products from raw data is referred to as *data reduction*.

NASA (National Aeronautics and Space Administration) HEASARC (High Energy Astrophysics Science Archive Research Center) website accommodates a vast X-ray data archive from various space observatories, and the software necessary for the data reduction and analysis [56]. HEASoft is a software package containing both the common and mission-specific tools necessary for the X-ray data analysis. A complementary tool is the CALDB (Calibration Database), where all the necessary information about the X-ray observatories are stored for the calibration of raw data. Both HEASoft and CALDB are updated regularly to accommodate the recent changes in X-ray missions, and to provide more functionality.

The observational data used in this thesis, and the aforementioned software is downloaded in the publicly available archives of NASA HEASARC. Publicly available spin frequency histories from Fermi/GBM and daily light curves from Swift/BAT are also utilized, obtained from the respective mission websites [57, 58]. The data sets employed in the analysis of each source are summarized in Table 3.1. The analyses are conducted using the most recent versions of HEASoft and CALDB available at the time, and the versions used for specific analyses are indicated in each chapter. The analysis tools and steps are version-agnostic (at least throughout the time period of the thesis work), are explained in the next sections of this chapter. Any specific step diverging from the standard data reduction is therefore stated in the respective chapter.

3.1.1 NICER/XTI Data Reduction

The Neutron Star Interior Composition Explorer (NICER) is an X-ray observatory launched to Earth orbit in 2017 July, and deployed on the International Space Station (ISS) [59]. Its main instrument, X-ray Timing Instrument (XTI), consists of 56 X-ray concentrator and focal plane module pairs, all aligned within $1'$ to work together.

Table 3.1: Summary of the data sets used in the thesis. "*" indicates that the value is the number of pulse frequency (Fermi/GBM) or daily light curve (Swift/BAT) measurements.

	Observatory /Detector	Dates (MJD)	Number of observations	Total exposure (ks)
Swift J0243.6+6124	NICER/XTI	58029–58532	188	485
	Fermi/GBM	58027–58525	225*	
	Swift/BAT	58029–58559	472*	
MXB 0656–072	RXTE/PCA	54418–54788	171	438
	Fermi/GBM	54729–54750	6*	
GRO J1008–57	NICER/XTI	58947–59022	46	150
	Fermi/GBM	58947–59019	21*	
	Swift/BAT	58947–59022	76*	

It is devoted for time-resolved spectrometry with a <300 ns timing accuracy in the 0.2–12 keV energy range. XTI has a combined $\sim$1900 cm^2 effective area at 1.5 keV, collecting X-ray photons from a $\sim$30 $arcmin^2$ field of view.

The standard pipeline processing tool, `nicerl2`, is used to to apply the standard calibration and data screening processes to the raw NICER observations. It consists of several subtasks that perform these processes [60]:

- `nicercal` applies NICER-recommended standard calibration,
- `niprefilter2` creates NICER-specific calibrated filter files,
- `nimaketime` creates good time interval (GTI) files for event screening,
- `nicermergeclean` merges data from MPUs (Measurement and Power Unit) and apply screening, and
- `niautoscreen` performs standard screening for single FPMs (Focal Plane Module) and MPUs.

Without additional input, `nicerl2` uses default event screening parameters that work in most cases; but the parameters can be customized for specific cases. Some of the default parameters used to determine good time intervals are as follows [61]:

- NICER must be in target tracking mode.
- At least 38 of 56 detectors of NICER must be enabled.
- The detectors must be pointed toward the target source with an offset no greater than 0.015° (0.9 arcmin).
- NICER must not be inside the Southern Atlantic Anomaly (SAA), a region where the satellites are exposed to strong ionizing radiation.
- There must be least 15° separation between the source and the dark Earth limb; otherwise, reflected light from the Earth and atmospheric fluorescence and absorption may degrade the data quality.
- If the bright Earth limb is visible instead, the separation must be at least 30° to avoid the adverse effects from reflected light on the day side of the Earth.

Since the NICER observations used in the thesis (thankfully) did not require any special processing, the default parameters are employed.

The resulting event files are merged by `nimpumerge`, and the event times are corrected to the Solar system barycenter using the JPL (Jet Propulsion Laboratory) ephemeris DE430 by `barycorr` to eliminate the Doppler shifts in photon arrival times caused by the orbit of the Earth and ISS. Light curves are then generated using `xselect` and are consequently used in timing analyses. Unless stated otherwise, the NICER/XTI light curves are created with a time resolution of 0.1 s.

3.1.2 RXTE/PCA

The Rossi X-ray Timing Explorer (RXTE) was a X-ray observatory [62]. Launched into a 580 km orbit in 1995 December, it served the X-ray astronomy community for 16 years until its decommission in 2012 January. It consisted of 3 instruments: While The All Sky Monitor (ASM) was capable of observing 80% of the sky every 1.5 hour with a $6^\circ \times 90^\circ$ field of view in 2–12 keV range [63], The High Energy X-ray Timing Experiment (HEXTE) was dedicated to hard X-ray observations, consisting of two clusters of scintillation detectors with an energy range of 15–250 keV.

The third instrument, Proportional Counter Array (PCA) was an array of five identical proportional counter units (PCU), sensitive to 2–60 keV energy range, with a total collecting area of 6500 cm^2. A collimator on each PCU limited its field of view to 1°. The instrument had a 2^{-20} s ($\approx$1 µs) time resolution, and 256 energy channels, with 18% energy resolution at 6 keV. Over time, the PCUs were subjected to wear and tear, and only one PCU was operating reliably at the end of the operating life of PCA.

The timing analysis of MXB 0656–072 utilized RXTE/PCA data. First, the data are filtered for good time intervals. Data taken during times when the elevation angle is lower than 10°, pointing offset exceeds 0.02°, electron contamination is above 0.1, or during SAA passages are excluded from analysis. Light curves are created using the GoodXenon mode events, with a 0.125 s time resolution in 3–20 keV. Barycenter correction is applied to the event times, and since not all PCUs operate simultaneously, the `correctlc` task is used to normalize the count rates as if all PCUs were

active. Additionally, for each observation, separate X-ray spectra are created. Only PCU2 top layer data in standard2f mode (with a 16 s resolution) are used for this task. For background estimation, a bright background model is used for the observations exceeding 40 cts/s/PCU, while a faint background model is applied otherwise.

3.1.3 Fermi/GBM

Fermi Gamma-ray Space Telescope is a space observatory dedicated to X-ray and gamma-ray astronomy. It was launched into Earth orbit in 2008 June, and is still operating. It includes two instruments, LAT and GBM. The Large Area Telescope (LAT) is a pair-conversion gamma-ray telescope, with an energy range of 20 MeV to >300 GeV [64]. Its field of view encompasses $\sim$20% of the sky, and is over 30 times more sensitive than its predecessors.

The Gamma-ray Burst Monitor (GBM) is an all-sky monitor, providing a unique perspective on our understanding of pulsars in binary systems. Consisting of 12 sodium iodide scintillators and 2 bismuth germanate scintillators, it is sensitive to $\sim$8 keV–40 MeV range [65]. One particular aspect of GBM, which is the quick trigger response to burst events and its ability to enable persistent follow-up, is of fundamental importance. The Fermi/GBM Pulsar Team takes full advantage of this capability. Using the continuous stream of data, they apply an automated dynamical power density spectrum to search for periodicities; and when periodic signals are found, they track their evolution over time. This allows them to follow the spin frequency evolution of many pulsars, as long as the sources are bright enough to be detected. They also provide open access to their results and offering pulse frequency and light curve histories for various X-ray sources through the website of their monitoring program [57].

In this thesis, frequency measurements provided by the Fermi/GBM Pulsar Team are used as a precursor to timing analyses, where the pulse profiles at each epoch are refined through folding at an accurate frequency signal.

3.1.4 Swift/BAT

Neil Gehrels Swift Observatory, or Swift, is a multi-wavelength space observatory launched in 2004 November. Although it was designed for a 2 year mission, it is still functional after 20 years. Each of its 3 instruments is dedicated on a different part of spectrum. The X-Ray Telescope (XRT) is a focusing X-ray telescope with a 600×600 pixel resolution in 0.2–10 keV range [66]. The Ultraviolet/Optical Telescope (UVOT) is a 30 cm aperture telescope, designed to detect afterglows of gamma-ray outbursts in 170–650 nm [67].

The Burst Alert Telescope (BAT) is a hard X-ray transient monitor, serving as an all sky monitor in the 15–50 keV range [68]. It provides data on local sky events through its coded mask, enabling region filtering around the sky locations of known sources. With known source distances, BAT observations enable effective luminosity estimations in the 15–50 keV band for tracked X-ray sources. The Swift/BAT team conducts detailed analyses and provides daily flux readings for the sources in their monitoring program. These results are made publicly accessible for scientific research.

This thesis utilizes the flux measurements by the Swift/BAT team to investigate the luminosity evolution of the target sources. In particular, cross-examining pulse profile morphologies with their corresponding luminosities is crucial for determining the critical luminosity thresholds.

3.2 Timing Analysis

The light curves of X-ray binaries, along with the energy spectra, are the main data products providing information about the nature of these systems. When the rotation of the pulsar modulates the photon flux along our line of sight, periodic pulses in the light curve are observed. Therefore, the most basic information we can get from a light curve is the spin frequency of the pulsar in the X-ray binary. Using multiple observations, the spin frequency evolution of the pulsar can be tracked. Since rotational torques result in a non-zero spin frequency derivative, the changes in spin frequency

over time are associated with the physical conditions that supply torque. For example, isolated pulsars spin down (i.e., their spin rate slows down) due to magnetic braking torques (i.e., rotational energy loss due to the rotation of an inclined dipolar field). On the other hand, the circumstances due to environmental conditions in binary systems are much more sophisticated, since there is a complex accretion flow that leads to strong and in most cases inhomogeneous torques. Thus, tracking the systematic evolution of the spin frequency can reveal the ongoing accretion processes in the X-ray binary system or the orbit of the pulsar around the companion star, since the observed spin frequencies experience orbital Doppler shifts. Meanwhile, the fluctuations of spin frequencies over the systematic trend, referred to as timing irregularities, can give insights into the internal structure of the pulsar or the accretion processes in the binary system, depending on the structural profile of the fluctuations. In general, sudden and step-like jumps in the spin frequencies are called *glitch* events and are associated with sudden movements of the vortices within the superfluid interior. The remaining unstructured and inevitably stochastic residuals are often identified as timing noise. In binary systems, timing noise components are thought to originate from inhomogeneities in the accretion flow.

Not only the spin frequency but also the pulse shapes, referred to as *pulse profiles*, can vary over time. Depending on the system's nature and geometry, one or multiple pulses per cycle may be observed, and the shape of the pulse profiles may evolve with time and X-ray luminosity. Systematic changes in pulse profile morphology are interpreted as alterations in the local emission geometries near the pulsar's surface and accretion columns formed at the polar caps. These systematic variations in pulse profiles form the central focus point of this thesis, which examines the critical luminosity thresholds in relation to their expected pulse profile variations. It should also be noted that the energy dependency of the pulse profiles is for understanding the emission processes near the surface of the pulsar. Since the pulse profile shape depends on the folding frequency, timing analysis requires high precision. Therefore, this thesis employs the pulse timing technique, which is the most effective method for improving the measurement accuracy of periodic signals.

The following subsections provide a detailed account of the timing analysis methods used in this thesis.

3.2.1 Nominal period estimations: Periodograms

In popular science, pulsars are renowned for their precise pulsations, some of which rival the accuracy of atomic clocks. However, the spin periods of many pulsars are actually not truly stable. Particularly in accreting binaries, the pulse period of a pulsar can change significantly over time due to torque transfer from the accreting material. It is also subject to inhomogeneities in the accretion flow and intrinsic timing noise. Nevertheless, the relative change in the spin period of an accreting pulsar is still minuscule over short timescales, and the spin period change throughout a single observation, typically lasting from minutes to hours, is negligible. Frequency derivatives are typically in the order of $\sim 10^{-11}$ Hz s^{-1}, resulting in a spin frequency change of $\dot{\nu}\Delta t \sim 3600 \times 10^{-11} = 3.6 \times 10^{-8}$ Hz during a one-hour observation. This level of change is not detectable with the present-day X-ray instruments.

Therefore, we often assume that the overall shape of the pulse profiles throughout an observation does not change significantly: Even if there are pulse-to-pulse variations due to occasional fluctuations in the light curve or the limitations on the detector (e.g., a low signal-to-noise ratio—SNR), the pulse profiles can be safely regarded as stable at short timescales after folding.

Generally, processing a light curve starts with epoch folding. Here, assuming a constant (guess) spin frequency ν_{guess}, the light curve of an observation is folded over the corresponding spin period $P_{guess} = 1/\nu_{guess}$, starting from a reference time, or epoch, t_0. For the arrival time stamps t_i in the light curve, the phase Φ_i corresponding to each t_i can be calculated as

$$\Phi_i = \mathrm{Mod}_1\left(\frac{t_i - t_0}{P_{guess}}\right). \tag{3.1}$$

Since the data are folded over a certain period, the phases naturally reside in modulo 1 ($\Phi \in [0, 1]$). Given the limitations due to the time resolution and signal-to-noise ratio of the data, the calculated phases are binned into N phase bins in Mod[0, 1] range with a bin width of $\Delta\Phi = \frac{1}{N}$. The distribution of count rates in each phase bin forms a histogram known as a *pulse profile*. If the initial guess period is close to the true period ($P_{guess} \approx P_{true}$), the folded pulse profiles will align. Stacking each aligned profile increases the statistical significance of the resulting pulse profile. However, if

the guessed period deviates from the true period, the misaligned pulses will smear out when stacked, degrading the resulting profile.

The significance of the pulse profiles are often tested through χ^2 statistics, as an ideal pulse signal should significantly deviate from a flat distribution. For a pulse profile containing a photon count rate C_n within the n^{th} phase bin, the χ^2 statistic can be calculated as

$$\chi^2 = \sum_{0}^{n} \frac{(C_n - C_{avg})^2}{C_{avg}}, \tag{3.2}$$

where C_{avg} is the average count rate of the pulse profile. The χ^2 test is also applicable if the pulse morphology is non-sinusoidal, because short, sharp signal profiles will still differ significantly from a flat distribution at the C_{avg} level.

The epoch folding method is also used to reveal the correct spin period—or pulse folding period—of a light curve. Assuming the light curve is folded with the correct period, the peaks and dips of the pulses align at the same phase in each cycle, resulting in a pulse profile with maximum variation. If an incorrect spin period is used instead, a phase shift will occur with each successive pulse, causing the peaks and dips to drift in phase rather than remain aligned. As a result, the resulting pulse profile will appear smeared, and its peaks and dips will become less pronounced. If the folding period is significantly inaccurate and/or the light curve is long enough, the pulse profiles may shift more than a whole period over the course of the observation; and all the variations of the pulse profile will cancel out, leaving a flat pulse profile. Therefore, using the correct pulse period for epoch folding is essential for obtaining accurate pulse profiles.

One way to approximate the correct periodicity is to check the power distribution of different nominal (guess) periods. This distribution is known as a *periodogram*. For an evenly sampled light curve $x(t)$, the power at a frequency ν_{guess}, corresponding to a guess period $P_{guess} = 1/\nu_{guess}$, can be calculated as

$$P(\nu_{guess}) = \left| \sum_{j=1}^{M} x_j e^{-2\pi i t_j \nu_{guess}} \right|^2, \tag{3.3}$$

where $x_j = x(t)\omega(t)$ describes each windowed segment of the light curve on the window function $\omega(t)$. As explained above, if the guess period starts to deviate from the true periodicity, the folded profiles become smeared, resulting in reduced power

in the periodogram. Consequently, the power distribution across guess periods peaks at the true period, leading to a Gaussian-like profile around that peak.

3.2.2 Pulse Timing

Over the years, the regular pulsations observed from pulsars have given rise to a methodology known as the pulse timing technique. The idea behind this technique is to track the arrival times of pulses (times of arrival—ToAs) and understand how they evolve over time in the phase domain. After measuring the ToAs, their evolution is described using physically motivated models to extract information about the star's spin, orbital motion, and even spacetime curvature in its vicinity. This method enables measurement the periodicities with high precession, as the pulses must remain connected in phase.

Due to timing noise, SNR of the data, and pulse-to-pulse variability on short timescales, pulse profiles are not determined by tracking individual pulses but by averaging many pulses into a single profile. Often, a single pulse profile is created from a single observation. Therefore, the number of the pulses averaged is approximately the exposure time divided by the pulse period (as long as there are not significant gaps within one single observation). In this method, the initial stage begins with the same epoch folding as described in the previous section. However, during the folding process, all pulses are folded with respect to a common reference time t_0. This common reference time is referred to as the folding epoch. Once the profiles are generated, each is labelled with a timestamp (e.g., the midpoint of the observation or the folded interval) and a corresponding time uncertainty, which represents the total duration of the averaged profile. These timestamps and uncertainties are ultimately linked to the resulting ToAs and pulse phase shifts at the end of this analysis. Then, all the pulses are represented via harmonic functions (through their Discrete Fourier Transform—DFT) [69]:

$$\Phi(\phi) = A_0 + \sum_{k=1}^{N} [A_k \cos(2\pi k\phi) + B_k \sin(2\pi k\phi)] \tag{3.4}$$

Here the total number of harmonics N is swept with the index k.

The technique proceeds with the determination of a *template profile*. The template

profile is chosen either as the strongest (i.e., the one with the highest χ^2 when compared to a constant) among the timestamped profiles, or by averaging all profiles into a single template profile. To reach to cross-correlation phase, the DFT of the template pulse is described with

$$T(\phi) = G_0 + \sum_{k=1}^{N} \left[G_k \cos(2\pi k\phi) + M_k \sin(2\pi k\phi) \right], \tag{3.5}$$

where G_0, G_k and M_k are some coefficients. The aim of using DFT of the pulses is to provide a mathematical approach for determining the phase shift $\delta\phi_i$ of each individual profile with respect to a common profile (the template profile) and a common reference time (the folding epoch). This is achieved by identifying the phase offset that best aligns the data profile with the template. Mathematically, this is done by computing the cross-correlation function $C(\Delta\phi)$ via the inverse Fourier transform of the product:

$$C(\Delta\phi) = \mathcal{F}^{-1}[\Phi_k T_k^*] \tag{3.6}$$

The cross-correlation function is maximized at the best-fitting shift, yielding the ToA offset in the phase domain. Meanwhile, the second derivative of the cross-correlation function with respect to the phase shift hints the stability of the function's curvature and is used as an indicator of the accuracy range of $\Delta\phi \pm \sigma_\phi$ measurements:

$$\sigma_\phi^2 \approx -\left(\frac{d^2 C}{d\Delta\phi^2} \bigg|_{\Delta\Phi=0} \right) \tag{3.7}$$

As the curvature of the function depends on the pulse shape, sharply peaked profiles (with strong higher harmonics) yield better ToA estimates than broad, sinusoidal profiles. This is generally the case for pulsations observed in radio band, where pulses typically have sharp peak confined to a small fraction of the period. However, X-ray pulsations are broader and often extend across the entire period. In such cases, ToA uncertainties are approximated based on the noise of the observed profile, as

$$\sigma_{ToA} \approx \frac{W}{S_N \sqrt{N}}, \tag{3.8}$$

where W is the pulse width, S_N is signal-to-noise ratio of the profile (i.e., root mean square of the pulse profile divided over the standard deviation of the errors) and N is the number of Fourier harmonics. Even if they are used interchangeably, it should be noted that, conventionally, ToAs refer to pulse arrivals in the time domain, not

the phase domain. However, since pulse arrivals are always modelled in the phase domain in the literature, this has led to some confusion in terminology. In the time domain, ToAs can simply be evaluated using

$$t_{ToA} = t_{ref} + P\Delta\phi, \tag{3.9}$$

where t_{ref} is the timestamp at the folding stage and P is the folding period.

The time evolution of pulse ToAs in the phase domain reflects the rotational evolution of the pulsar. For isolated pulsars, the time evolution is simply described using polynomials to accurately determine the spin frequency and its derivatives as

$$\phi_{model}(t) = \phi_0 + v_0(t - t_0) + \frac{1}{2}\dot{\nu}(t - t_0)^2 + \frac{1}{6}\ddot{\nu}(t - t_0)^3 + \ \ldots\ , \tag{3.10}$$

where t_0 is the folding epoch as mentioned previously. In isolated pulsars, the frequency derivative $\dot{\nu}$ is the most noticeable term because it is directly related with the dipolar field strength of the pulsar through the magnetic braking model. Higher-order terms are generally attributed to timing noise arising from magnetospheric fluctuations.

For pulsars in binary systems, the phase evolution model requires further modifications since the pulses reach the observer (or detector) with time delays caused by the orbital motion of the pulsar. For a Keplerian orbit, the orbital delays can be characterized by

$$\delta\phi_{orb} = \nu\, a_c \sin i(\sin\omega(cosE - e) + \sqrt{1 - e^2}\cos\omega \sin E) \tag{3.11}$$

where $a_c \sin i$ is the projected semi-major axis (in light-seconds), e is the orbital eccentricity, ω is the longitude at periastron and E is the eccentric anomaly. The eccentric anomaly is found by solving Kepler's equation,

$$E - e\, sinE = M \tag{3.12}$$

where M is the mean anomaly; and as the equation cannot be solved analytically, finding E involves numerical computations. This way, the orbit parameters of the pulsar can be found (or refined, if the orbit parameters are previously provided) and the orbit modulation in spin frequency measurements can be removed to obtain orbit-corrected spin frequencies.

Also, the gravitational delays due to field of the companion is also included if the accuracy of the ToAs is adequate. Such delays are known as binary Shapiro delays and are described by

$$\delta\phi_{Shapiro} = -2r\, ln(1 - e\, cosE). \tag{3.13}$$

Therefore, the generic phase evolution model for a pulsar in a binary system can be approximated as

$$\phi_{model}(t) = \delta\phi_{orb} + \delta\phi_{Shapiro} + \phi_0 + v_0(t-t_0) + \frac{1}{2}\dot{\nu}(t-t_0)^2 + \frac{1}{6}\ddot{\nu}(t-t_0)^3 + ... \tag{3.14}$$

In general, the real phase evolution of the data is consistent with the models prescribed above. However, regardless of how complicated these models are, a residual remains relative to the expected trends ($\phi_{res} = \phi_{real} - \phi_{model}$). This implies that timing noise has a physical origin and is intrinsic to the pulsars.

The pulse timing analysis is a particularly powerful method; however, it requires phase-connection of the successive phase delay measurements ($\Delta\phi_i$) in order to track the phase evolution using the expected models. This is not always possible, especially if successive observations are not closely spaced, the pulse profiles change significantly over time, and/or a very strong frequency derivative causes deviations of more than several cycles between successive ToAs separated by Δt (i.e., $\dot{\nu}\Delta t \gg 1$). In such cases, situation-specific modifications are implemented. One example is also present in this thesis: due to the strong frequency derivative of Swift J0243.6+6124, we employed *synthetic pulse timing* (see Section 4.3 for details).

3.2.3 Intrinsic spin frequency evolution

The rotational evolution of pulsars in binary systems is strongly influenced by accretion torques. In the case of a disk accretion, generic theoretical models predict a power law relation $\dot{\nu} \propto L_x^{\alpha}$ between the bolometric X-ray luminosity (luminosity in the entire X-ray band, typically 0.1–200 keV [70]) and the spin frequency derivative [37, 36, 39]. Among those models, the most extensive used is the Ghosh & Lamb model [37]. This model, in particular, specifies the power law index of the relation as 6/7. This theoretical relation has shown observational consistency in many X-ray sources: not only in persistently emitting systems, but also in transient X-ray sources

during outbursts.

In accreting pulsars, it is possible to use a physical model to describe their rotational evolution (commonly referred to as the *intrinsic spin frequency evolution*), rather than relying on a phenomenological model, such as the one expressed in Equation (3.10). To achieve this goal, a torque model must be developed to examine the effect of mass transfer during accretion episodes [71]. Derivation of the intrinsic evolution begins with the frequency derivative. First, the relationship between changes in pulse frequency is examined within the data set. These relations are typically consistent with theoretical expectations and take the form:

$$\left(\frac{\dot{\nu}_{intrinsic}}{\dot{\nu}_{12}}\right) = 1.4\, n(\omega_s) \left(\frac{\mu_*}{\mu_{30}}\right)^{2/7} \left(\frac{r_*}{r_6}\right)^{6/7} \left(\frac{M_*}{M_{1.4}}\right)^{-3/7} \left(\frac{I_*}{I_{45}}\right)^{-1} \left(\frac{L_X}{L_{37}}\right)^{6/7}. \tag{3.15}$$

A simplified version of this equation, assuming other source parameters remain constant, yields a relation between the frequency derivative and luminosity as

$$\dot{\nu}_{intrinsic} = \beta L_x^{\alpha}, \tag{3.16}$$

where β sets the numerical factor for normalization connected to the mass, radius and magnetic field strength of the pulsar (see Equation (2.14)), and α is the power law index, ideally 6/7. Then, in principle, the intrinsic spin frequency evolution can be obtained by integrating this relation over time. Mathematically, the intrinsic frequency evolution can be expressed as [72, 73]:

$$\nu_{intrinsic}(t) = \nu_0 + \int_{t_0}^{t_f} \dot{\nu}_{intrinsic}(t')dt' = \nu_0 + \int_{t_0}^{t_f} \beta L_x^{\alpha}(t')dt' \tag{3.17}$$

Here t_0 and t_f are start and end times, and ν_0 is the spin frequency at t_0. This relation suggests that the intrinsic evolution can be found through the integration of a light curve. Flux measurements can be converted to luminosity if the source distance is known. If we integrate once more, we can obtain the intrinsic evolution in phase domain [71]:

$$\phi_{intrinsic}(t) = \phi_0 + v_0(t - t_0) + \int_{t_0}^{t_f} \nu_{intrinsic}(t')dt' \tag{3.18}$$

In the modelling of accreting pulsars, Equation (3.17) or (3.18) replaces Equation (3.10) to construct a model based on physical principles. Notably, this approach also allows for the determination of the power law index α, enabling tests of the validity of different theoretical models across various sources.

From a technical point of view, these calculations need to be performed on real data with discrete time steps. In this thesis, the data modelling described above was performed using Python-based scripts. The Python script first performs torque–luminosity modelling, then interpolates the X-ray flux using a spline function to address data sparsity, and finally performs numerical integration using the trapezoidal rule to obtain Equation (3.17) or (3.18).

CHAPTER 4

SWIFT J0243.6+6124

4.1 Introduction

Swift J0243.6+6124 is the first galactic ultraluminous X-ray pulsar (ULXP) discovered in the Milky Way. It is located at 2h 43m 40.43s, +61° 26′ 03.76″ [74], in the constellation Cassiopeia. It was first detected on 2017-10-03, Modified Julian Date (MJD) 58029, by a Swift/BAT trigger [75]. Right after the initial discovery, subsequent Swift observations revealed pulsations with a period of ∼9.86 s, and the source was first suggested to be an X-ray pulsar [76]. Along with the detections by the major X-ray observatories, the source was also identified in the radio band using the Karl G. Jansky Very Large Array (VLA) [77].

The discovery of this source coincided with the start of a very bright Type II outburst (MJD ∼58030–58150), followed by a series of Type I outbursts (MJD ∼58150–58550). Therefore, Swift J0243.6+6124 was active for around 500 days and fade into quiescence around February 2019 until a re-brightening in 2023.

These outbursts are well-studied, and an extensive literature regarding the timing and spectral properties of Swift J0243.6+6124 exists [78, 79, 80, 81, 82, 83, 84, 85, 86, 87, 88, 89].

First of all, the companion of the binary system was determined to be a Be star [90] of O9.5Ve spectral type with V = 12.9 mag, based on optical observations [19], confirming that the system is a BeXB. The companion exhibits long-term optical and infrared variability, in line with the behavior of BeXBs, yet no short-term periodic variability. The orbital parameters of the system was determined by Doroshenko et al. [91], and

the orbit period was estimated to be 28.3±0.2 days.

Different distance estimates of Swift J0243.6+6124 are used throughout the existing literature. Some of the estimates are:

- 2.5±0.5 kpc based on optical photometry and spectroscopy of the Be-type companion (November 2017) [92],
- more than ∼5 kpc based on the relationship between the observed spin-up rate and the corresponding bolometric flux of the neutron star (December 2017) [91],
- ∼5 kpc by the optical and infrared observations of the companion star [19],
- ∼6 kpc by applying two accretion torque models on Hard X-ray Modulation Telescope (Insight-HXMT) data [93]
- $6.8^{+1.5}_{-1.1}$ kpc in Gaia Data Release 2 (DR2) catalogue [94], (this is the preferred value for some important publications about the source).
- 5.2±0.3 kpc in Gaia Early Data Release 3 (EDR3) catalogue [95, 96], (source ID: 4656281935263644l6).

Originally, assuming a source distance of ∼7 kpc yielded a peak brightness of $\sim 2 \times 10^{39}$ erg s^{-1} [81, 79, 83]. Even when using the revised distance estimate of 5.2±0.3 kpc from Gaia EDR3, the resulting peak luminosity of $\sim 1 \times 10^{39}$ erg s^{-1} remains well above the Eddington limit for the neutron star [19]. As such, Swift is recognised as the first galactic ultraluminous X-ray pulsar ever detected.

This work uses the latest Gaia distance available at the time of the analysis, 5.2±0.3 kpc. Whenever necessary, the values from other articles are normalized to this distance and this conversion is stated explicitly in the text.

It was found in previous studies that the source exhibits systematic changes in temporal and spectral properties, such as pulse profiles, energy spectra and the structure of power spectrum, at two separate luminosity transitions [81, 83, 84]. More specifically, Doroshenko et al. [83] reports these transitional luminosity levels as $L_1 \sim$

1.5×10^{37} erg s^{-1} and $L_2 \sim 4.5 \times 10^{38}$ erg s^{-1} for a 6.8 kpc distance, where L_1 was regarded as the luminosity level where the source switches from subcritical to supercritical accretion, whereas L_2 was interpreted as the luminosity level where supercritical accretion to radiation pressure dominated (RPD) disk accretion transition occurs. Adjusted to 5.2 kpc, these transitional luminosity levels become $L_1 \sim 8.8 \times 10^{36}$ erg s^{-1} and $L_2 \sim 2.6 \times 10^{38}$ erg s^{-1}. They also report some QPO features in the power spectra of the source, which begin to appear around the super-Eddington luminosity threshold reached during the Type II outburst. The QPO frequencies, $\sim$0.2 to $\sim$0.3 Hz, tend to rise with increasing luminosity, while no QPOs are detected at lower luminosity levels.

The nature of the magnetic field in Swift J0243.6+6124 remains uncertain even after considerable research. Observations indicate that the source continues to exhibit pulsations at luminosities down to 10^{34}–10^{35} erg s^{-1}, implying that the transition to the propeller regime has not occurred. Consequently, early studies argued that continued accretion at these levels implies a tightly confined magnetosphere, thus constraining the neutron star's magnetic field strength to to a maximum of 3×10^{12} G [79, 83].

Similarly, phase-resolved spectroscopy of NuSTAR data across varying luminosities points to a thick, super-Eddington disk with an inner radius of (2–3) $\times$ 10^7 cm and a reflection component showing limited variability, indicating a magnetic field strength of $\sim 3 \times 10^{12}$ G, assuming a dipolar configuration [88].

Nonetheless, a cyclotron resonance scattering feature (CRSF) was discovered in the spectrum of Swift J0243.6+6124: It is found at $\sim$120–146 keV, making the source with the highest-energy CRSF ever detected, even though it is only apparent at certain phases and highest luminosity levels [85]. Since the CRSF energy is directly proportional to the magnetic field strength, this corresponds to a surface magnetic field strength of $\sim 1.6 \times 10^{13}$ G, where the cyclotron features originated in the X-ray spectrum. Although this value is one order of magnitude higher than the estimates mentioned above, this discrepancy is attributed to the suggestion that this magnetic field strength is instead associated with localized multipole fields [85], which decay more rapidly with distance. In contrast, the large-scale dipolar magnetic field strength is suggested to be lower, estimated at (3–9) $\times$ 10^{12} G [83]. If the accretion

disk intrudes deeper into the magnetosphere than previously assumed, multipole field components may arise and dominate the disk interactions at the highest luminosity—therefore, accretion—levels [83, 85].

In 2023-04-08, Swift J0243.6+6124 was detected again at the onset of another outburst [97]. The outburst peaked in July and mostly faded by September of the same year. However, the maximum luminosity of this event was significantly lower than that of the great Type II outburst of 2017. Similar to the 2017 outbursts, pulsations with a period of $\sim$9.8 s were detected [98, 99]. Using data from the Imaging X-ray Polarimetry Explorer (IXPE) throughout this outburst, some X-ray polarization characteristics of the source were revealed, including significant phase-dependent variations in the polarization behaviour of the source [100].

This chapter focuses on the timing properties of Swift J0243.6+6124 mostly during the later, less luminous part of the 2017–2018 outbursts. Contrary to the first part of the outburst where it was much brighter, the source was in the subcritical accretion stage during this period.

4.2 Observations

Throughout its 2017–2018 outbursts, Swift J0243.6+6124 has 214 NICER/XTI (X-ray Timing Instrument) observations, taken between 2017-10-03 and 2019-06-07 (MJD 58029–58641). Of these, last 26 observations after late February 2019 (after MJD 58535) are omitted in the analysis as the source luminosity becomes too low. Therefore, 188 observations totalling $\sim$485 ks of exposure are used. The list of the observations are included in Table A.1.

Data reduction is done using HEASoft v6.29, with the latest available calibration files for NICER (CALDB release `xti20210707`). The standard pipeline processing tool, `nicerl2` and other tools mentioned in Chapter 3.1.1 are used to process the data and create light curves consequently used in timing analyses.

Apart from the NICER/XTI observations, publicly available orbit-corrected spin frequencies of Swift J0243.6+6124 by Fermi/GBM [101, 70] are used to enrich the spin

frequency history of the source. There are 225 Fermi/GBM spin frequency measurements covering 498 days from 2017-10-01 to 2019-02-11 (MJD 58027–58525).

The daily light curve of the source is taken from publicly available Swift/BAT Hard X-Ray Transient Monitor archive [102, 68]. Since the Swift/BAT light curve provides 15–50 keV count rates, converting these values to bolometric luminosity is required. Doroshenko et al. [83] noted that Swift/BAT count rates align closely with the 2–150 keV flux from Insight–HXMT, allowing them to estimate bolometric luminosity by using a scaling factor of $\sim 8.2 \times 10^{38}$ for a distance of 6.8 kpc. Following their approach, a revised scaling factor of $\sim 4.8 \times 10^{38}$ is used with a distance adjustment to 5.2 kpc, to calculate the bolometric luminosities from the Swift/BAT count rates.

4.3 Timing Analysis

Performing timing analysis of Swift J0243.6+6124 presents unique challenges. The X-ray luminosity of the source varied dramatically throughout the outbursts in 2017–2018, spanning five orders of magnitude. As different accretion regimes dominate at different luminosity levels, both the accretion geometry and the pulse profiles undergo significant changes throughout the observations [81, 83]. Notably, it has been reported that the pulse profiles of Swift J0243.6+6124 are double-peaked in subcritical regime at low luminosity levels ($L_x < L_1$), become single-peaked structures in the supercritical regime ($L_1 < L_x < L_2$), and revert to double-peaked at the peak outburst levels L_2 ($L_x > L_2$) [83]. Moreover, the excessive luminosity levels at the beginning of outburst is accompanied with the high spin-up rates of the source up to 2.2×10^{-10} Hz s^{-1} [91]. The presence of a frequency derivative of $|\dot{\nu}|$ results in a one-cycle phase shift over a time-scale of $\sqrt{2/|\dot{\nu}|}$ [103]; therefore, the reported maximum spin-up rate translates to time-scale of $\sim$1.1 d. Given that successive NICER observations at the beginning of the outburst are often separated by a couple of days (up to 15 days), and that the pulse profiles evolve throughout the outburst, it is not feasible to apply a phase-coherent timing technique under these conditions. To address this, we developed and applied a method we refer as *synthetic pulse timing*.

The synthetic pulse timing technique makes use of previously known pulse frequen-

cies that are relatively densely sampled in time. In our case, Fermi/GBM provides reliable, orbit-corrected pulse frequency measurements of Swift J0243.6+6124 (see Section 3.2.2 for the orbital correction of pulse frequencies), which are useful for deriving more precise pulse frequencies from the NICER observations.

First, Fermi/GBM measurements are divided into four segments, chosen in such a way that each exhibits relatively simple frequency evolution. Each segment is then fitted by a polynomial model to interpolate the frequency evolution of the source. While higher-degree polynomials provide a better fit, increasing the model complexity offers only marginal improvement beyond a certain point. Each polynomial model is a synthetic timing solution of this segment. At this point, it should be noted that both the number of segments and the degree of the polynomials used in the fits are somewhat arbitrary choices. Still, the synthetic residual reconstruction compensates for deviations from the chosen model, as long as the reconstructed pulse profiles are consistent with the observed ones. The parameters of the synthetic timing solutions for each interval are provided in Table 4.1.

These timing solutions are then used to determine the frequency residuals by comparing the Fermi/GBM frequencies against the model. Afterwards, the residuals are interpolated with a linear spline and the spline is integrated to obtain synthetic phase residuals:

$$\Phi_r(t) = \int_{t_0}^{t} \nu_r(t')\,\mathrm{d}t', \tag{4.1}$$

Here, the synthetic phase residual model is denoted by $\Phi_r(t)$, frequency residuals by $\nu_r(t')$ and t_0 marks the segment start time. Thus, while the synthetic timing solution models the segment with some deviations from the original frequencies, the frequency or phase residuals are used to correct for the deviations. The combined timing solution and the phase residual model can then be used to measure the pulse frequencies of an another data set within the same time interval.

This approach is more powerful than using the `efsearch` tool: `efsearch` disregards the frequency evolution of the source and whose precision is limited by the duration of the individual light curve. Our approach incorporates frequency evolution and connects multiple observations, thereby it yields significantly more reliable frequency estimates.

Converting a polynomial model to a timing solution is straightforward. The polynomial model is simply

$$y = c_0 + c_1 x + c_2 x^2 + c_3 x^3 + ... + c_A x^A = \sum_{n=0}^{A} c_n x^n, \tag{4.2}$$

where A is the order of the polynomial. Similarly, the frequency evolution of the source can be described as:

$$\nu(t) = c_0 + c_1(t-t_0) + c_2(t-t_0)^2 + c_3(t-t_0)^3 + ... + c_A(t-t_0)^A = \sum_{n=0}^{A} c_n(t-t_0)^n, \tag{4.3}$$

where x is exchanged with $(t - t_0)$, where t is the time and t_0 is time epoch (both in MJD days). This is similar to the frequency evolution formula in terms of frequency and frequency derivatives (which is actually a Taylor expansion):

$$\nu(t) = \nu_0 + (t-t_0)\dot{\nu} + \frac{1}{2!}(t-t_0)^2\ddot{\nu} + \frac{1}{3!}(t-t_0)^3\dddot{\nu} + ... = \sum_{n=0}^{\infty} \frac{1}{n!}(t-t_0)^n \frac{d^n\nu}{dt^n}, \tag{4.4}$$

(also see Equation (3.10)). While modelling the frequency evolution, a finite number of terms (i.e., frequency derivatives) are used and the higher order terms are ignored. Selecting the number of terms used for modelling is rather arbitrary: The synthetic timing solution is just a guide to pulse-connect the subsequent observations; therefore, as long as using a specific number of terms to the model yields a sufficiently coherent fit so that the discrepancy between the model and the spin frequencies results less than a single phase shift over the modelling time span, adding more terms is considered unnecessary. Then, we can convert the fit parameters c_n of the polynomial model to frequency and frequency derivatives as

$$\nu_0 = c_0, \frac{d^n\nu}{dt^n} = n! \frac{c_n}{86400^n}. \tag{4.5}$$

As the unit of time is days in Equation (4.3), and seconds in Equation (4.4), an extra factor of 86400^n is included.

In our case, the orbitally corrected NICER light curves are folded using the same synthetic timing solutions, using 20 phase bins for each observation, then their phase residuals are computed.

The first interval exhibits substantial luminosity changes in the source; as a result, the polynomial modelling leads to considerable deviations from the rapid frequency evolution. Nevertheless, after applying the appropriate integer phase shifts, the NICER

Table 4.1: Timing parameters of Swift J0243.6+6124 for four different intervals. The synthetic timing solutions are derived by fitting the existing Fermi/GBM frequencies. The units of the rows are as follows: Timing range and epoch, MJD; ν, Hz; $d\nu/dt$, 10^{-10} Hz s^{-1}; $d^2\nu/dt^2$, 10^{-17} Hz s^{-2}; $d^3\nu/dt^3$, 10^{-24} Hz s^{-3}; $d^4\nu/dt^4$, 10^{-29} Hz s^{-4}; $d^5\nu/dt^5$, 10^{-34} Hz s^{-5}; $d^6\nu/dt^6$, 10^{-41} Hz s^{-6}; $d^7\nu/dt^7$, 10^{-47} Hz s^{-7}.

	Interval 1	Interval 2	Interval 3	Interval 4
Timing range	58027–58162	58162–58239	58299–58497	58450–58531
Epoch	58050	58200	58350	58500
ν	0.1015335(20)	0.1021289(2)	0.1021046(2)	0.10210146(7)
$d\nu/dt$	1.02(2)	−0.0161(4)	−0.0180(9)	0.0730(10)
$d^2\nu/dt^2$	9.85(31)	−0.0109(45)	0.0265(36)	−0.408(13)
$d^3\nu/dt^3$	−4.94(35)	-	−0.0158(32)	−4.52(23)
$d^4\nu/dt^4$	−9.86(90)	-	−0.0139(22)	0.359(29)
$d^5\nu/dt^5$	1.58(11)	-	0.000556(51)	0.0369(41)
$d^6\nu/dt^6$	−9.77(66)	-	-	−0.114(59)
$d^7\nu/dt^7$	2.41(17)	-	-	-

phase residuals align with the synthetic residual model. The only complication comes from variations in the pulse profiles between different episodes [83], which require further correction. Accordingly, to match the synthetic phase residuals, we make an exception by allowing half-integer phase shifts in the supercritical regime, reflecting the phase offset between the double- and single-peaked profile peaks (see Figure 4 [83]). The bottom panel of Figure 4.1 illustrates the outcome of applying these phase shifts.

In contrast, during the late stages of the outburst (intervals 2, 3, and 4), the source exhibits lower luminosity ($L_x \lesssim 8 \times 10^{37}$ erg s^{-1}) and accretes exclusively in the subcritical regime ($L_x < L_1$). Consequently, the synthetic phase residuals stay confined within a single cycle for the respective synthetic timing solutions provided in Table 4.1.

Synthetic timing solutions are ultimately intended for measuring pulse frequencies. This is done by using each successive pair of pulse arrival times in the NICER phase

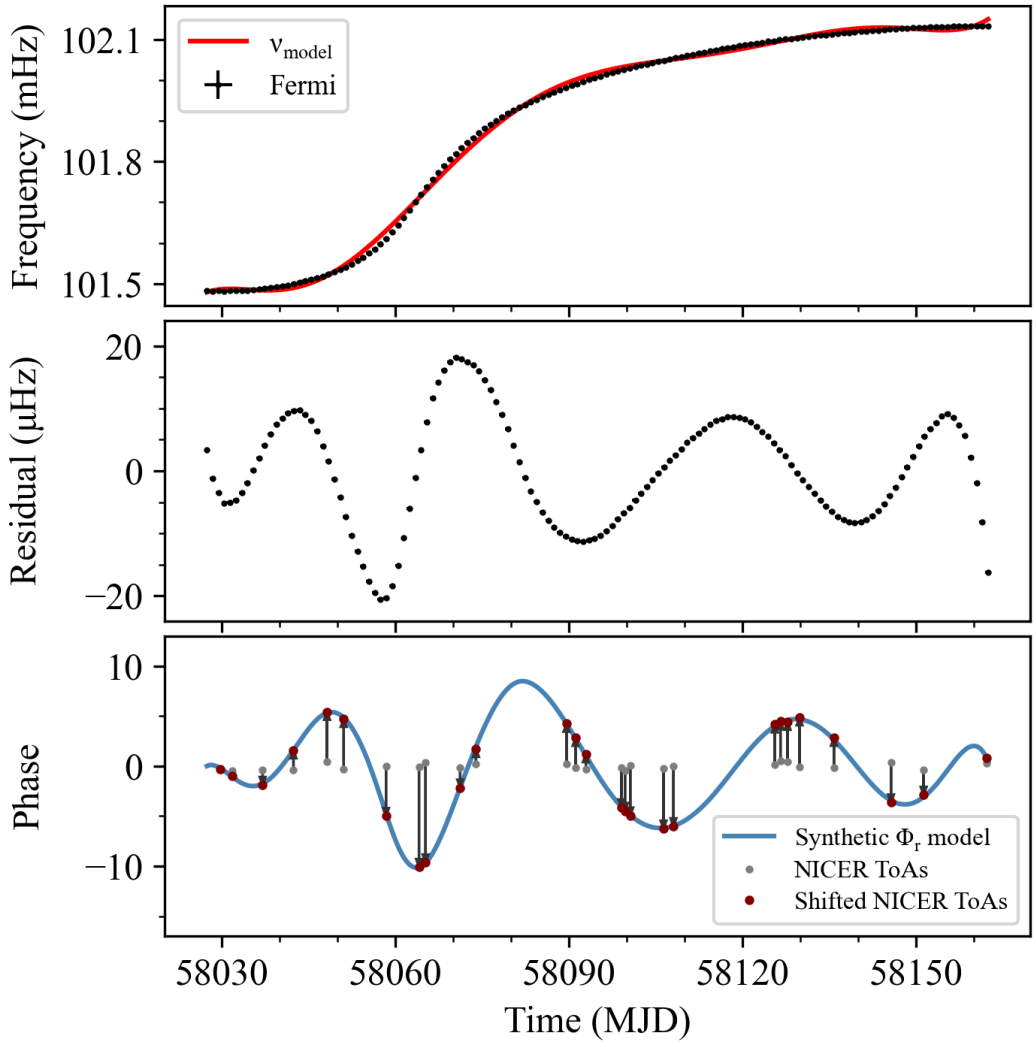


Figure 4.1: Upper panel: Spin frequency history from Fermi/GBM (black dots) alongside the synthetic timing solution (red curve), derived from polynomial fitting in interval 1 (see Table 4.1 for timing parameters). Middle panel: Frequency residuals relative to the synthetic timing solution. Lower panel: Synthetic phase residual model derived from Fermi/GBM residuals (blue curve), time of arrival (ToA) residuals from NICER observations (gray dots) obtained by folding with the corresponding timing solution, and the phase-shifted NICER ToA residuals (red dots) aligned to match the synthetic phase residual model.

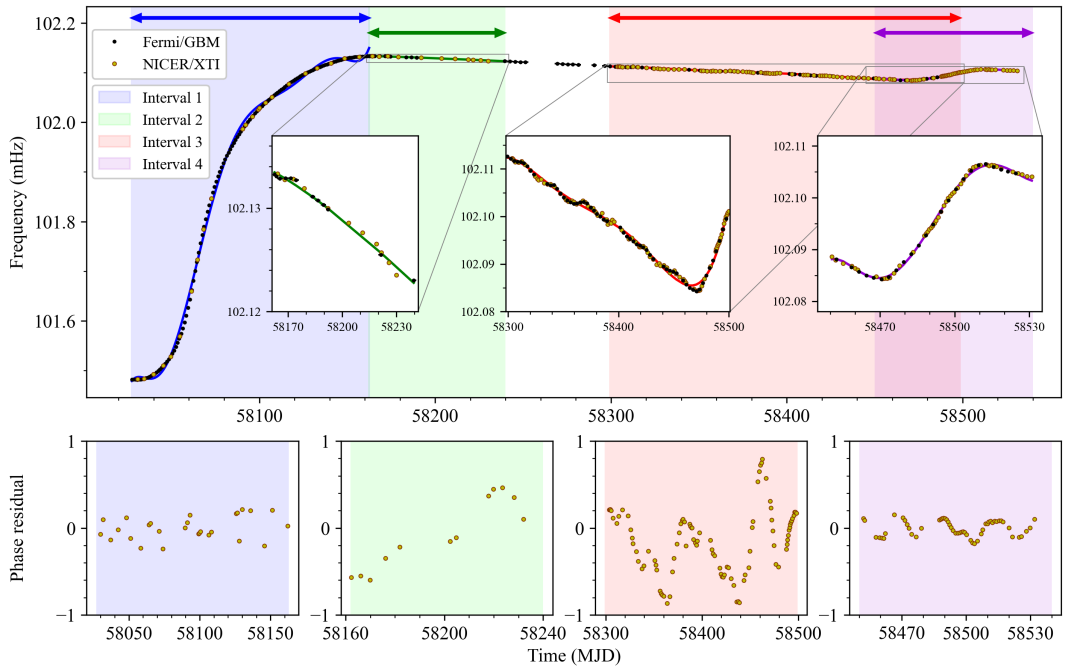


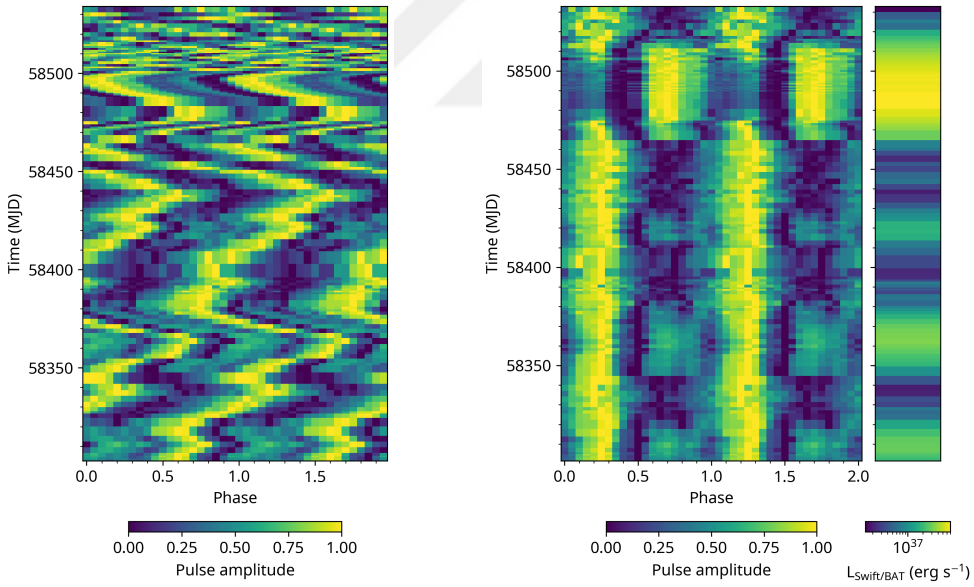
Figure 4.2: Top panel: The spin frequency history of Swift J0243.6+6124 constructed over the full 2017–2018 outburst. Colored arrows and shaded regions indicate the time intervals used for the synthetic timing solution models. Inset panels display zoomed-in views of selected regions for clarity. Bottom panels: NICER ToA phase residuals of the synthetic timing solutions.

residuals. A linear fit of the form $\delta\nu = \delta\phi/(t_2 - t_1)$ is applied to each pulse pair, where t_1 and t_2 are the arrival times of the first and second pulses, and $\delta\phi$ is the phase offset between them. Each linear fit is converted into a spin frequency measurement at the midpoint of the respective interval by applying the frequency correction $\delta\nu$ to the synthetic timing solutions [104, 73]. The 1σ uncertainty of the fit slopes serve as the error estimates of the spin frequency measurements. As shown in Figure 4.2, the spin frequency measurements from NICER observations are consistent with those reported by the Fermi/GBM Accreting Pulsars Program team.

In addition to the initial spin-up phase of the Type II outburst, Figure 4.2 indicates that Swift J0243.6+6124 continues to spin up during MJD ∼58470–58510 as well. As the flux declines over time, the source transitions back to a spin-down phase, with an average derivative of $\sim -1.6 \times 10^{-12}$ Hz s^{-1}, similar to the earlier average spin-down rate of $\sim -1.8 \times 10^{-12}$ Hz s^{-1} over MJD 58150–58460.

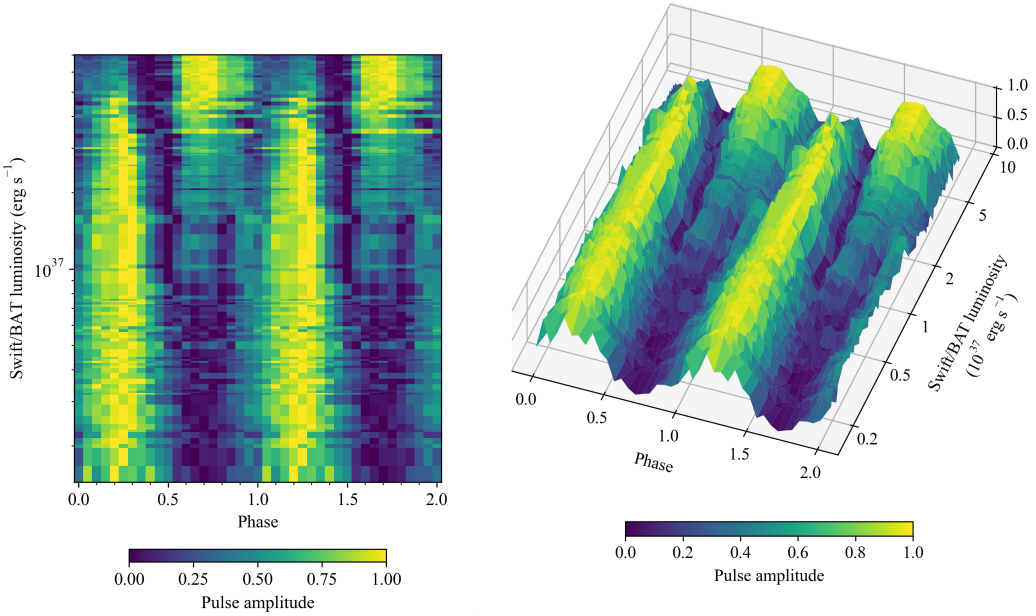
The luminosity-sorted pulse profiles during the early phase of the outburst (MJD $\sim$ 58030–58160) were previously studied by Doroshenko et al. [83]. Here, our analysis focuses on profiles obtained after MJD 58300, representing the later, lower-luminosity phase of the outburst (see Figure 4.4). Double-peaked pulses are visible at higher luminosity levels as reported earlier. As the luminosity decreases, the main peak slowly weakens and is no longer detectable below $\sim 7 \times 10^{36}$ erg s^{-1}. This may represent a previously unidentified transition in the accretion geometry. It is worth noting that this luminosity threshold corresponds with the level below which the spin-up behaviour reverses to spin-down.

Additionally, the evolution of the spin frequency of Swift J0243.6+6124 is investigated using a torque–luminosity model. The spin frequency derivatives are calculated by taking three consecutive spin frequency measurements and applying a linear fit. The publicly available daily light curve from Swift/BAT is used to determine the flux levels of the source. In order to align the timing of the Swift/BAT data with the spin



(a) (b)

Figure 4.3: Time-sorted pulse profiles of Swift J0243.6+6124 for observations after MJD 58300 (a) before the alignment, and (b) after the alignment. For clarity, the pulse profiles are normalized to a [0, 1] scale and displayed over two cycles.



(a) (b)

Figure 4.4: Luminosity-sorted pulse profiles of Swift J0243.6+6124 for observations after MJD 58300, (a) in 2D and (b) in 3D. Swift/BAT luminosities are in the 15–50 keV range. For clarity, the pulse profiles are normalized to a [0, 1] scale and displayed over two cycles.

frequency derivatives, linear spline interpolation is applied to estimate the flux at specific time points. The relationship between the frequency derivatives and luminosity is shown in Figure 4.5. This relationship is modelled with a power law as mentioned in Section 3.2.3. A modification to Equation (3.16) involves the addition of a constant term, as the low-luminosity regime of Swift J0243.6+6124 is characterised by a regular spin-down. Consequently, resulting fitted function becomes

$$\dot{\nu}_{intrinsic} = \beta L_x^{\alpha} + \nu_{sd}, \tag{4.6}$$

where the constant ν_{sd} represents the spin-down behaviour. The power law exponent of the fit is found to be $\alpha = 1.231 \pm 0.014$, ehich is close to the value predicted by the Ghosh & Lamb model ($\alpha = 6/7$). Using luminosity of the source and Equation (3.17), the spin frequencies are then reconstructed. The modelling proves to be highly successful, despite the complex variations in both frequency and luminosity over $\sim$500 days, as well as gaps in the spin frequency measurements. The results of the intrinsic

spin frequency modelling are presented in Figure 4.6.

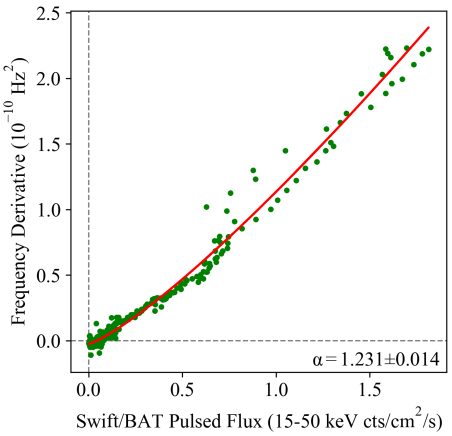


Figure 4.5: Relation between the measured spin-up rates and the 15–50 keV luminosity of sw from Swift/BAT data. The red line represents the best-fit model.

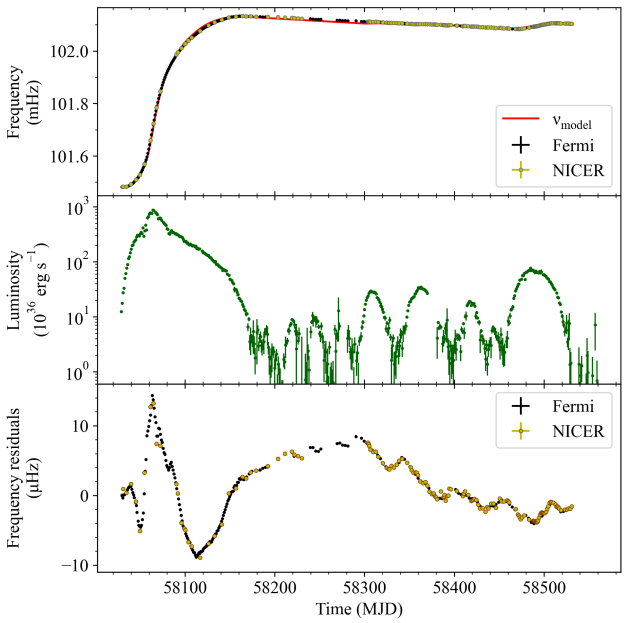


Figure 4.6: Top panel: Fermi/GBM (black) and NICER/XTI (yellow) spin frequency measurements of Swift J0243.6+6124, alongside the intrinsic spin frequency model (red line). Middle panel: Swift/BAT luminosity of Swift J0243.6+6124 over time in 15–50 keV band with d = 5.2 kpc. Bottom panel: Spin frequency residuals of Swift J0243.6+6124.

CHAPTER 5

MXB 0656–072

5.1 Introduction

MXB 0656–072 is a Be-type X-ray binary in Milky Way. It is located at 6h 58m 17.29s, -7° $12'$ $35.20''$ [105], in the constellation Monoceros. It was first detected in late 1975 by the SAS-3 Group (Small Astronomy Satellite 3), and described as a "soft X-ray transient" at the time [106]. In early 1976, the source flux was reported to be 50–70 mCrab in the 3–6 keV range [107]; however, it wasn't observed again until 2000s, yet remained listed in several catalogues [108, 109].

On 2003-10-18 (MJD 52930), an outburst was detected by RXTE/ASM [110], which lasted until December of the same year. It was during this period that the true nature of the source began to be uncovered. It was reported that a neutron star with a spin period of 160.7 s resides in MXB 0656–072 [111]. The donor star of the source is "a variable reddened Be star" RX J065817.7–071228, of a spectral type O9.7Ve, having a magnitude of 12.1–12.4 mag; therefore it is established that MXB 0656–072 is indeed a Be type high mass X-ray binary [112]. Based on RXTE observations obtained during the 2003 outburst, McBride et al. [113] identified the event as a Type II outburst (also see e.g., [10]). They also detected a CRSF in the spectra at $\sim$33 keV, consistent with an earlier report of a cyclotron line around 35 keV [114]. This corresponds to a magnetic field strength of $\sim 3.7 \times 10^{12}$ G. Their phase-resolved spectral analysis revealed that while the CRSF width changed with pulse phase, the CRSF energy remained constant. Their distance estimation at the time was 3.9 ± 0.1 kpc, inferred by optical observations. Yet, the newer Gaia EDR3 catalogue puts the source further away, at a the distance of 5.7 ± 0.5 kpc (Source ID: 3052677318793446016)

[95, 96]; and this distance value is used in the thesis work.

Following the 2003 outburst, the only activity of MXB 0656–072 observed to date is a series of Type I outbursts, each separated by ∼100 days, between November 2007 and November 2008. The outbursts were observed by INTEGRAL [115], RXTE [116, 117], Swift [118, 117], and Fermi [119]. Combined RXTE/PCA and HEXTE spectra on MJD 54632 (2008-06-15) revealed a broad CRSF at ∼30 keV, while the source luminosity in 3–22 keV range was 6.6×10^{36} erg s^{-1} (assuming a 3.9 kpc distance) [120]. Evaluating RXTE/ASM and Swift/BAT light curves, the same study inferred the orbital period as ∼101.2 d, but no orbital parameters were presented. Besides, Nespoli et al. (2012) reported the multiwavelength variability of the source, as well as spectral analysis results from RXTE/PCA (both 2003 and 2007–2008 outbursts) and RXTE/HEXTE (2003 observations). Their observation of anti-correlation between the source flux and photon index resulted a conclusion that there may be a transition luminosity around 2.3×10^{37} erg s^{-1} for an assumed distance of 3.9 kpc (∼4.9×10^{37} erg s^{-1} when scaled to 5.7 kpc).

Spectral modelling of the 2003 and 2007–2008 outbursts commonly includes an absorbed cutoff power law (either `powerlaw*highecut` or `cutoffpl` [121]), a CRSF feature at ∼30–36 keV, and a Gaussian iron line at ∼6.4 keV [113, 120, 122]. Additional components included a blackbody model [113], and a Gaussian absorption feature around 10 keV, introduced to address residuals of unclear origin [120, 122]. In addition to its outburst phases, the quiescent state of MXB 0656–072 has been explored as well using Chandra [123] and NuSTAR [124] data.

5.2 Observations

The analysis presented in this thesis investigates Type I outbursts of MXB 0656–072 occurred in 2007–2008, using data from RXTE/PCA [62] observation sets P93032 and P93423. These observation sets, spanning from 2007-11-14 to 2008-11-18, contain a total of 172 observations. Excluding one observation with no exposure, 171 observations were used in the analysis, with a total exposure of 438 ks. The list of the observations are included in Table A.2.

The RXTE/PCA observations were processed using HEASoft v6.31, and light curves in 3–20 keV energy range are created. Details of the data processing steps are provided in Section 3.1.2.

In order to evaluate the correlation between the frequency derivative and luminosity of the source, its flux history is required. For this purpose, the 3–20 keV flux measurements from the same RXTE/PCA observations used in [2] are utilized. These measurements are reported to have been obtained by fitting each spectrum with an absorbed power law model, including a high-energy cutoff and/or a Gaussian iron line at 6.4 keV when necessary, and calculating the unabsorbed flux, which is then converted to luminosity assuming a distance of $\sim$5.7 kpc.

Apart from the RXTE/PCA observation set, Fermi/GBM had a limited history of spin frequencies of MXB 0656–072. 6 spin frequency measurements around MJD 54740 cover $\sim$20 days near the end of the outburst sequence [119] (see Figure 5.3).

5.3 Timing Analysis

We used statistically independent trial frequencies to fold the RXTE/PCA light curve and determine a nominal spin frequency [125]. This process allowed us to search for the best-fitting spin frequency in a statistically robust manner. To generate pulse profiles, the light curves were folded at the nominal spin period, using 20 phase bins per observation. If the subsequent observations are less than one day apart, they are merged and a single pulse profile is created. Each pulse profile is expressed in terms of Fourier harmonics and cross-correlated with a template profile (see Section 3.2.2). The template profile is chosen as the one with the highest overall χ^2 value among them. This way, the ToAs of the pulses are calculated and pulses are aligned by cross-correlating them with the methods mentioned in Section 3.2.2. The alignment process is separately done with an already available C script and a self-written Python script, both of which returned the same results. The pulse profiles, sorted by luminosity, are presented in Figure 5.1.

Throughout the entire outburst, the pulse profiles maintain a single-peaked structure and show no substantial changes in shape, except at the lowest luminosity levels.

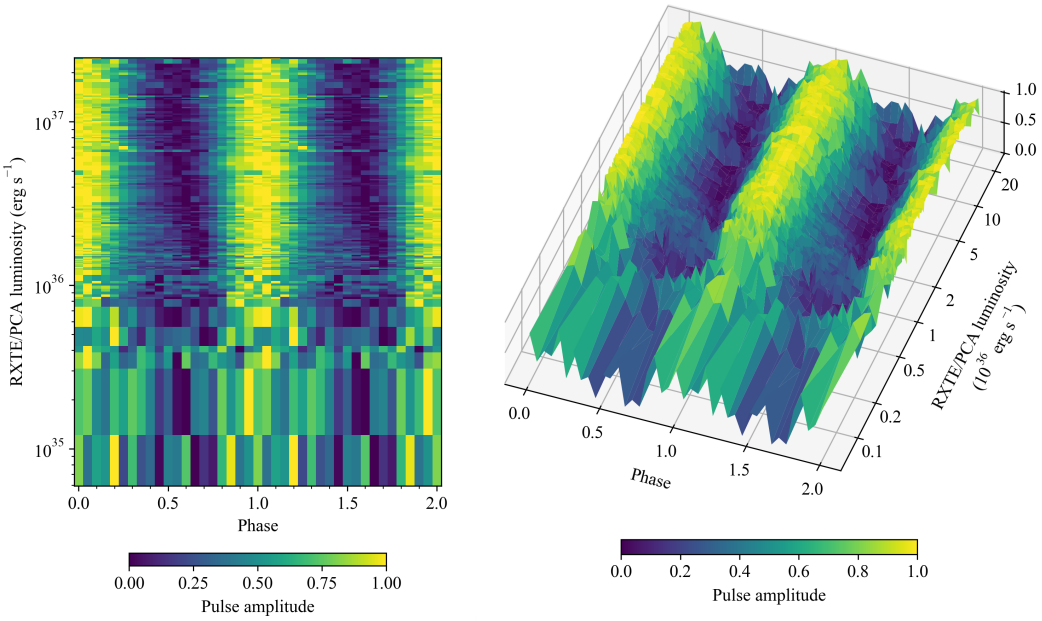


Figure 5.1: Luminosity-sorted pulse profiles of MXB 0656–072 in 2D (a) and 3D (b). RXTE/PCA luminosities are in the 3–20 keV range. The pulse profiles are normalized to the [0, 1] range and plotted over two cycles for clarity.

The pulsed emission disappears in the final few observations, where the luminosity falls below $\sim 5 \times 10^{35}$ erg s^{-1}. The loss of detection is attributed to a reduced SNR, caused by reduced count rates in the detector. It is important to note that the source luminosity does not exceed $\sim 2 \times 10^{37}$ erg s^{-1} in the data set analysed since the 2007–2008 events are Type I outbursts with relatively low luminosity. Accordingly, the interpretations presented are based on the 10^{36}–10^{37} erg s^{-1} luminosity range.

It was particularly challenging to track and display the pulse ToAs during enhanced accretion episodes of Type I outbursts, which lead to rapid variations in the spin frequency. To account for the dominant spin-up behaviour, we subtract the overall spin-up trend Φ_{su}

$$\Phi_{su} = \nu + \dot{\nu}(t - t_{epoch}) \tag{5.1}$$

where the epoch t_{epoch} = MJD 54598.05, the frequency ν = 6.271 28(6) mHz and the frequency derivative $\dot{\nu} = 1.14(2) \times 10^{-12}$ Hz s^{-1}. Following the subtraction, the

resulting pulse ToAs are shown in Figure 5.2.

Although these ToAs are intended for generating a phase-coherent timing solution, their complex evolution made high-order polynomial modelling impractical. Rather than using high-order polynomial modelling, frequencies are computed by fitting linear functions to successive ToA triplets. Each ToA triplet is fitted by a linear function, yielding a frequency correction $\delta\nu = \delta\phi/\delta t$ which is applied to the spin-up trend (Equation (5.1)) at the midpoint of the ToA triplet. As a result, the spin frequency history of the RXTE/PCA observations are generated, providing a substantial enhancement to the limited Fermi/GBM measurements (Figure 5.3). Frequency measurement uncertainties are derived from the 1σ errors of the fitted slopes, and the uncertainties in time correspond to the time intervals covered by each ToA triplet.

5.3.1 Torque–luminosity correlation

MXB 0656–072 shows persistent spin-up across the outburst sequence. While spin frequencies seem to modulate around the proposed orbital period ($\sim$101.2 days by Yan et al. [120]), superimposed on an overall spin-up trend, this interpretation requires caution. While spin-up rate increases are observed during outbursts, a sustained spin-up trend continues even during the quieter phases between Type I outbursts. We therefore investigate how the torque from accretion influences the intrinsic evolution of the pulsar's spin frequency.

As a first step, spin frequency derivatives were estimated using linear fits applied to consecutive $\sim$20-day intervals in the frequency history, using a method similar to that outlined in the previous section. Because the timing of the RXTE/PCA flux data does not coincide with that of the spin frequency derivative measurements, a linear spline interpolation is applied to estimate the flux values corresponding to those intervals. Figure 5.4 illustrates a clear relationship between the spin-up rates and the corresponding flux values. The spin-up rate shows a positive correlation with luminosity, peaking at around 4×10^{-12} Hz s^{-1} at the maximum luminosity of outbursts. For comparison, a time-averaged spin-up rate of $\sim 4.52(13) \times 10^{-12}$ Hz s^{-1} has been reported for the 2003 Type II outburst, with an average luminosity of $1.4(8) \times 10^{37}$ erg s^{-1} (adjusted for a distance of 5.7 kpc) [113], consistent with our results.

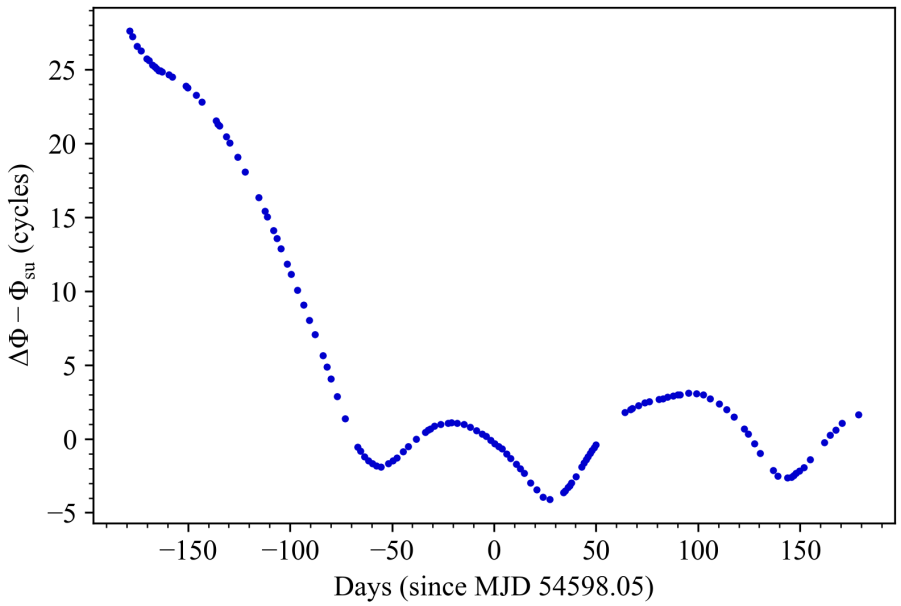


Figure 5.2: Time of arrivals (ToAs) of pulses from RXTE/PCA observations of MXB 0656–072, with the long-term spin-up trend removed.

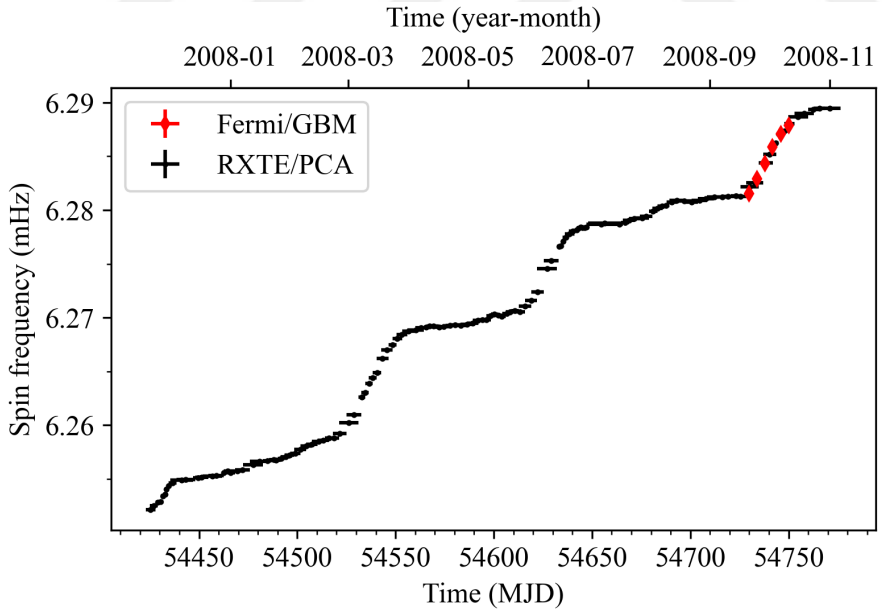


Figure 5.3: Reconstructed spin frequency history of MXB 0656–072 derived from RXTE/PCA data (black points), shown alongside publicly available Fermi/GBM measurements (green diamonds).

The correlation between accretion torques and X-ray luminosity is modelled with a power-law profile, using the methodology described by Galloway et al. [72] and referenced in Section 3.2.3. A power-law fit results in an exponent of $\alpha = 0.88 \pm 0.03$ (1σ confidence), closely matching the Ghosh–Lamb model prediction of $\alpha = 6/7$.

Since MXB 0656–072 has a long spin period (i.e., it is a "slow rotator": $P_{spin} \sim 160$ s), the fastness parameter defined in Equation (2.10) is much smaller than unity ($\omega_s \ll 1$). Consequently, the effect of the curvature by the dimensionless torque function $n(\omega_s)$ (defined in Equation (2.12)) on the fit is negligible within the studied luminosity range. Also, given that the source luminosity stays mostly above 10^{36} erg s^{-1} throughout the observations, variations between torque models [126, 127] have minimal impact on the torque modelling or the derived spin frequency residuals. For all these reasons, Ghosh & Lamb's model [37] is used for the rest of the analysis and the power law exponent of the fit is frozen to 6/7. The best fit of model $\dot{\nu} = \beta L_{37}^{6/7}$

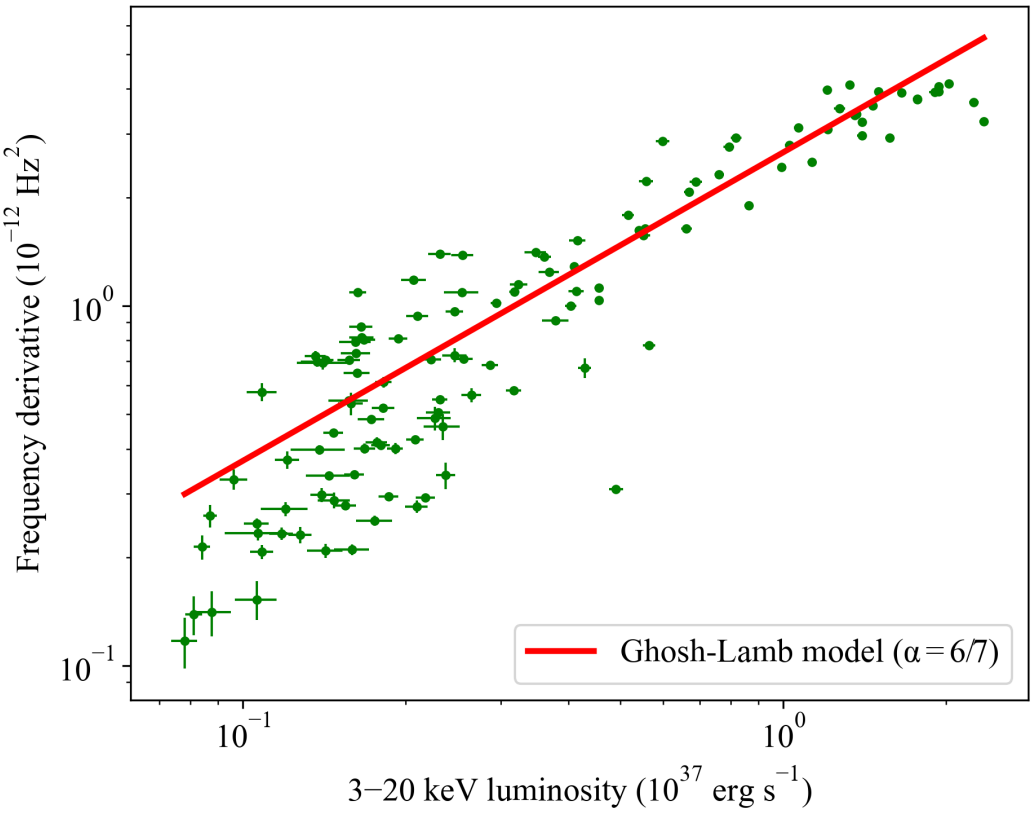


Figure 5.4: Relation between the measured spin-up rates and the 3–20 keV luminosity of MXB 0656–072 from RXTE/PCA data. The red line represents the best-fit model.

as given in Equation (3.16) (L_{37} is the luminosity in 10^{37} erg s^{-1}), gives β = 2.42(6) (1σ confidence). Equation (3.17) is then used to model the intrinsic spin frequency evolution due to the accretion process, and the residual frequencies after removing the intrinsic spin frequency model are created. Both the resulting model and the residual frequencies, along with the source luminosity at 5.7 kpc, are presented in Figure 5.5. Although the residuals appear to exhibit some structure, it cannot be confidently interpreted as an orbital modulation. Even if the power law exponent is not fixed to 6/7 and set free instead, the results are similar. Therefore, modelling the torque–luminosity relation and deriving spin frequency residuals from the data set is not sufficient to confidently determine the orbital parameters of MXB 0656–072.

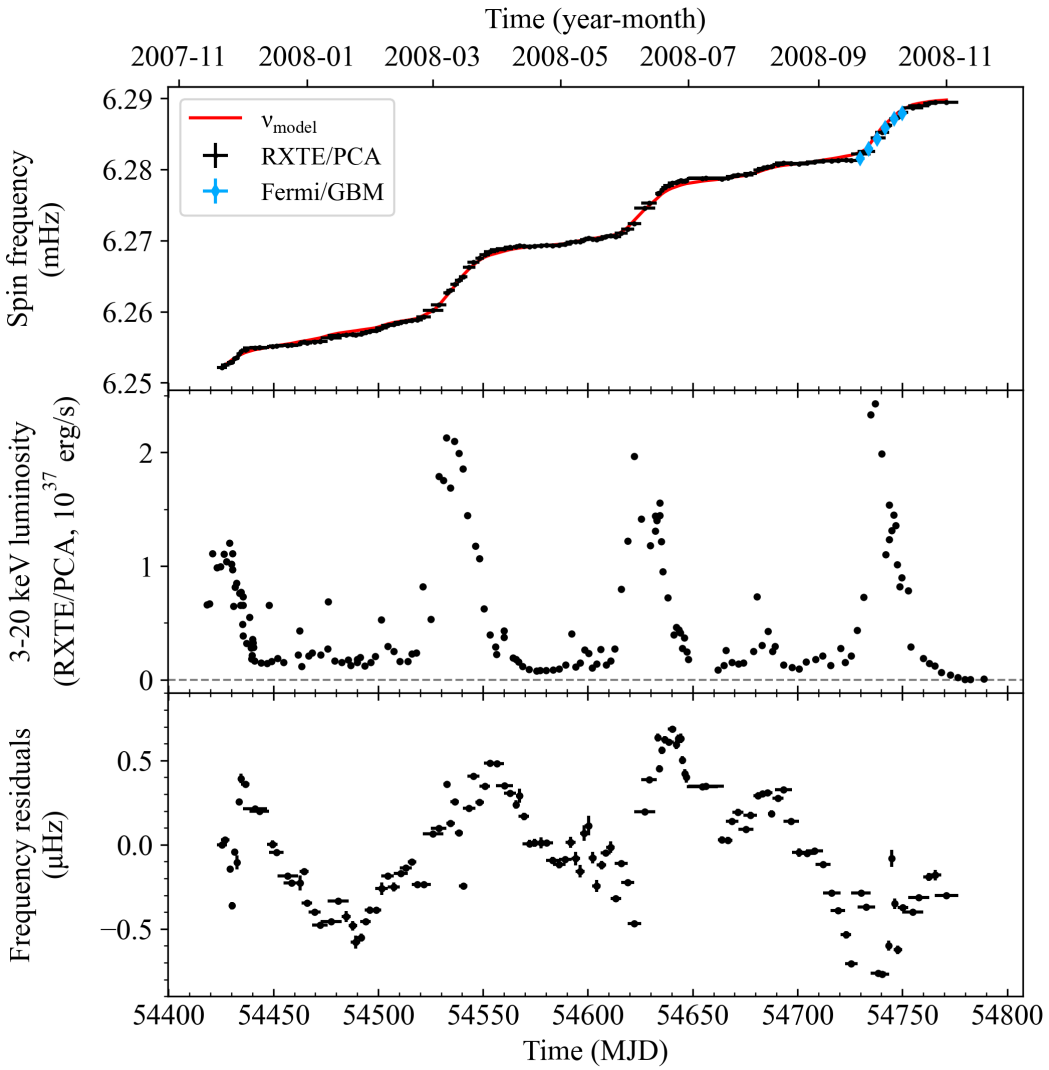


Figure 5.5: Top panel: RXTE/PCA (black) and Fermi/GBM (green) spin frequency measurements of MXB 0656–072, alongside the intrinsic spin frequency model (red line). Middle panel: RXTE/PCA luminosity of MXB 0656–072 over time in 3–20 keV band with d = 5.7 kpc. Bottom panel: Spin frequency residuals of MXB 0656–072.

CHAPTER 6

GRO J1008–57

6.1 Introduction

GRO J1008–57 is a Be type X-ray binary, discovered in 1993 [128]. It is located at 10h 09m 46.96s, -58° $17'$ $35.60''$ [129], in the constellation Carina. The system consists of a pulsar with a $\sim$93.6 s spin period (at the time of the discovery) [128]. The discovery of a OB type optical counterpart with infrared excess suggests that the source is a BeXB [130], and later studies indicate the donor star is indeed of B1–B2 Ve type [131].

GRO J1008–57 is characterised by its regular Type I outbursts, interspersed with occasional Type II outbursts. The regularity of Type I outbursts suggests an orbital period of $\sim$250 days, and the orbit period estimate of 247.8$\pm$0.4 d [131] is last refined as $249.48^{+0.04}_{-0.04}$ d [133]. The latest orbital parameters suggest that the Type I outbursts reach a maximum at an orbital phase of $\phi_{orb} = -0.0323(17)$, corresponding to 8.06(42) d before the periastron [133]. The orbit is determined to be eccentric, with an orbital eccentricity $e = 0.68 \pm 0.02$ [131]. However, the most current orbital solution does not completely match the extended recent data set; therefore, a further refinement is needed [70], at least in the orbital period.

Various CRSF detections in the energy spectra of the source put the CRSF energy at 88$\pm$5 keV in CGRO/OSSE (Compton Gamma Ray Observatory, Oriented Scintillation Spectrometer Experiment instrument) data [134], 76$\pm$2 keV in Suzaku/HXD (Hard X-ray Detector) data [135], 78^{+3}_{-2} keV in NuSTAR and Suzaku data [136], and 90.3$\pm$0.3 keV in HXMT data [137], implying an magnetic field strength of (7–8) $\times$ 10^{12} G. Until the detection of a CRSF in the energy spectra of Swift J0243.6+6124,

GRO J1008–57 had the highest energy of a fundamental CRSF and inferred magnetic field strength in all accreting pulsars [136].

The distance estimates of the system are quite variable. An initial estimate of 2 kpc [138] was later challenged to 9.7±0.8 or 5.8±0.5 kpc [139]. Yet, the Gaia EDR3 catalogue yields a 3.6±0.2 kpc source distance (Source ID: 5258414192353423360) [140] and this distance value is used throughout our analysis.

Energy-resolved pulse profiles of the source during various Type I and II outbursts created by Suzaku/HXD and HXMT data indicate that, while the pulse profiles are double-peaked in 3–10 keV energy range, they evolve into a single-peaked profile above 10 keV [135, 137, 141]. X-ray polarimetry of the source by IXPE during a Type I outburst in 2022 revealed that the magnetic obliquity of the source is ∼75°; therefore GRO J1008–57 is "a nearly orthogonal rotator" [142]. The same study determined

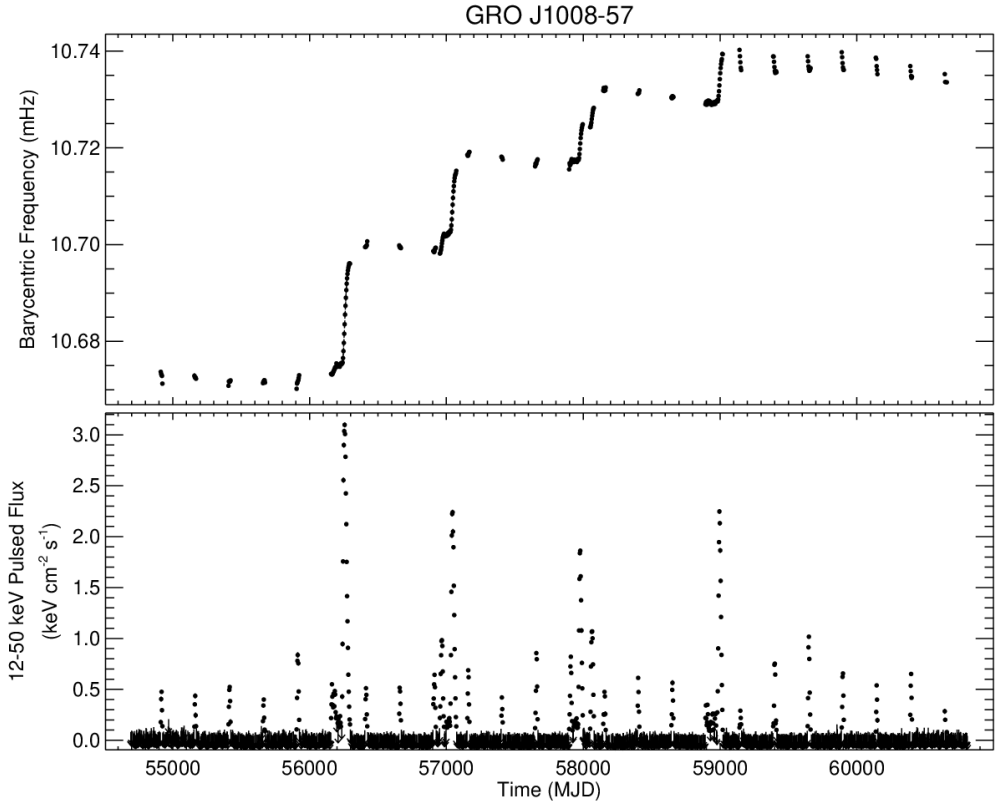


Figure 6.1: Pulse frequency and pulsed flux history of GRO J1008–57 by Fermi/GBM [132].

that the source polarization doesn't depend on the source flux and stays at $\sim$4%, and that this can be explained by a overheated neutron star atmosphere model. The observations at the quiescent state between two consequent Type I outbursts revealed that as the source luminosity drops to 10^{34} erg s^{-1} levels, the source does not enter into a propeller state but a stable accretion from a cold disk ($T < \sim$6500 K, the hydrogen recombination limit) continues instead [143].

6.2 Observations

While GRO J1008–57 has regular Type I outbursts and occasional Type II outbursts, its Type II outburst in 2020 is studied for the scope of this thesis. NICER/XTI has 46 observations during this outburst, between 2020-04-08 and 2020-06-26 (MJD 58947–59022), with a total of $\sim$150 ks exposure. The list of observations are included in Table A.3.

The observations are processed with HEASoft v6.31.1, with the latest available calibration files for NICER (CALDB release `xti20221001`). The data reduction steps are done as outlined in Section 3.1.1, and the resulting light curve is used for timing analysis of the source. Note that the energy range of the constructed light curve is 0.5–10 keV, and the light curve is created with a timing resolution of 0.125 s. As a reference, NICER count rates of the source binned daily are presented in Figure 6.2.

Even though the daily-binned NICER light curve gives an insight into the outburst intensity, spectral modelling is needed to obtain the flux levels of the source (and then convert it to corresponding luminosity using the distance d = 3.6 kpc). Furthermore, the NICER/XTI light curve is up to 10 keV, limiting the spectral cutoff modelling accuracy at higher energies. Therefore, the luminosity of the source is derived from the publicly available data set from the Swift/BAT X-Ray Transient Monitor archive [144]. The daily flux measurements at 15–50 keV is proven reliable to estimate bolometric luminosity of several similar sources before [145, 83, 73], including Swift J0243.6+6124 (Chapter 4.2, [1]). A scaling factor of $\sim 6 \times 10^{-8}$ is used to convert the Swift/BAT count rates to the reported flux measurements from spectral modelling in Kühnel et al. [146], and corresponding luminosity values are calculated assuming a

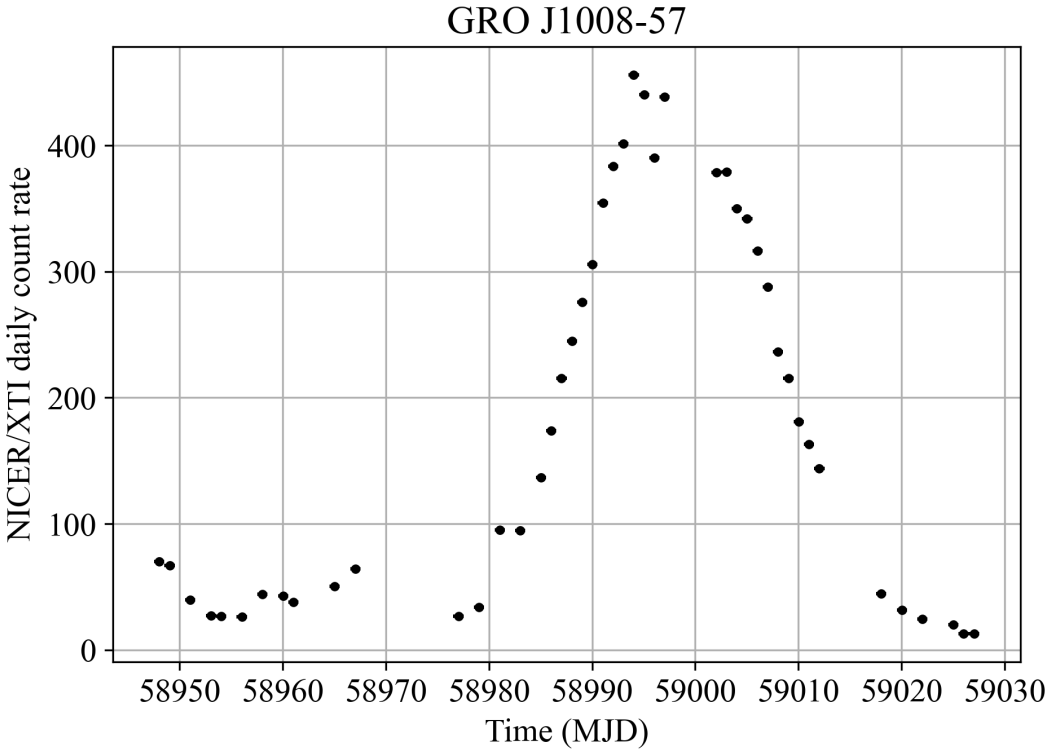


Figure 6.2: NICER/XTI daily count rates of GRO J1008–57.

3.6 kpc source distance.

As a complement to the to-be-acquired spin frequencies from the NICER light curve, the publicly available pulse frequencies measured by Fermi/GBM are also collected [132] (Figure 6.1). However, as it is explained in more detail in the next section, this data set is not utilised in the long run due to the inconsistencies in the orbit-correction of the data.

6.3 Timing Analysis

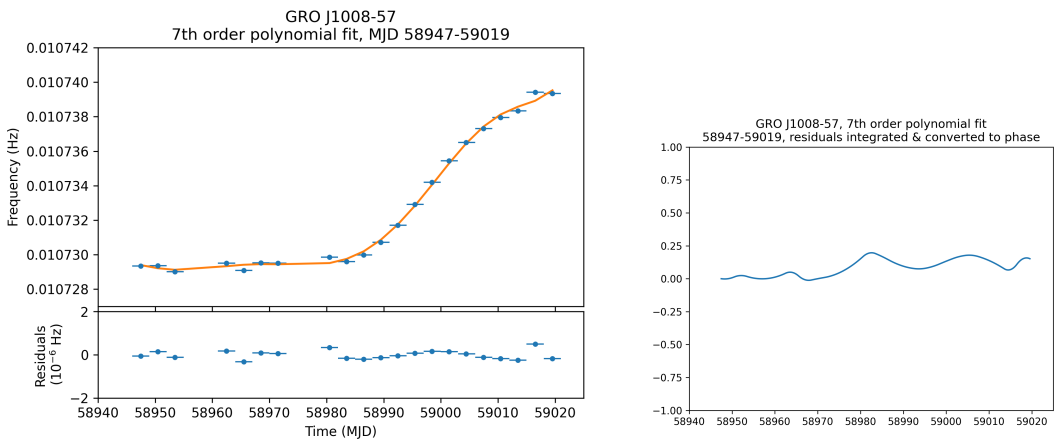
The initial aim of the timing analysis is to phase-connect the NICER/XTI observations to obtain precise spin frequencies. We start with creating a timing solution using the Fermi/GBM spin frequency measurements. The $\sim$80 day-long Fermi/GBM frequency history is fitted by a polynomial. It is determined that a seventh-order polynomial gives the best results. The frequency residuals are calculated by subtracting the

Table 6.1: Timing parameters of the timing model to fit Fermi/GBM frequencies of GRO J1008–57.

Timing range	MJD 58947–59019
Epoch	MJD 59000
ν	10.734 69$\pm$0.00012 mHz
dν/dt	(4.82$\pm$0.22) $\times$ 10^{-12} Hz s^{-1}
$d^2\nu/dt^2$	(-4.20$\pm$3.71) $\times$ 10^{-19} Hz s^{-2}
$d^3\nu/dt^3$	(-6.71$\pm$1.31) $\times$ 10^{-24} Hz s^{-3}
$d^4\nu/dt^4$	(-1.73$\pm$1.50) $\times$ 10^{-30} Hz s^{-4}
$d^5\nu/dt^5$	(1.85$\pm$0.60) $\times$ 10^{-35} Hz s^{-5}
$d^6\nu/dt^6$	(3.13$\pm$1.29) $\times$ 10^{-41} Hz s^{-6}
$d^7\nu/dt^7$	(1.73$\pm$0.90) $\times$ 10^{-47} Hz s^{-7}

timing model from the frequency history. Afterwards, the residuals are interpolated with a linear spline and the integration of the linear spline yields the phase residuals (Equation (4.1). The Fermi/GBM frequencies and the fitted model are matching enough so that the the phase difference resulting from the differences are within 0.25 cycles over $\sim$80 days (Figure 6.3). The parameters of the timing model are presented in Table 6.1.

Once a timing model is obtained, the NICER/XTI observations are folded to the respective frequencies the timing solution yields and pulse profiles with 32 phase bins are created. Each pulse profile is expressed in terms of Fourier harmonics and cross-correlated with a template profile (see Section 3.2.2). The template profile is chosen as the one with the highest overall χ^2 value among them. This way, pulse profiles are aligned and the pulse ToAs are acquired. The pulse ToAs can be fitted with a cubic function, $\Delta\phi = (1.10 \times 10^{-5})t^3 + 0.0122t^2 + 0.360t + 2.81$, where $\Delta\phi$ is the pulse ToA and t is the time, in terms of (MJD$-$59000). The fit and the resulting residuals of ToAs indicate that the ToAs are obtained correctly and the pulses are correctly phase-connected (Figure 6.4). In this case, the fit is used to verify the continuity of the ToAs and the correction of the phase-connection of pulses, and does not affect the rest of the analysis. Finally, applying linear fits to successive ToA triplets, the frequency



(a) (b)

Figure 6.3: (a) Top panel: Fermi/GBM pulse frequency history (light blue) and the timing model (orange). Bottom panel: Frequency residuals relative to the timing solution. (b) The phase residuals after integrating the linear spline of the frequency residuals.

corrections are calculated and NICER/XTI spin frequencies are generated. Frequency measurement uncertainties are derived from the 1σ errors of the fitted slopes, and the uncertainties in time correspond to the time intervals covered by each ToA triplet.

When superimposed with Fermi/GBM spin frequency history, some discrepancy between Fermi/GBM and NICER/XTI spin frequencies are evident (Figure 6.5). While the spin frequencies are matching at most of the times, the beginning of NICER/XTI frequencies are visibly lower than Fermi/GBM counterparts. Since the procedure of obtaining NICER/XTI frequencies are seemingly correct, we concluded the cause of discrepancy is that even though it is stated otherwise in the website, Fermi/GBM frequencies up to the end of the 2020 outburst are actually orbitally corrected (Figure 6.6). As the orbital determination of the source is outside of the scope of the thesis, the details are omitted here. Nevertheless, the orbit parameters of GRO J1008–57 in Kühnel et al. [133] give that the Doppler shifts on the spin frequency due to orbital motion are $\sim^{+1}_{-4}$ μHz in the given frequency range, in which the discrepancy is well-bounded. As a result, Fermi/GBM frequencies are not used along with measured NICER/XTI counterparts for the rest of the analysis; nonetheless, Fermi/GBM

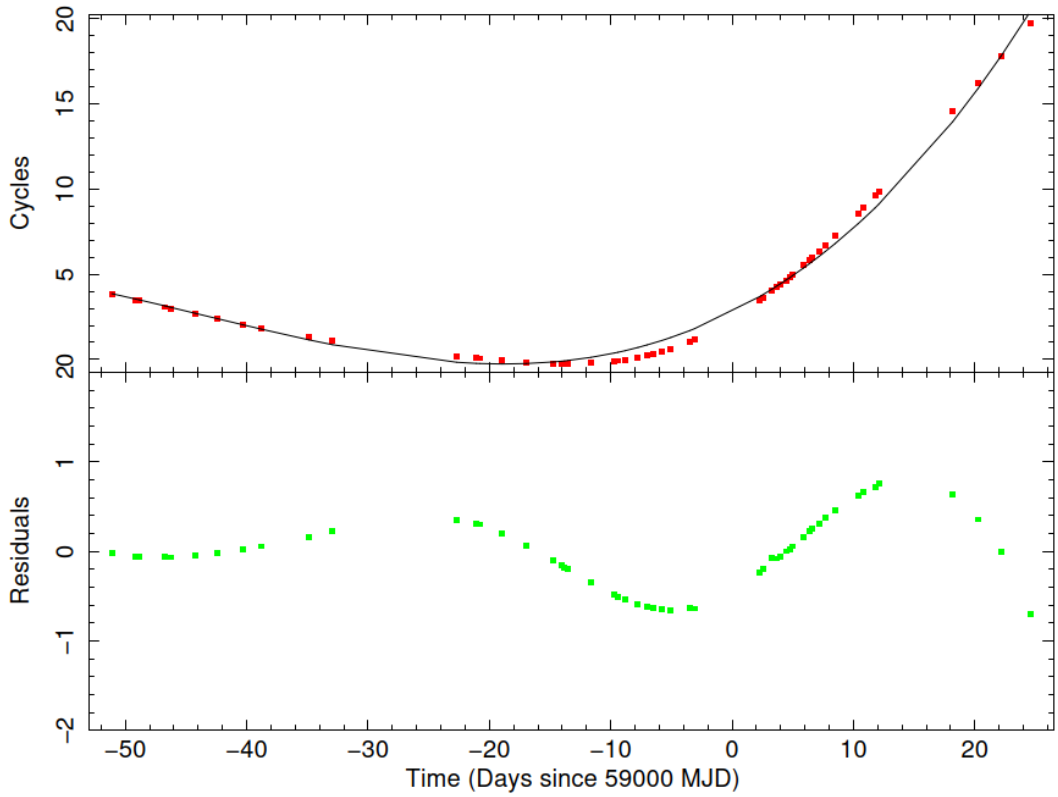


Figure 6.4: Upper panel: Time of arrivals (ToAs) of pulses from NICER/XTI observations of GRO J1008–57 (red), along with the cubic fit of ToAs (black line). Lower panel: ToA residuals (green).

frequencies are still useful to phase-connect the NICER/XTI observations.

Further orbital correction is not applied to NICER/XTI pulse profiles. The NICER/XTI frequencies are still in line with Fermi/GBM counterparts at most of the part, including the peak of the outburst. There is some difference at the beginning of the observations, less than 2 μHz, resulting a phase shift no more than ∼0.015 s per spin period ($P_{spin} \approx 93.2$ s). Since there are 32 phase bins in pulse profiles, in order to get one phase bin shift due to the orbital modulation, an observation should last at least for 18 ks in the worst case. Considering that the NICER/XTI observations at the beginning are not that long, the impact of the orbital modulation on the shape of the pulse profiles will be negligible.

The luminosity-sorted pulse profiles do not show any substantial evolution through almost 2 orders of magnitude of luminosity ($\sim 2 \times 10^{35}$ to $\sim 1.5 \times 10^{37}$ erg s^{-1}). The

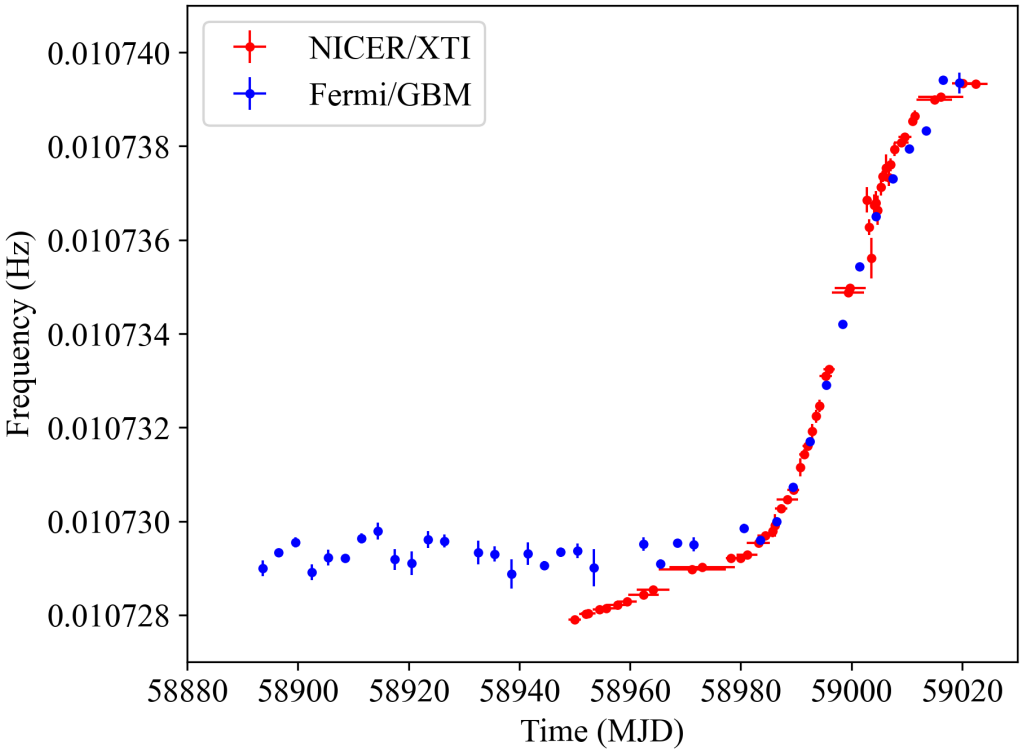


Figure 6.5: Spin frequency evolution of GRO J1008–57 by NICER/XTI (red) and Fermi/GBM (blue).

pulses are double-peaked: A more prominent peak is accompanied by a more prominent dip, along with a smaller peak and a smaller dip (Figure 6.7).

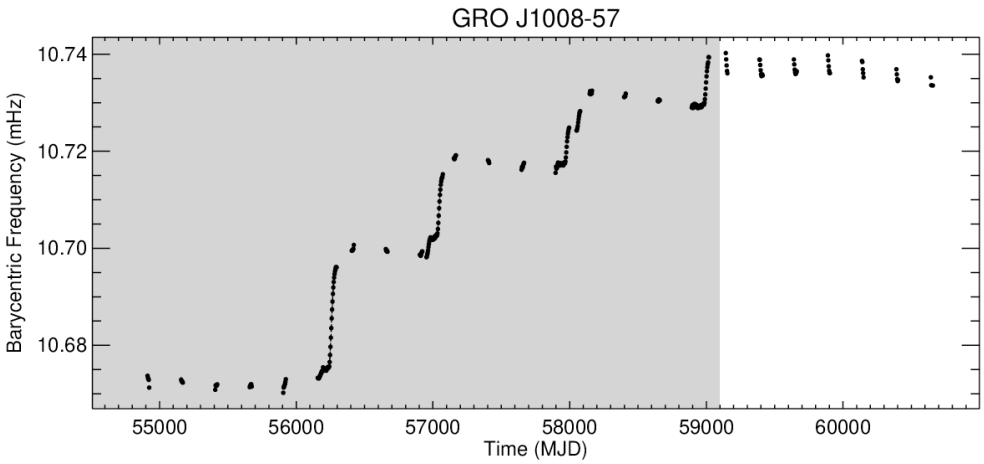
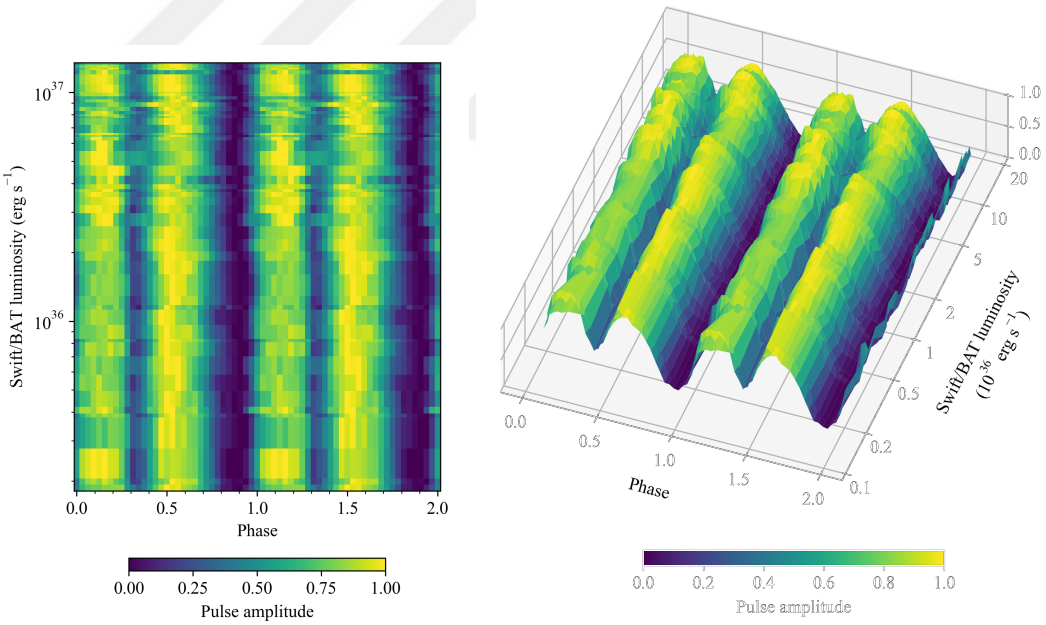


Figure 6.6: Fermi/GBM spin frequency history of GRO J1008–57. Orbitally corrected part is highlighted with gray. Note that the frequencies are changing much faster in the white region due to the orbital modulation, than the counterparts in the gray region, which are orbit-corrected. Adapted from the Fermi/GBM accreting pulsar histories archive.



(a) (b)

Figure 6.7: Luminosity-sorted pulse profiles of GRO J1008–57 in 2D (a) and 3D (b). Swift/BAT luminosities are in the 15–50 keV range. The pulse profiles are normalized to the [0, 1] range and plotted over two cycles for clarity.

CHAPTER 7

DISCUSSION

7.1 Swift J0243.6+6124

The NICER/XTI data set of 2017–2018 outburst of Swift J0243.6+6124 is analysed to enrich the spin frequency history with additional measurements. Apart from the one around MJD ∼58160, another reversal is observed around MJD ∼58510, initiating a new phase of spin-down behaviour in the source. Based on the corresponding luminosity levels, torque reversals tend to take place consistently below $\sim 7 \times 10^{36}$ erg s^{-1}. Given that prior observations confirm the presence of pulsations at luminosities as low as 10^{34}–10^{35} erg s^{-1} [79, 83], the observed spin-down phases are unlikely to be caused by the transition into the propeller phase.

A transition in the pulse profiles of Swift J0243.6+6124 is evident. The pulse profiles are single-peaked below the luminosity of $\sim 7 \times 10^{36}$ erg s^{-1}. With increasing luminosity, a secondary peak begins to form and gradually a double-0peaked profile emerges; and at the highest luminosities, the initial dominant peak starts to fade. The maximum luminosity in the analysed observations is $\sim 7 \times 10^{37}$ erg s^{-1}.

In fact, the change in the pulse profiles around 7×10^{36} erg s^{-1} is a previously unreported transition, predicted by the Becker model as L_{coul} (Equation (2.31)). Below this luminosity threshold, the emission from the accretion column is from purely pencil beam—hence the single-peaked pulses. This type of single-peaked profile was previously reported by Doroshenko et al. [83] near 3×10^{34} erg s^{-1} using NuSTAR data. Above this level, fan beam emission starts to appear alongside pencil beam emission, explaining the emergence of the second peak and indicating a hybrid regime that persists up to the second luminosity threshold L_{crit} predicted by the Becker model. If the

transition observed at $\sim 7 \times 10^{36}$ erg s^{-1} is indeed associated with L_{coul}, then adopting typical pulsar parameters implies a magnetic field of 4.7×10^{12} G.

At the upper end of the luminosity range, one component of the double-peaked pulse profile starts to weaken with increasing luminosity, but it is uncertain whether this marks another transition. The observations of which the pulse profiles are created (MJD $\sim$58300–58530) does not have a luminosity higher than 7×10^{37} erg s^{-1}. Yet, the critical luminosity threshold L_{crit} signifying a change from subcritical to super-critical accretion is actually expected around this upper limit, and it can explain the weakening of the second peak. Pulse profiles in the beginning of the outburst (MJD $\sim$58030–58160), where the luminosity reaches 1×10^{39} erg s^{-1} level are presented by [83]: They observed a transition in pulse profiles at 8.8×10^{37} erg s^{-1} (corrected for a 5.2 kpc distance), above which the pulses are single-peaked. Similarly, using the quasi-periodic oscillation (QPO)-like features in power spectra of the source at the same time segment, Wilson-Hodge et al. [81] estimated the critical luminosity as 1.0×10^{38} erg s^{-1} (again, corrected for a 5.2 kpc distance). These increase the odds that the the upper end of the luminosity-sorted pulse profiles are just below the critical luminosity L_{crit}. Borrowing the critical luminosity estimate of [83], the corresponding magnetic field strength is found as 5.3×10^{12} G.

Therefore, we were able to confine the magnetic field estimate of Swift J0243.6+6124 to 4.7–5.3 $\times 10^{12}$ G using the transitional levels of the source and assuming a 5.2 kpc distance. While the CRSF energies in the X-ray spectra suggests a much higher value of $\sim 1.6 \times 10^{13}$ G, as noted in Section 4.1, this value may reflect the presence of local multipole magnetic fields. The results of the timing noise analysis from our published article support this interpretation [1]; though that analysis is not included here as it lies beyond the scope of this thesis.

In summary,

- A new transition in the pulse profiles is found at $\sim 7 \times 10^{36}$ erg s^{-1}, which matches L_{coul} in the Becker model. The observed changes in the pulse profiles are also consistent with the model's prediction of the change in emission geometry.

- At the highest luminosities, another change in pulse profiles begins to emerge,

and it is likely that L_{crit} in the Becker model lies just above the maximum luminosity covered by the pulse profiles.

- The magnetic field strength estimates using L_{coul} and L_{crit} at a 5.2±0.3 kpc distance converges at $\sim 5 \times 10^{12}$ G. Therefore, we were able to bound it in the range of 4.7–5.3 $\times 10^{12}$ G.

7.2 MXB 0656–072

To investigate timing properties of MXB 0656–072, the RXTE/PCA data from the source's 2007–2008 outburst are analysed. To this end, precise spin frequency measurements are performed, luminosity-sorted pulse profiles are created, and the intrinsic frequency evolution is tracked by modelling the torque–luminosity relation of the source. The phase-connection of the RXTE observations helped us obtain frequency measurements all across the outburst sequence (∼350 d), highly enriching 6 publicly available data points from Fermi/GBM, which covers only ∼20 days from this time period.

Created pulse profiles, in the luminosity range of $\sim 6 \times 10^{34}$–2.4×10^{37} erg s^{-1} at a 5.7 kpc distance, mostly exhibit a single-peak structure (Figure 5.1). The source luminosity suggests that the source stays in the subcritical accretion phase with a pencil beam emission throughout the outburst sequence. The pulses disappear into noise below $\sim 5 \times 10^{35}$ erg s^{-1} as a result of the increased signal-to-noise ratio due to sparse count rates on the detector. No transition in pulse profiles is observed: The estimated critical luminosity transition (L_{crit}) lies beyond the luminosity range of the pulse profiles (as discussed in the following paragraphs), and is therefore not expected to be observed in the data. However, the other transition in the subcritical accretion regime L_{coul}, above which the emission shifts from a pure pencil beam to a hybrid fan–pencil beam geometry, is predicted to occur at $\sim 8 \times 10^{36}$ erg s^{-1} for a magnetic field of 3.3–3.7 $\times 10^{12}$ G according to Equation (2.31). In order to reconcile the discrepancy, rather than utilizing typical pulsar parameters, the required pulsar mass and radius values are checked. The condition $L_{coul} > 2.4 \times 10^{37}$ erg s^{-1} holds

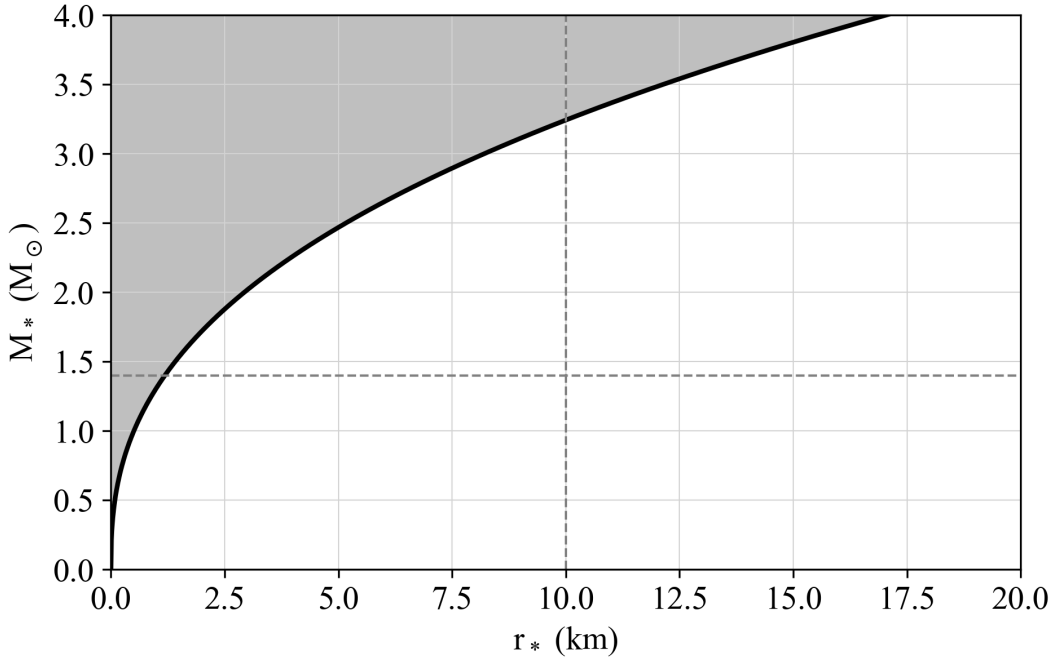


Figure 7.1: The parameter space of solution of Equation (7.1). Typical pulsar parameters are marked with dashed lines, and the solution space is highlighted with gray.

when

$$\frac{M_*^{11/8}}{r_*^{13/24}} > 1.45, \tag{7.1}$$

where the unit of r_* is km and the unit of M_* is solar mass. However, the values holding this relation are not physical (Figure 7.1), so it is not found to be a plausible approach. The implications of this missing transition, from a hybrid fan–pencil beam to a pure pencil beam with decreasing luminosity, is further discussed in the final section of this chapter.

On the other hand, modelling the intrinsic frequency evolution with the Ghosh & Lamb model is highly successful. Ghosh & Lamb model is one of the oldest torque models in the literature. It is simple yet powerful among the other torque models; and as argued in Section 5.3.1, the predictions of various torque models converge because of the slow rotation of the source combined with relatively high observed luminosities. The fitting is in line with the frequency evolution, and the spin frequency residuals are constrained to only ± 0.8 µHz. The best fit of model $\dot{\nu} = \beta L_{37}^{6/7}$ yields β = 2.42(6); in turn, applying Equation (3.15), assuming typical pulsar parameters and

the slow rotator approximation ($n(\omega_s) \approx 1.4$) results in a magnetic field strength of 4.2×10^{12} G. This value is close to the estimates $B = 3.4$–3.7×10^{12} G inferred by the observed CRSF lines at 30–36 keV [114, 113, 120, 122].

Nespoli et al. [122] had observed an anti-correlation between the source luminosity and the photon index in X-ray spectra, leading to a conclusion that a transition occurs at $\sim 2.3 \times 10^{37}$ erg s^{-1} for a distance of 3.9 kpc. Adjusting to the more recent distance estimate of 5.7 kpc, this transition luminosity occurs at $\sim 4.9 \times 10^{37}$ erg s^{-1}. The reported anti-correlation is in line with what is expected at the transition between subcritical and supercritical accretion regimes; therefore, this transition luminosity can be interpreted as L_{crit}. Note that a transition at L_{crit} is not directly observed in the pulse profiles since the 2007–2008 outbursts did not reach such a luminosity level–only the type II outburst in 2003 did. Still, the previously observed transition remains valuable for constraining the source's distance and magnetic field strength. Using Equation (2.30) and the previous magnetic field estimates from CRSF lines, L_{crit} is expected to lie at ~ 5.1–5.5×10^{37} erg s^{-1}, which is quite close to the value mentioned above.

Although there are many cases where the magnetic field strengths predicted by torque models do not match well with those calculated from CRSF observations [147, 42], the magnetic field strength predictions of MXB 0656–072 converge. To constrain the parameters, the dependence of the magnetic field strength on the source distance is plotted, using the predictions from the Ghosh & Lamb torque model, and L_{crit} of the Becker model (Figure 7.2). The results from both models converge within the confidence region of the Gaia EDR3 distance estimate and the magnetic field estimate from the CRSF energies.

Revisiting the frequency residuals derived from the Ghosh & Lamb torque model, the residuals covering $\sim$350 days resemble an orbital signature and the modulation is similar to the previously predicted orbital period of 101.2 d [120]. Nevertheless, attempts to fit an orbit to the data set is inconclusive.

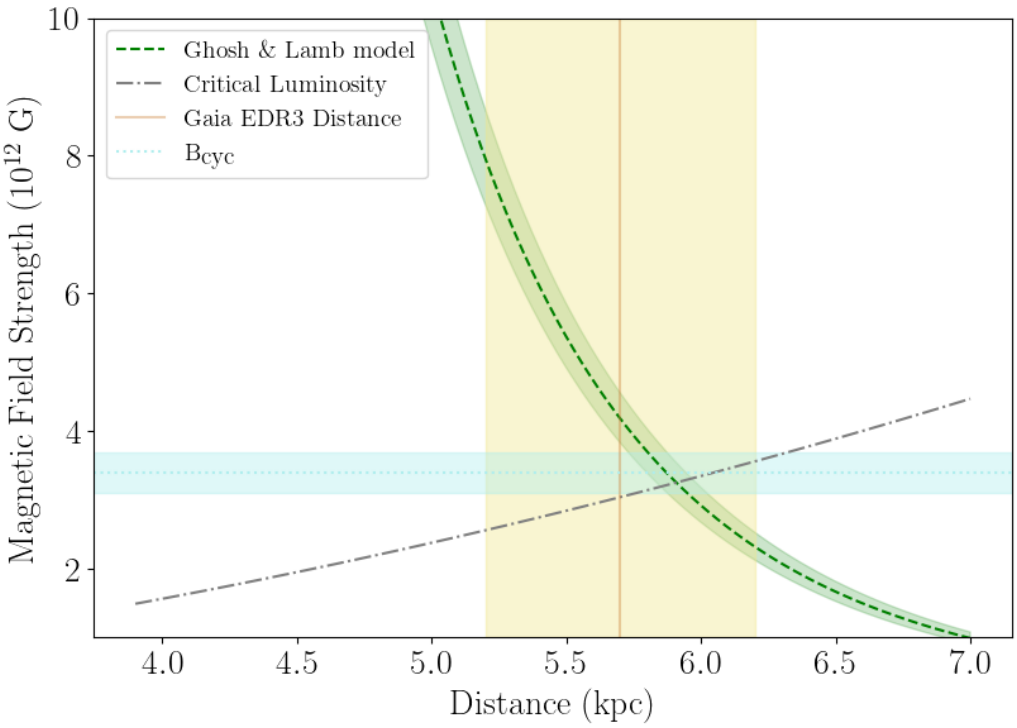


Figure 7.2: Variation of the magnetic field strength of MXB 0656–072 with distance, derived from several models. Uncertainties in the parameters are shown as shaded areas.

7.3 GRO J1008–57

For this thesis, NICER/XTI observations of GRO J1008–57 during its Type II outburst in 2020 are analysed. Phase-connecting the NICER data helped us measure precise measurements of the spin frequencies throughout the outburst. It is revealed that the obtained spin frequencies do not match with the frequency history from Fermi/GBM, especially at the beginning of the outburst, due to the revelation that Fermi/GBM frequencies throughout the outburst is actually corrected with the pulsar orbit. Yet, the most current orbital solution [133] is reported to be not completely coherent well beyond its epoch [70], ultimately only NICER frequencies are utilised for the rest of the analysis. Nevertheless, the modulation in the NICER spin frequencies due the the orbit is miniscule and its effect on the pulse profiles are negligible. Work on an updated orbit solution of GRO J1008–57 is in progress, but the details are not included

CRSF energy (keV)	B (G)	L_{crit} (erg s^{-1})	L_{coul} (erg s^{-1})	L_{crit}/L_{coul}
75	6.5×10^{12}	1.1×10^{38}	6.3×10^{36}	17
90	7.8×10^{12}	1.3×10^{38}	5.9×10^{36}	22

Table 7.1: Estimated magnetic field strength and corresponding transition luminosities of GRO J1008–57, based on the given CRSF energies and typical pulsar parameters.

here as the orbit determination is outside of the main objectives of this thesis.

The pulse profiles of GRO J1008–57 consistently exhibit a double-peaked structure throughout the outburst and do not show a discernible evolution with changing luminosity (Figure 6.7). This result is puzzling, as the Becker model predicts at least one transition, if not two, in the pulse profiles at this luminosity range.

Assuming typical pulsar parameters, e.g., $M_* = M_{1.4} = 1.4\ M_\odot$, $r_* = r_6 = 10$ km, the transition luminosities derived in Becker model are simplified as follows:

$$L_{crit} \approx 1.49 \times 10^{37}\ \text{erg s}^{-1} \left(\frac{B_*}{B_{12}}\right)^{16/15},\ L_{Coul} \approx 1.17 \times 10^{37}\ \text{erg s}^{-1} \left(\frac{B_*}{B_{12}}\right)^{-1/3}. \tag{7.2}$$

Then, the ratio of the transition luminosities are found as

$$\frac{L_{crit}}{L_{coul}} \approx 1.27 \left(\frac{B_*}{B_{12}}\right)^{7/5}. \tag{7.3}$$

As both transition luminosities and their ratio depend on the magnetic field strength, obtaining a consistent estimate of the source's magnetic field is crucial. Since CRSF line energies in the X-ray spectrum provide a distance-independent estimate, they are commonly used to constrain the magnetic field strength of sources. For GRO J1008–57, several cyclotron features are identified (see Section 6.1) and the reported CRSF energies lie between 76–90 keV, $\sim$90.3 keV being the most recent detection. Using Equation (2.27), the magnetic field strength and corresponding transition luminosity estimates, along with the ratio between them based on 75 and 90 keV CRSF energies are provided in Table 7.1. Again, these values are calculated using typical pulsar parameters.

Meanwhile, the source flux varied by a factor of $\sim$75 over the course of the observa-

tions, corresponding to a $\sim 1.8 \times 10^{35}$–1.35×10^{37} erg s^{-1} luminosity range assuming a 3.6±0.2 kpc distance from the Gaia EDR3 catalogue. Based on the estimates in Table 7.1, we don't expect to see the critical luminosity threshold L_{crit} above which the hybrid emission is effectively changed into a full fan beam emission, as the constructed pulse profiles do not reach luminosities on the order of 10^{38} erg s^{-1}. Besides, the existence of a double-peaked structure at the higher luminosities (Figure 6.7) is compatible with the hybrid fan–pencil beam mode, supporting the prediction that L_{crit} is indeed beyond the maximum luminosity of the observations.

Another transition between hybrid and full pencil beam emission is expected to be at $L_{coul} \sim 6 \times 10^{36}$ erg s^{-1}, where the pencil beam manifests as single-peaked pulse profiles. However, such a transition is not observed in the pulse profiles. Even if the distance estimate is significantly inaccurate, the flux variation still offers insight into whether a transition in pulse profiles is expected. But the magnitude of observed flux variability, a factor of 75, makes it implausible that both transition luminosities fall entirely outside the sampled range.

In order to reconcile the case, several possibilities are examined. One approach involved estimating the required magnetic field strength. For typical pulsar parameters, the condition $L_{crit}/L_{coul} > 75$ holds only if $B_* > 1.8 \times 10^{13}$ G—an implausibly high value compared to similar sources. Also, this estimate is more than twice the magnetic field inferred from the CRSF energy, and even accounting for gravitational redshift at the neutron star surface, it would imply an implausible value of $z > 1.3$.

Another approach comprises checking if changing the mass and radius of the neutron star gives an expected result. With mass and radius of the pulsar is not fixed to typical values, Equation (7.3) changes into the form of

$$\frac{L_{crit}}{L_{coul}} = 1.27 \left(\frac{M_*}{M_{1.4}}\right)^{-49/120} \left(\frac{r_*}{r_6}\right)^{77/120} \left(\frac{B_*}{B_{12}}\right)^{7/5}, \tag{7.4}$$

where $B_{12} = 10^{12}$ G. Fixing the magnetic field strength at $B_* = 8 \times 10^{12}$ G, $L_{crit}/L_{coul} > 75$ holds when

$$\frac{r_*^{77/120}}{M_*^{49/120}} > 12.3 \tag{7.5}$$

where the unit of r_* is km and the unit of M_* is solar mass. Using this relation, the plausible mass and radius values are plotted in Figure 7.3. Unfortunately, the

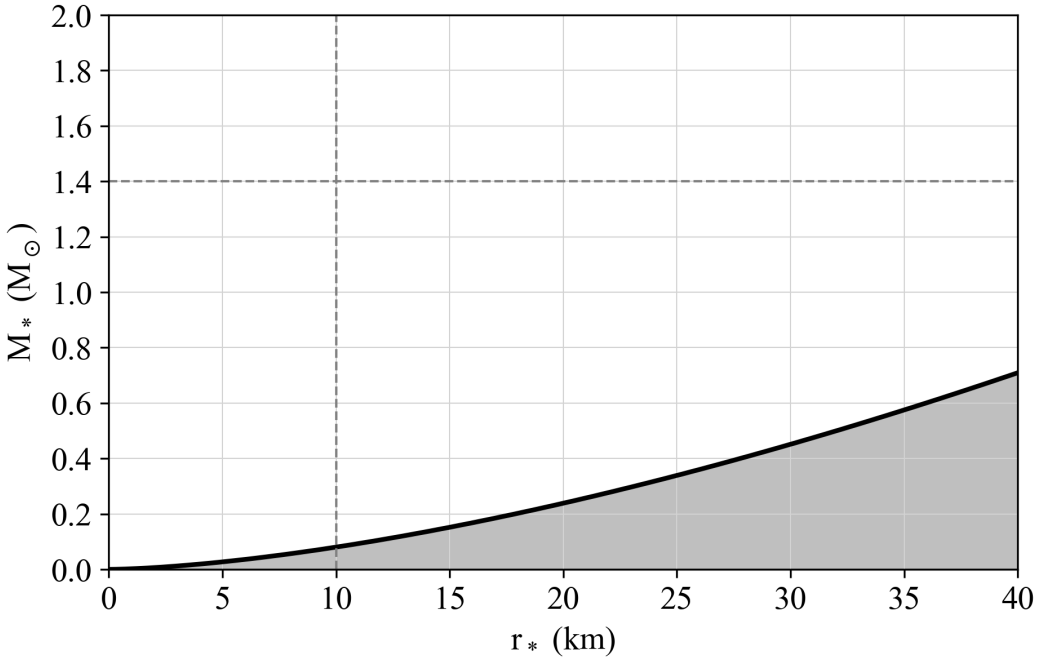


Figure 7.3: The parameter space of solution of Equation (7.5). Typical pulsar parameters are marked with dashed lines, and the solution space is highlighted with gray.

resulting solution space lies far from typical pulsar parameters and appears physically implausible. Therefore, we conclude that the absence of any observable transition in the pulse profiles of GRO J1008–57 is not compatible with the Becker model.

CHAPTER 8

CONCLUSION

The model described in Becker et al. [40] is successful in predicting the pulse profile transitions of Swift J0243.6+6124 and provides a solid framework for understanding the accretion column dynamics of the source. Besides, despite its estimate of the critical luminosity transition (L_{crit}) for MXB 0656–072 lies outside the luminosity range of the observations used, it was strongly suggested that this transition occurred during the 2003 outburst of the source; consequently, utilizing L_{crit} in combination with other models helped verify that the estimations of magnetic field strength and distance of the source are consistent. However, there is no transition in pulse profiles in GRO J1008–57 at the expected L_{coul} level, and the expected L_{crit} is an order of magnitude greater than maximum luminosity of the observation used.

The findings of the individual sources presented in the previous chapters are summarized in Table 8.1.

Even though it is clearly observed in Swift J0243.6+6124 at the predicted luminosity level, the absence of the detection of L_{coul} in MXB 0656–072 and GRO J1008–57 can be regarded as a caveat of the Becker model. The Becker model begins with an assumption that the accretion column is cylindrical. Then, at the upper levels of subcritical accretion ($L_{crit} > L_X > L_{coul}$), it predicts a subcritical emission zone in the accretion column, where the emission escape radially through the column walls as a fan beam pattern, while some of the radiation still escapes from the top as a pencil beam, resulting in a hybrid emission geometry. At the lower levels of subcritical accretion, i.e., below L_{coul}, the emission primarily escapes from the top and a pencil beam is observed. Although these assumptions successfully explain observations in several sources, including Swift J0243.6+6124, this simplification might not work

Table 8.1: Summary of the key findings about the sources. The table lists the luminosity ranges used in the analysis, the expected values of L_{coul} and L_{crit} from the Becker model (and whether these transitions are observed if the corresponding luminosity levels are reached), the expected L_{Edd} (if applicable), and magnetic field strength estimates along with previous estimates from existing literature. Where results are taken from other publications, the corresponding references are provided. All luminosity values are expressed in units of 10^{36} erg s^{-1}.

	Swift J0243.6+6124	MXB 0656–072	GRO J1008–57
L range	∼1.4–70	∼0.06–24	∼0.18–14
L_{coul}	∼7	∼8	∼6
Observed?	Yes	No	No
L_{crit}	∼88	∼51–55	∼110–130
Observed?	Yes [83]	At ∼49 [122]	–
L_{Edd}	∼260	–	–
Observed?	Yes [83]	–	–
B (G)	$\sim 4.7–5.3 \times 10^{12}$	$\sim 4.2 \times 10^{12}$	–
In literature	$\sim 3–9 \times 10^{12}$	$3.3–3.7 \times 10^{12}$	$7–8 \times 10^{12}$
	[83]	[113, 120]	[135, 137]

for MXB 0656–072 and GRO J1008–57. Swift J0243.6+6124, as a galactic ULX, is capable of much higher luminosity, accretion level, and magnetic field strength near the pulsar surface, whereas—as far as the observations indicate—MXB 0656–072 and GRO J1008–57 are not. In subcritical accretion levels, it may be possible that the geometry of accreted matter at the magnetic poles of MXB 0656–072 and GRO J1008–57 is not cylindrical; as mentioned in Section 2.3.1, alternative models with different assumptions exist.

When Mushtukov [45] model is considered instead, the overall prescription still seems puzzling. For example, for GRO J1008–57 the critical luminosity threshold can be calculated as $L_{crit} \sim 2 \times 10^{37}$ erg s^{-1} which is still above the luminosity range of this thesis study and the model does not anticipate any other transition at lower luminosity (e.g. it predicts no transition like the Coulomb transition luminosity of the

Becker model, which is already observed in Swift J0243.6+6124). Thus, we cannot test its validity on GRO J1008–57. Besides, it is not possible to explain the simultaneous presence of several distinct transitional levels (L_{coul}, L_{crit} and L_{Edd}) observed in Swift J0243.6+6124 using the Mushtukov model. Nevertheless, the need for a numerical solution for L_{crit}, even after simplifications, makes the model difficult to quantify using observational data.

Although no clear analytical prescription exists yet, the accretion mound model presents a promising alternative model for describing the geometry of the accretion column. There are ongoing efforts to the structure and physical conditions of accretion mounds using 2D and 3D magnetohydrodynamic simulations [51, 55, 148].

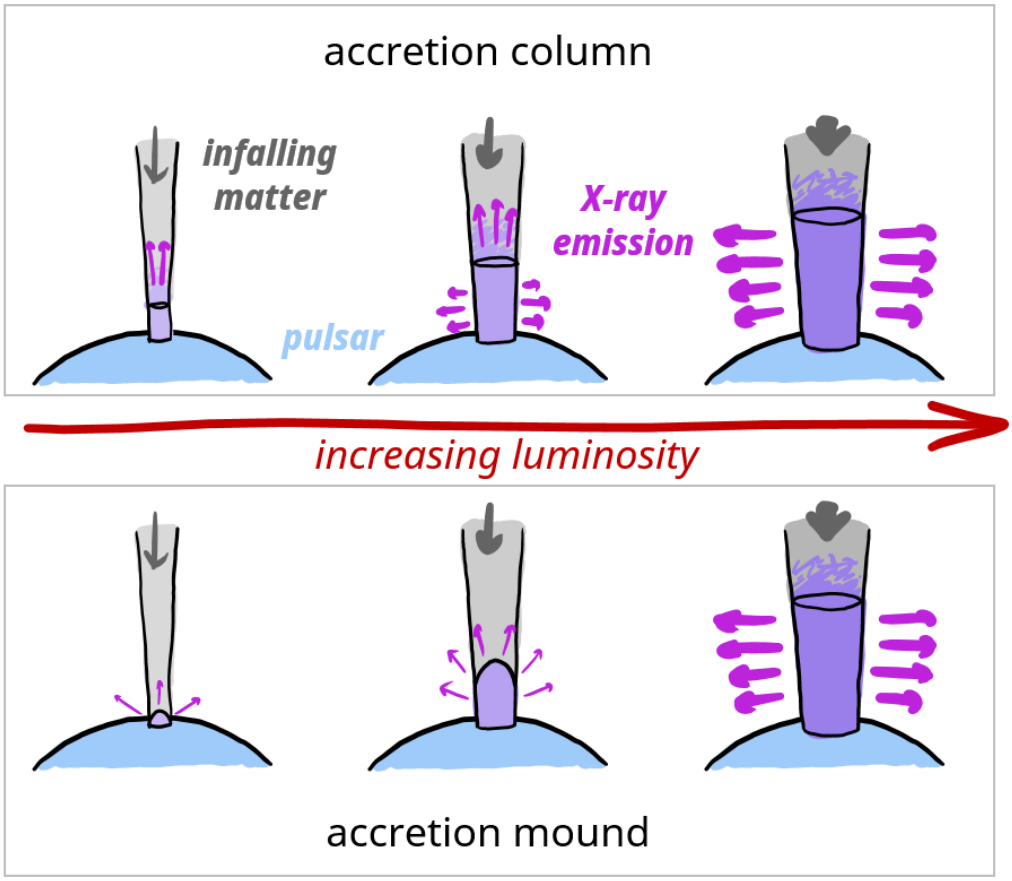


Figure 8.1: The changes in accretion column and accretion mound geometries with increasing luminosity. At the highest luminosities, it is possible that accretion mound geometry is well-approximated to a cylindrical accretion column.

From an observational perspective, the results seems to be consistent with several sources like such as 4U 0115+63, Vela X–1, and GX 301–2 [53], because this model also handles the CSRFs imprinted at different angles with respect to the observer.

To conclude, despite being a promising model for Swift J0243.6+6124, the Becker model does not provide a coherent picture for MXB 0656–072 and GRO J1008–57. It is possible that the actual physical conditions reside in an hybrid or superposition of these models. To be more precise, if we assume an *accretion mound* model at lower luminosities (see Section 2.3.3), which grows into a rather cylindrical shape with increasing mass accretion rate, then a combination with the Becker model may be applicable. For instance, a smaller accretion mound may form in MXB 0656–072 and GRO J1008–57, then the emission is expected to be in rather spherically diverging (see Figure 8.1) and its exact characteristics depend on the structure of the mound. Thus, at low luminosities, the pulse profile morphology depends on the viewing angle of the observer and is typically expected to exhibit a single-peaked profile (or double-peaked if the secondary cap is visible along the line of sight). The profile morphology can be interpreted as a pencil beam form, even though the emission in practice diverges radially over the mound. Whether the changes associated with the luminosity L_{coul} are observable in the pulse profile depends on the local interaction depth along the observer's line of sight. At higher luminosities, increased mass accretion rate may transform the accretion mound into a cylindrical accretion column due to the confinement by the magnetic field lines, approximating the results to those of the Becker model.

REFERENCES

[1] M. M. Serim, Ç. K. Dönmez, D. Serim, L. Ducci, A. Baykal, and A. Santangelo, "Timing analysis of Swift J0243.6+6124 with NICER and Fermi/GBM during the decay phase of the 2017-2018 outburst," *Monthly Notices of the Royal Astronomical Society*, vol. 522, pp. 6115–6122, July 2023.

[2] M. M. Serim, D. Serim, Ç. K. Dönmez, Y. Tuo, L. Ducci, A. Baykal, and A. Santangelo, "Pulse frequency variations and timing noise of MXB 0656–072 during the 2007–2008 type I outbursts and implications for its magnetic field," *Astronomy and Astrophysics*, vol. 690, p. A5, Oct. 2024.

[3] T. M. Tauris, M. Kramer, P. C. C. Freire, N. Wex, H. T. Janka, N. Langer, P. Podsiadlowski, E. Bozzo, S. Chaty, M. U. Kruckow, E. P. J. van den Heuvel, J. Antoniadis, R. P. Breton, and D. J. Champion, "Formation of Double Neutron Star Systems," *The Astrophysical Journal*, vol. 846, p. 170, Sept. 2017.

[4] F. Verbunt and C. Zwaan, "Magnetic braking in low-mass X-ray binaries.," *Astronomy and Astrophysics*, vol. 100, pp. L7–L9, July 1981.

[5] T. M. Tauris and E. P. J. van den Heuvel, "Formation and evolution of compact stellar X-ray sources," in *Compact stellar X-ray sources* (W. H. G. Lewin and M. van der Klis, eds.), vol. 39 of *Cambridge Astrophysics*, pp. 623–665, Cambridge University Press, 2006.

[6] D. R. Lorimer and M. Kramer, *Handbook of Pulsar Astronomy*, vol. 4. 2004.

[7] S. L. Shapiro and S. A. Teukolsky, *Black holes, white dwarfs and neutron stars. The physics of compact objects*. John Wiley & Sons, Ltd, 1983.

[8] W. H. G. Lewin, J. van Paradijs, and E. P. J. van den Heuvel, *X-ray Binaries*. Cambridge University Press, 1997.

[9] D. Bhattacharya and E. P. J. van den Heuvel, "Formation and evolution of

binary and millisecond radio pulsars," *Physics Reports*, vol. 203, pp. 1–124, Jan. 1991.

[10] P. Reig, "Be/X-ray binaries," *Astrophysics and Space Science*, vol. 332, pp. 1–29, Mar. 2011.

[11] R. W. Hanuschik, "On the structure of Be star disks.," *Astronomy and Astrophysics*, vol. 308, pp. 170–179, Apr. 1996.

[12] J. E. Bjorkman and J. P. Cassinelli, "Equatorial Disk Formation around Rotating Stars Due to Ram Pressure Confinement by the Stellar Wind," *The Astrophysical Journal*, vol. 409, p. 429, May 1993.

[13] S. P. Owocki, S. R. Cranmer, and K. G. Gayley, "Inhibition FO Wind Compressed Disk Formation by Nonradial Line-Forces in Rotating Hot-Star Winds," *The Astrophysical Journal Letters*, vol. 472, p. L115, Dec. 1996.

[14] J. M. Porter, "Continuum IR emission of Be star wind-compressed discs.," *Astronomy and Astrophysics*, vol. 324, pp. 597–605, Aug. 1997.

[15] J. C. Brown, J. P. Cassinelli, and M. Maheswaran, "Magnetically Fed Hot Star Keplerian Disks with Slow Outflow," *The Astrophysical Journal*, vol. 688, pp. 1320–1325, Dec. 2008.

[16] S. R. Cranmer, "A Pulsational Mechanism for Producing Keplerian Disks Around Be Stars," *The Astrophysical Journal*, vol. 701, pp. 396–413, Aug. 2009.

[17] J. M. Porter and T. Rivinius, "Classical Be Stars," *Publications of the Astronomical Society of the Pacific*, vol. 115, pp. 1153–1170, Oct. 2003.

[18] M. Orellana and G. E. Romero, "Gamma-Ray Emission from Be/X-ray Binaries," *Astrophysics and Space Science*, vol. 297, pp. 167–178, June 2005.

[19] P. Reig, J. Fabregat, and J. Alfonso-Garzón, "Optical counterpart to Swift J0243.6+6124," *Astronomy and Astrophysics*, vol. 640, p. A35, Aug. 2020.

[20] P. Reig, V. Larionov, I. Negueruela, A. A. Arkharov, and N. A. Kudryavtseva, "The Be/X-ray transient 4U 0115+63/V635 Cassiopeiae. III. Quasi-cyclic variability," *Astronomy and Astrophysics*, vol. 462, pp. 1081–1089, Feb. 2007.

[21] J. E. Pringle, "Accretion discs in astrophysics," *Annual Review of Astronomy and Astrophysics*, vol. 19, pp. 137–162, Jan. 1981.

[22] R. H. D. Corbet, "The three types of high-mass X-ray pulsator.," *Monthly Notices of the Royal Astronomical Society*, vol. 220, pp. 1047–1056, June 1986.

[23] F. Fortin, F. García, A. Simaz Bunzel, and S. Chaty, "A catalogue of high-mass X-ray binaries in the Galaxy: from the INTEGRAL to the Gaia era," *Astronomy and Astrophysics*, vol. 671, p. A149, Mar. 2023.

[24] K. Davidson and J. P. Ostriker, "Neutron-Star Accretion in a Stellar Wind: Model for a Pulsed X-Ray Source," *The Astrophysical Journal*, vol. 179, pp. 585–598, Jan. 1973.

[25] H. J. G. L. M. Lamers and J. P. Cassinelli, *Introduction to Stellar Winds*. Cambridge University Press, 1999.

[26] R. Walter, A. A. Lutovinov, E. Bozzo, and S. S. Tsygankov, "High-mass X-ray binaries in the Milky Way. A closer look with INTEGRAL," *The Astronomy and Astrophysics Review*, vol. 23, p. 2, Aug. 2015.

[27] T. M. Tauris and E. P. J. van den Heuvel, *Physics of Binary Star Evolution. From Stars to X-ray Binaries and Gravitational Wave Sources*. 2023.

[28] A. Slettebak, "The Be Stars," *Publications of the Astronomical Society of the Pacific*, vol. 100, p. 770, July 1988.

[29] L. Bildsten, D. Chakrabarty, J. Chiu, M. H. Finger, D. T. Koh, R. W. Nelson, T. A. Prince, B. C. Rubin, D. M. Scott, M. Stollberg, B. A. Vaughan, C. A. Wilson, and R. B. Wilson, "Observations of Accreting Pulsars," *The Astrophysical Journal Supplement Series*, vol. 113, pp. 367–408, Dec. 1997.

[30] H. Bondi and F. Hoyle, "On the mechanism of accretion by stars," *Monthly Notices of the Royal Astronomical Society*, vol. 104, p. 273, Jan. 1944.

[31] J. Frank, A. King, and D. J. Raine, *Accretion Power in Astrophysics: Third Edition*. Cambridge University Press, 3 ed., 2002.

[32] L. Stella, N. E. White, and R. Rosner, "Intermittent Stellar Wind Acceleration and the Long-Term Activity of Population I Binary Systems Containing an X-Ray Pulsar," *The Astrophysical Journal*, vol. 308, p. 669, Sept. 1986.

[33] A. F. Illarionov and R. A. Sunyaev, "Why the Number of Galactic X-ray Stars Is so Small?," *Astronomy and Astrophysics*, vol. 39, p. 185, Feb. 1975.

[34] N. Shakura, K. Postnov, A. Kochetkova, and L. Hjalmarsdotter, "Theory of quasi-spherical accretion in X-ray pulsars," *Monthly Notices of the Royal Astronomical Society*, vol. 420, pp. 216–236, Feb. 2012.

[35] N. I. Shakura, K. A. Postnov, A. Y. Kochetkova, and L. Hjalmarsdotter, "Quasispherical subsonic accretion in X-ray pulsars," *Physics Uspekhi*, vol. 56, pp. 321–346, Apr. 2013.

[36] R. V. E. Lovelace, M. M. Romanova, and G. S. Bisnovatyi-Kogan, "Spin-up/spin-down of magnetized stars with accretion discs and outflows," *Monthly Notices of the Royal Astronomical Society*, vol. 275, pp. 244–254, July 1995.

[37] P. Ghosh and F. K. Lamb, "Accretion by rotating magnetic neutron stars. III. Accretion torques and period changes in pulsating X-ray sources.," *The Astrophysical Journal*, vol. 234, pp. 296–316, Nov. 1979.

[38] N. I. Shakura and R. A. Sunyaev, "Black holes in binary systems. Observational appearance.," *Astronomy and Astrophysics*, vol. 24, pp. 337–355, Jan. 1973.

[39] W. Kluźniak and S. Rappaport, "Magnetically Torqued Thin Accretion Disks," *The Astrophysical Journal*, vol. 671, pp. 1990–2005, Dec. 2007.

[40] P. A. Becker, D. Klochkov, G. Schönherr, O. Nishimura, C. Ferrigno, I. Caballero, P. Kretschmar, M. T. Wolff, J. Wilms, and R. Staubert, "Spectral formation in accreting X-ray pulsars: bimodal variation of the cyclotron energy with luminosity," *Astronomy and Astrophysics*, vol. 544, p. A123, Aug. 2012.

[41] J. Liu, P. A. Jenke, L. Ji, S.-N. Zhang, S. Zhang, M. Ge, J. Liao, X. Li, and L. Song, "Super-Eddington accretion of the first Galactic ultra-luminous X-ray pulsar Swift J0243.6+6124," *Monthly Notices of the Royal Astronomical Society*, vol. 512, pp. 5686–5692, June 2022.

[42] R. Staubert, J. Trümper, E. Kendziorra, D. Klochkov, K. Postnov, P. Kretschmar, K. Pottschmidt, F. Haberl, R. E. Rothschild, A. Santangelo, J. Wilms, I. Kreykenbohm, and F. Fürst, "Cyclotron lines in highly magnetized neutron stars," *Astronomy and Astrophysics*, vol. 622, p. A61, Feb. 2019.

[43] F. K. Lamb, C. J. Pethick, and D. Pines, "A Model for Compact X-Ray Sources: Accretion by Rotating Magnetic Stars," *The Astrophysical Journal*, vol. 184, pp. 271–290, Aug. 1973.

[44] P. Reig and E. Nespoli, "Patterns of variability in Be/X-ray pulsars during giant outbursts," *Astronomy and Astrophysics*, vol. 551, p. A1, Mar. 2013.

[45] A. A. Mushtukov, V. F. Suleimanov, S. S. Tsygankov, and J. Poutanen, "The critical accretion luminosity for magnetized neutron stars," *Monthly Notices of the Royal Astronomical Society*, vol. 447, pp. 1847–1856, Feb. 2015.

[46] D. Lai, "Theory of Disk Accretion onto Magnetic Stars," in *European Physical Journal Web of Conferences*, vol. 64 of *European Physical Journal Web of Conferences*, p. 01001, EDP, Jan. 2014.

[47] M. M. Basko and R. A. Sunyaev, "The limiting luminosity of accreting neutron stars with magnetic fields.," *Monthly Notices of the Royal Astronomical Society*, vol. 175, pp. 395–417, May 1976.

[48] J. Arons, R. I. Klein, and S. M. Lea, "Radiation Gas Dynamics of Polar CAP Accretion onto Magnetized Neutron Stars: Basic Theory," *The Astrophyiscal Journal*, vol. 312, p. 666, Jan. 1987.

[49] A. K. Harding and D. Lai, "Physics of strongly magnetized neutron stars," *Reports on Progress in Physics*, vol. 69, pp. 2631–2708, Sept. 2006.

[50] P. A. Becker and M. T. Wolff, "Thermal and Bulk Comptonization in Accretion-powered X-Ray Pulsars," *The Astrophysical Journal*, vol. 654, pp. 435–457, Jan. 2007.

[51] D. Mukherjee, D. Bhattacharya, and A. Mignone, "MHD instabilities in accretion mounds - I. 2D axisymmetric simulations," *Monthly Notices of the Royal Astronomical Society*, vol. 430, pp. 1976–1987, Apr. 2013.

[52] K. A. Postnov, M. I. Gornostaev, D. Klochkov, E. Laplace, V. V. Lukin, and N. I. Shakura, "On the dependence of the X-ray continuum variations with luminosity in accreting X-ray pulsars," *Monthly Notices of the Royal Astronomical Society*, vol. 452, pp. 1601–1611, Sept. 2015.

[53] W. A. Heindl, R. E. Rothschild, W. Coburn, R. Staubert, J. Wilms, I. Kreykenbohm, and P. Kretschmar, "Timing and Spectroscopy of Accreting X-ray Pulsars: the State of Cyclotron Line Studies," in *X-ray Timing 2003: Rossi and Beyond* (P. Kaaret, F. K. Lamb, and J. H. Swank, eds.), vol. 714 of *American Institute of Physics Conference Series*, pp. 323–330, AIP, July 2004.

[54] O. Nishimura, "Formation Mechanism for Broad and Shallow Profiles of Cyclotron Lines in Accreting X-Ray Pulsars," *The Astrophysical Journal*, vol. 672, pp. 1127–1136, Jan. 2008.

[55] D. Mukherjee, D. Bhattacharya, and A. Mignone, "MHD instabilities in accretion mounds - II. 3D simulations," *Monthly Notices of the Royal Astronomical Society*, vol. 435, pp. 718–727, Oct. 2013.

[56] "HEASARC: NASA's Archive of Data on Energetic Phenomena." HEASARC. https://heasarc.gsfc.nasa.gov/. (accessed Jun. 21, 2025).

[57] "Gamma Ray Astrophysics at the NSSTC." gammaray.nsstc.nasa.gov. https://gammaray.nsstc.nasa.gov/gbm/science/pulsars.html. (accessed Jun. 21, 2025).

[58] "Swift/BAT Hard X-ray Transient Monitor." Swift/BAT Hard X-ray Transient Monitor. https://swift.gsfc.nasa.gov/results/transients, 2025. (accessed Jun. 21, 2025).

[59] K. C. Gendreau, Z. Arzoumanian, P. W. Adkins, C. L. Albert, J. F. Anders, A. T. Aylward, C. L. Baker, E. R. Balsamo, W. A. Bamford, S. S. Benegalrao, and et al., "The Neutron star Interior Composition Explorer (NICER): design and development," in *Space Telescopes and Instrumentation 2016: Ultraviolet to Gamma Ray* (J.-W. A. den Herder, T. Takahashi, and M. Bautz, eds.), vol. 9905 of *Society of Photo-Optical Instrumentation Engineers (SPIE) Conference Series*, p. 99051H, July 2016.

[60] "nicerl2 HEADAS help file." HEASARC. https://heasarc.gsfc.nasa.gov/lheasoft/help/nicerl2.html, 2024. (accessed Jun. 21, 2025).

[61] "nimaketime HEADAS help file." HEASARC. https://heasarc.gsfc.nasa.gov/lheasoft/help/nimaketime.html, 2024. (accessed Jun. 21, 2025).

[62] K. Jahoda, J. H. Swank, A. B. Giles, M. J. Stark, T. Strohmayer, W. Zhang, and E. H. Morgan, "In-orbit performance and calibration of the Rossi X-ray Timing Explorer (RXTE) Proportional Counter Array (PCA)," in *EUV, X-Ray, and Gamma-Ray Instrumentation for Astronomy VII* (O. H. Siegmund and M. A. Gummin, eds.), vol. 2808 of *Society of Photo-Optical Instrumentation Engineers (SPIE) Conference Series*, pp. 59–70, Oct. 1996.

[63] A. M. Levine, H. Bradt, W. Cui, J. G. Jernigan, E. H. Morgan, R. Remillard, R. E. Shirey, and D. A. Smith, "First Results from the All-Sky Monitor on the Rossi X-Ray Timing Explorer," *The Astrophysical Journal Letters*, vol. 469, p. L33, Sept. 1996.

[64] W. B. Atwood, A. A. Abdo, M. Ackermann, W. Althouse, B. Anderson, M. Axelsson, L. Baldini, J. Ballet, D. L. Band, G. Barbiellini, and et al., "The Large Area Telescope on the Fermi Gamma-Ray Space Telescope Mission," *The Astrophysical Journal*, vol. 697, pp. 1071–1102, June 2009.

[65] C. Meegan, G. Lichti, P. N. Bhat, E. Bissaldi, M. S. Briggs, V. Connaughton, R. Diehl, G. Fishman, J. Greiner, A. S. Hoover, and et al., "The Fermi Gamma-ray Burst Monitor," *The Astrophysical Journal*, vol. 702, pp. 791–804, Sept. 2009.

[66] D. N. Burrows, J. E. Hill, J. A. Nousek, J. A. Kennea, A. Wells, J. P. Osborne, A. F. Abbey, A. Beardmore, K. Mukerjee, A. D. T. Short, and et al., "The Swift X-Ray Telescope," *Space Science Reviews*, vol. 120, pp. 165–195, Oct. 2005.

[67] P. W. A. Roming, T. E. Kennedy, K. O. Mason, J. A. Nousek, L. Ahr, R. E. Bingham, P. S. Broos, M. J. Carter, B. K. Hancock, H. E. Huckle, and et al., "The Swift Ultra-Violet/Optical Telescope," *Space Science Reviews*, vol. 120, pp. 95–142, Oct. 2005.

[68] H. A. Krimm, S. T. Holland, R. H. D. Corbet, A. B. Pearlman, P. Romano, J. A. Kennea, J. S. Bloom, S. D. Barthelmy, W. H. Baumgartner, J. R. Cummings, and et al., "The Swift/BAT Hard X-Ray Transient Monitor," *The Astrophysical Journal Supplement Series*, vol. 209, p. 14, Nov. 2013.

[69] J. E. Deeter and P. E. Boynton, "Uses of the harmonic representation in pulse timing," in *Inuyama Workshop on timing analysis of X-ray sources* (S. Hayakawa and F. Nagase, ed.), p. 29, Jan. 1985.

[70] C. Malacaria, P. Jenke, O. J. Roberts, C. A. Wilson-Hodge, W. H. Cleveland, B. Mailyan, and GBM Accreting Pulsars Program Team, "The Ups and Downs of Accreting X-Ray Pulsars: Decade-long Observations with the Fermi Gamma-Ray Burst Monitor," *The Astrophysical Journal*, vol. 896, p. 90, June 2020.

[71] M. H. Finger, R. B. Wilson, and D. Chakrabarty, "Reappearance of the X-ray binary pulsar 2S 1417-624.," *Astronomy and Astrophysics Supplement Series*, vol. 120, pp. 209–212, Dec. 1996.

[72] D. K. Galloway, E. H. Morgan, and A. M. Levine, "A Frequency Glitch in an Accreting Pulsar," *The Astrophysical Journal*, vol. 613, pp. 1164–1172, Oct. 2004.

[73] M. M. Serim, Ö. C. Özüdoğru, Ç. K. Dönmez, Ş. Şahiner, D. Serim, A. Baykal, and S. Ç. İnam, "Timing and spectral analysis of 2S 1417-624 during its 2018 outburst," *Monthly Notices of the Royal Astronomical Society*, vol. 510, pp. 1438–1449, Feb. 2022.

[74] "Swift J0243.6+6124." SIMBAD. https://simbad.u-strasbg.fr/simbad/sim-id?Ident=Swift+J0243.6%2B6124. (accessed Jun. 21, 2025).

[75] S. B. Cenko, S. D. Barthelmy, P. D'Avanzo, J. A. Kennea, A. Y. Lien, F. E. Marshall, D. M. Palmer, M. H. Siegel, and A. Tohuvavohu, "GRB 171003A: Swift detection of a burst or a Galactic Transient.," *GRB Coordinates Network*, vol. 21960, p. 1, Jan. 2017.

[76] J. A. Kennea, A. Y. Lien, H. A. Krimm, S. B. Cenko, and M. H. Siegel,

"Swift J0243.6+6124: Swift discovery of an accreting NS transient," *The Astronomer's Telegram*, vol. 10809, p. 1, Oct. 2017.

[77] J. van den Eijnden, N. Degenaar, T. Russell, R. Wijnands, J. V. Hernandez Santisteban, G. Sivakoff, C. Heinke, J. Miller-Jones, A. Bahramian, T. Maccarone, and et al., "VLA radio detection of the newly discovered transient and super-Eddington X-ray pulsar Swift J0243.6+6124," *The Astronomer's Telegram*, vol. 10946, p. 1, Nov. 2017.

[78] G. K. Jaisawal, S. Naik, and J. Chenevez, "Understanding the spectral and timing behaviour of a newly discovered transient X-ray pulsar Swift J0243.6+6124," *Monthly Notices of the Royal Astronomical Society*, vol. 474, pp. 4432–4437, Mar. 2018.

[79] S. S. Tsygankov, V. Doroshenko, A. A. Mushtukov, A. A. Lutovinov, and J. Poutanen, "On the magnetic field of the first Galactic ultraluminous X-ray pulsar Swift J0243.6+6124," *Monthly Notices of the Royal Astronomical Society*, vol. 479, pp. L134–L138, Sept. 2018.

[80] J. van den Eijnden, N. Degenaar, T. D. Russell, R. Wijnands, J. C. A. Miller-Jones, G. R. Sivakoff, and J. V. Hernández Santisteban, "An evolving jet from a strongly magnetized accreting X-ray pulsar," *Nature*, vol. 562, pp. 233–235, Sept. 2018.

[81] C. A. Wilson-Hodge, C. Malacaria, P. A. Jenke, G. K. Jaisawal, M. Kerr, M. T. Wolff, Z. Arzoumanian, D. Chakrabarty, J. P. Doty, K. C. Gendreau, and et al., "NICER and Fermi GBM Observations of the First Galactic Ultraluminous X-Ray Pulsar Swift J0243.6+6124," *The Astrophysical Journal*, vol. 863, p. 9, Aug. 2018.

[82] L. Tao, H. Feng, S. Zhang, Q. Bu, S. Zhang, J. Qu, and Y. Zhang, "Super-Eddington Accretion onto the Galactic Ultraluminous X-Ray Pulsar Swift J0243.6+6124," *The Astrophysical Journal*, vol. 873, p. 19, Mar. 2019.

[83] V. Doroshenko, S. N. Zhang, A. Santangelo, L. Ji, S. Tsygankov, A. Mushtukov, L. J. Qu, S. Zhang, M. Y. Ge, Y. P. Chen, and et al., "Hot disc of the Swift

J0243.6+6124 revealed by Insight-HXMT," *Monthly Notices of the Royal Astronomical Society*, vol. 491, pp. 1857–1867, Jan. 2020.

[84] L. D. Kong, S. Zhang, Y. P. Chen, S. N. Zhang, L. Ji, V. Doroshenko, P. J. Wang, L. Tao, M. Y. Ge, C. Z. Liu, and et al., "Two Complete Spectral Transitions of Swift J0243.6+6124 Observed by Insight-HXMT," *The Astrophysical Journal*, vol. 902, p. 18, Oct. 2020.

[85] L.-D. Kong, S. Zhang, S.-N. Zhang, L. Ji, V. Doroshenko, A. Santangelo, Y.-P. Chen, F.-J. Lu, M.-Y. Ge, P.-J. Wang, and et al., "Insight-HXMT Discovery of the Highest-energy CRSF from the First Galactic Ultraluminous X-Ray Pulsar Swift J0243.6+6124," *The Astrophysical Journal*, vol. 933, p. L3, July 2022.

[86] M. Sugizaki, M. Oeda, N. Kawai, T. Mihara, K. Makishima, and M. Nakajima, "X-Ray Emission Evolution of the Galactic Ultraluminous X-Ray Pulsar Swift J0243.6+6124 during the 2017-2018 Outburst Observed by the MAXI GSC," *The Astrophysical Journal*, vol. 896, p. 124, June 2020.

[87] P. J. Wang, L. D. Kong, S. Zhang, Y. P. Chen, S. N. Zhang, J. L. Qu, L. Ji, L. Tao, M. Y. Ge, F. J. Lu, and et al., "Insight-HXMT observations of Swift J0243.6+6124: the evolution of RMS pulse fractions at super-Eddington luminosity," *Monthly Notices of the Royal Astronomical Society*, vol. 497, pp. 5498–5506, Oct. 2020.

[88] S. D. Bykov, M. R. Gilfanov, S. S. Tsygankov, and E. V. Filippova, "ULX pulsar Swift J0243.6+6124 observations with NuSTAR: dominance of reflected emission in the super-Eddington state," *Monthly Notices of the Royal Astronomical Society*, vol. 516, pp. 1601–1611, Oct. 2022.

[89] W. Liu, J. Yan, P. Reig, X. Wang, G. Xiao, H. Lin, X. Zhang, H. Sai, Z. Chen, S. Yan, and Q. Liu, "Multiwavelength observations of Swift J0243.6+6124 from 2017 to 2022," *Astronomy and Astrophysics*, vol. 666, p. A110, Oct. 2022.

[90] K. Kouroubatzakis, P. Reig, J. Andrews, and A. Zezas, "The optical counterpart to the new accreting pulsar Swift J0243.6+6124 is a Be star," *The Astronomer's Telegram*, vol. 10822, p. 1, Oct. 2017.

[91] V. Doroshenko, S. Tsygankov, and A. Santangelo, "Orbit and intrinsic spin-up of the newly discovered transient X-ray pulsar Swift J0243.6+6124," *Astronomy and Astrophysics*, vol. 613, p. A19, May 2018.

[92] I. Bikmaev, V. Shimansky, E. Irtuganov, M. Glushkov, N. Sakhibullin, I. Khamitov, R. Burenin, A. Lutovinov, I. Zaznobin, M. Pavlinsky, and et al., "Determination of the distance to SWIFT J0243.6+6124," *The Astronomer's Telegram*, vol. 10968, p. 1, Nov. 2017.

[93] Y. Zhang, M. Ge, L. Song, S. Zhang, J. Qu, S. Zhang, V. Doroshenko, L. Tao, L. Ji, C. Güngör, and et al., "Insight-HXMT Observations of Swift J0243.6+6124 during Its 2017-2018 Outburst," *The Astrophysical Journal*, vol. 879, p. 61, July 2019.

[94] C. A. L. Bailer-Jones, J. Rybizki, M. Fouesneau, G. Mantelet, and R. Andrae, "Estimating Distance from Parallaxes. IV. Distances to 1.33 Billion Stars in Gaia Data Release 2," *The Astronomical Journal*, vol. 156, p. 58, Aug. 2018.

[95] Gaia Collaboration, A. G. A. Brown, A. Vallenari, T. Prusti, J. H. J. de Bruijne, C. Babusiaux, M. Biermann, O. L. Creevey, D. W. Evans, L. Eyer, and et al., "Gaia Early Data Release 3. Summary of the contents and survey properties," *Astronomy and Astrophysics*, vol. 649, p. A1, May 2021.

[96] C. A. L. Bailer-Jones, J. Rybizki, M. Fouesneau, M. Demleitner, and R. Andrae, "Estimating Distances from Parallaxes. V. Geometric and Photogeometric Distances to 1.47 Billion Stars in Gaia Early Data Release 3," *The Astronomical Journal*, vol. 161, p. 147, Mar. 2021.

[97] K. Setoguchi, H. Negoro, M. Nakajima, K. Kobayashi, M. Tanaka, Y. Soejima, T. Mihara, T. Kawamuro, S. Yamada, T. Tamagawa, and et al., "MAXI/GSC detection of a new X-ray brightening from Swift J0243.6+6124, LS I +61 303, or a new X-ray transient MAXI J0242+611," *The Astronomer's Telegram*, vol. 15983, p. 1, Apr. 2023.

[98] M. Ng, A. Sanna, D. Chakrabarty, C. Malacaria, G. K. Jaisawal, P. Pradhan, J. B. Coley, M. T. Wolff, S. Guillot, Z. Arzoumanian, and et al., "NICER

Detects Pulsations from Swift J0243.6+6124," *The Astronomer's Telegram*, vol. 15987, p. 1, Apr. 2023.

[99] P. Pradhan, S. Pike, J. B. Coley, K. Pottschmidt, C. Malacaria, M. Ng, G. K. Jaisawal, A. R. Escorial, and P. Kretschma, "NuSTAR looks at Swift J0243.6+6124 during the rise of the 2023 outburst," *The Astronomer's Telegram*, vol. 16139, p. 1, July 2023.

[100] J. Poutanen, S. S. Tsygankov, V. Doroshenko, S. V. Forsblom, P. Jenke, P. Kaaret, A. V. Berdyugin, D. Blinov, V. Kravtsov, I. Liodakis, and et al., "Studying geometry of the ultraluminous X-ray pulsar Swift J0243.6+6124 using X-ray and optical polarimetry," *Astronomy and Astrophysics*, vol. 691, p. A123, Nov. 2024.

[101] "Swift J0243.6+6124." Gamma Ray Astrophysics at the NSSTC. https://gammaray.nsstc.nasa.gov/gbm/science/pulsars/lightcurves/swiftj0243.html, 2025. (accessed Jun. 21, 2025).

[102] "Scaled Map Transient Analysis for Swift J0243.6+6124." Swift/BAT Hard X-ray Transient Monitor. https://swift.gsfc.nasa.gov/results/transients/weak/SwiftJ0243.6p6124, 2025. (accessed Jun. 21, 2025).

[103] Z. Acuner, S. Ç. İnam, Ş. Şahiner, M. M. Serim, A. Baykal, and J. Swank, "Timing studies of X Persei and the discovery of its transient quasi-periodic oscillation feature," *Monthly Notices of the Royal Astronomical Society*, vol. 444, pp. 457–465, Oct. 2014.

[104] D. Çerri-Serim, M. M. Serim, Ş. Şahiner, S. Ç. İnam, and A. Baykal, "Pulse frequency fluctuations of magnetars," *Monthly Notices of the Royal Astronomical Society*, vol. 485, pp. 2–12, May 2019.

[105] "MXB 0656-072." SIMBAD. https://simbad.u-strasbg.fr/simbad/sim-id?Ident=MXB+0656-072. (accessed Jun. 21, 2025).

[106] G. W. Clark, G. D. Schmidt, and J. R. P. Angel, "MX0656-07," *International Astronomical Union Circulars*, vol. 2843, p. 1, Oct. 1975.

[107] L. J. Kaluzienski, "MX0656-07," *International Astronomical Union Circulars*, vol. 2935, p. 5, Apr. 1976.

[108] L. Cominsky, C. Jones, W. Forman, and H. Tananbaum, "Transient X-ray sources in the galactic plane.," *The Astrophysical Journal*, vol. 224, pp. 46–52, Aug. 1978.

[109] Q. Z. Liu, J. van Paradijs, and E. P. J. van den Heuvel, "A catalogue of low-mass X-ray binaries," *Astronomy and Astrophysics*, vol. 368, pp. 1021–1054, Mar. 2001.

[110] R. Remillard and F. Marshall, "New Outburst in Recurrent X-ray transient (MX0656-072 = XTEJ0658-073)," *The Astronomer's Telegram*, vol. 197, p. 1, Oct. 2003.

[111] E. Morgan, R. Remillard, and J. Swank, "XTEJ0658-073 (=MX0656-072) is a Pulsar," *The Astronomer's Telegram*, vol. 199, p. 1, Oct. 2003.

[112] M. W. Pakull, C. Motch, and I. Negueruela, "Be star counterpart of X-ray pulsar MX0656-072," *The Astronomer's Telegram*, vol. 202, p. 1, Oct. 2003.

[113] V. A. McBride, J. Wilms, M. J. Coe, I. Kreykenbohm, R. E. Rothschild, W. Coburn, J. L. Galache, P. Kretschmar, W. R. T. Edge, and R. Staubert, "Study of the cyclotron feature in MXB 0656-072," *Astronomy and Astrophysics*, vol. 451, pp. 267–272, May 2006.

[114] W. Heindl, W. Coburn, I. Kreykenbohm, and J. Wilms, "Cyclotron Line in XTE J0658-073," *The Astronomer's Telegram*, vol. 200, p. 1, Oct. 2003.

[115] I. Kreykenbohm, S. E. Shaw, V. Bianchin, R. Diehl, S. Brandt, M. Mas-Hesse, A. Parmar, W. Hermsen, and R. Krivonos, "INTEGRAL detects a new outburst of MXB 0656-072," *The Astronomer's Telegram*, vol. 1281, p. 1, Nov. 2007.

[116] K. Pottschmidt, V. A. McBride, S. Suchy, I. Kreykenbohm, J. Wilms, R. E. Rothschild, P. Kretschmar, G. Schoenherr, I. Caballero, E. Kendziorra, and et al., "RXTE observations of MXB 0656-072," *The Astronomer's Telegram*, vol. 1283, p. 1, Nov. 2007.

[117] J. A. Kennea, P. Romano, K. Pottschmidt, J. Wilms, J. Cummings, P. Evans, and D. N. Burrows, "Swift and RXTE observations of MXB 0656-072," *The Astronomer's Telegram*, vol. 1293, p. 1, Nov. 2007.

[118] D. N. Burrows, J. R. Cummings, G. Cusumano, C. Guidorzi, S. T. Holland, J. A. Kennea, H. A. Krimm, V. Mangano, F. E. Marshall, A. Moretti, and et al., "Swift detection of MXB 0656-072.," *GRB Coordinates Network*, vol. 7097, p. 1, Jan. 2007.

[119] "MXB 0656-072." Gamma Ray Astrophysics at the NSSTC. https://gammaray.nsstc.nasa.gov/gbm/science/pulsars/lightcurves/mxb0656.html, 2025. (accessed Jun. 21, 2025).

[120] J. Yan, J. A. Zurita Heras, S. Chaty, H. Li, and Q. Liu, "Multi-wavelength Study of the Be/X-Ray Binary MXB 0656-072," *The Astrophysical Journal*, vol. 753, p. 73, July 2012.

[121] "XSPEC Models." HEASARC. https://heasarc.gsfc.nasa.gov/docs/xanadu/xspec/manual/node128.html, 2025. (accessed Jun. 21, 2025).

[122] E. Nespoli, P. Reig, and A. Zezas, "New insights into the Be/X-ray binary system MXB 0656-072," *Astronomy and Astrophysics*, vol. 547, p. A103, Nov. 2012.

[123] S. S. Tsygankov, R. Wijnands, A. A. Lutovinov, N. Degenaar, and J. Poutanen, "The X-ray properties of Be/X-ray pulsars in quiescence," *Monthly Notices of the Royal Astronomical Society*, vol. 470, pp. 126–141, Sept. 2017.

[124] G. Raman, Varun, P. Pradhan, and J. Kennea, "Quiet, but not silent: uncovering quiescent state properties of two transient high-mass X-ray binaries," *Monthly Notices of the Royal Astronomical Society*, vol. 526, pp. 3262–3272, Dec. 2023.

[125] D. A. Leahy, W. Darbro, R. F. Elsner, M. C. Weisskopf, P. G. Sutherland, S. Kahn, and J. E. Grindlay, "On searches for pulsed emission with application to four globular cluster X-ray sources : NGC 1851, 6441, 6624 and 6712.," *The Astrophysical Journal*, vol. 266, pp. 160–170, Mar. 1983.

[126] Y. M. Wang, "On the Torque Exerted by a Magnetically Threaded Accretion Disk," *The Astrophysical Journal Letters*, vol. 449, p. L153, Aug. 1995.

[127] E. Bozzo, L. Stella, M. Vietri, and P. Ghosh, "Can disk-magnetosphere interaction models and beat frequency models for quasi-periodic oscillation in accreting X-ray pulsars be reconciled?," *Astronomy and Astrophysics*, vol. 493, pp. 809–818, Jan. 2009.

[128] M. T. Stollberg, M. H. Finger, R. B. Wilson, B. A. Harmon, B. C. Rubin, N. S. Zhang, and G. J. Fishman, "GRO J1008-57," *International Astronomical Union Circulars*, vol. 5836, p. 1, July 1993.

[129] "GRO J1008-57." SIMBAD. https://simbad.u-strasbg.fr/simbad/sim-id?Ident=GRO+J1008-57. (accessed Jun. 21, 2025).

[130] M. J. Coe, P. Roche, C. Everall, J. Fabregat, D. A. Buckley, R. C. Smith, A. P. Reynolds, I. D. Jupp, and H. T. MacGillivray, "Discovery of the optical counterpart to the CGRO transient GRO J1008-57.," *Monthly Notices of the Royal Astronomical Society*, vol. 270, pp. L57–L61, Oct. 1994.

[131] M. J. Coe, A. J. Bird, A. B. Hill, V. A. McBride, M. Schurch, J. Galache, C. A. Wilson, M. Finger, D. A. Buckley, and E. Romero-Colmenero, "Now you see it, now you don't - the circumstellar disc in the GRO J1008-57 system," *Monthly Notices of the Royal Astronomical Society*, vol. 378, pp. 1427–1433, July 2007.

[132] "GRO J1008-57." Gamma Ray Astrophysics at the NSSTC. https://gammaray.nsstc.nasa.gov/gbm/science/pulsars/lightcurves/groj1008.html, 2025. (accessed Jun. 21, 2025).

[133] M. Kühnel, S. Müller, I. Kreykenbohm, F. Fürst, K. Pottschmidt, R. E. Rothschild, I. Caballero, V. Grinberg, G. Schönherr, C. Shrader, and et al., "GRO J1008-57: an (almost) predictable transient X-ray binary," *Astronomy and Astrophysics*, vol. 555, p. A95, July 2013.

[134] J. E. Grove, J. D. Kurfess, B. F. Phlips, M. S. Strickman, and M. P. Ulmer, "OSSE Observations Spectra of X-Ray Pulsars," in *International Cosmic Ray Conference*, vol. 2 of *International Cosmic Ray Conference*, p. 1, Jan. 1995.

[135] T. Yamamoto, T. Mihara, M. Sugizaki, M. Nakajima, K. Makishima, and M. Sasano, "Firm detection of a cyclotron resonance feature with Suzaku in

the X-ray spectrum of GRO J1008-57 during a giant outburst in 2012," *Publications of the Astronomical Society of Japan*, vol. 66, p. 59, June 2014.

[136] E. C. Bellm, F. Fürst, K. Pottschmidt, J. A. Tomsick, S. E. Boggs, D. Chakrabarty, F. E. Christensen, W. W. Craig, C. J. Hailey, F. A. Harrison, and et al., "Confirmation of a High Magnetic Field in GRO J1008-57," *The Astrophysical Journal*, vol. 792, p. 108, Sept. 2014.

[137] M. Y. Ge, L. Ji, S. N. Zhang, A. Santangelo, C. Z. Liu, V. Doroshenko, R. Staubert, J. L. Qu, S. Zhang, F. J. Lu, and et al., "Insight-HXMT Firm Detection of the Highest-energy Fundamental Cyclotron Resonance Scattering Feature in the Spectrum of GRO J1008-57," *The Astrophysical Journal Letters*, vol. 899, p. L19, Aug. 2020.

[138] D. J. Macomb, C. R. Shrader, and A. B. Schultz, "An EXOSAT Detection of the Transient X-Ray Pulsar GRO J1008-57," *The Astrophysical Journal*, vol. 437, p. 845, Dec. 1994.

[139] M. S. Riquelme, J. M. Torrejón, and I. Negueruela, "Circumstellar emission in Be/X-ray binaries of the Magellanic Clouds and the Milky Way," *Astronomy and Astrophysics*, vol. 539, p. A114, Mar. 2012.

[140] F. Fortin, F. García, S. Chaty, E. Chassande-Mottin, and A. Simaz Bunzel, "Constraints to neutron-star kicks in high-mass X-ray binaries with Gaia EDR3," *Astronomy and Astrophysics*, vol. 665, p. A31, Sept. 2022.

[141] W. Wang, Y. M. Tang, Y. L. Tuo, P. R. Epili, S. N. Zhang, L. M. Song, F. J. Lu, J. L. Qu, S. Zhang, M. Y. Ge, and et al., "Accretion torque reversals in GRO J1008-57 revealed by Insight-HXMT," *Journal of High Energy Astrophysics*, vol. 30, pp. 1–8, June 2021.

[142] S. S. Tsygankov, V. Doroshenko, A. A. Mushtukov, J. Poutanen, A. Di Marco, J. Heyl, F. La Monaca, S. V. Forsblom, C. Malacaria, H. L. Marshall, and et al., "X-ray pulsar GRO J1008−57 as an orthogonal rotator," *Astronomy and Astrophysics*, vol. 675, p. A48, July 2023.

[143] S. S. Tsygankov, A. A. Mushtukov, V. F. Suleimanov, V. Doroshenko, P. K. Abolmasov, A. A. Lutovinov, and J. Poutanen, "Stable accretion from a

cold disc in highly magnetized neutron stars," *Astronomy and Astrophysics*, vol. 608, p. A17, Nov. 2017.

[144] "Scaled Map Transient Analysis for GRO J1008-57." Swift/BAT Hard X-ray Transient Monitor. https://swift.gsfc.nasa.gov/results/transients/GROJ1008-57, 2025. (accessed Jun. 21, 2025).

[145] L. Ji, V. Doroshenko, A. Santangelo, C. Güngör, S. Zhang, L. Ducci, S. N. Zhang, M. Y. Ge, L. J. Qu, Y. P. Chen, and et al., "Timing analysis of 2S 1417-624 observed with NICER and Insight-HXMT," *Monthly Notices of the Royal Astronomical Society*, vol. 491, pp. 1851–1856, Jan. 2020.

[146] M. Kühnel, F. Fürst, K. Pottschmidt, I. Kreykenbohm, R. Ballhausen, S. Falkner, R. E. Rothschild, D. Klochkov, and J. Wilms, "Evidence for different accretion regimes in GRO J1008-57," *Astronomy and Astrophysics*, vol. 607, p. A88, Nov. 2017.

[147] M. Revnivtsev and S. Mereghetti, "Magnetic Fields of Neutron Stars in X-Ray Binaries," *Space Science Reviews*, vol. 191, pp. 293–314, Oct. 2015.

[148] S. Yeole, D. Mukherjee, and A. Mandal, "Investigating field burial by magnetically confined accretion mounds on Neutron Stars," *arXiv e-prints*, p. arXiv:2507.08509, July 2025.

APPENDIX

A Lists of Observations Used

The following tables list the observations used for each source, including their IDs, times and exposures.

Table A.1: The list of NICER/XTI observations of Swift J0243.6+6124 used in this thesis.

Obs. ID	Time (MJD)	Exp. (s)	Obs. ID	Time (MJD)	Exp. (s)
1050390101	58029.737	2657	1050390126	58098.901	120
1050390102	58030.868	3819	1050390127	58099.173	751
1050390103	58031.000	19389	1050390128	58100.573	341
1050390104	58032.029	21788	1050390129	58106.359	623
1050390105	58037.054	2518	1050390130	58107.905	491
1050390106	58038.525	36	1050390131	58108.226	638
1050390107	58042.380	450	1050390132	58125.639	220
1050390108	58047.203	880	1050390133	58126.489	990
1050390109	58048.039	2067	1050390134	58127.257	5384
1050390110	58049.005	772	1050390135	58128.097	3173
1050390111	58050.229	709	1050390136	58128.995	3324
1050390112	58051.132	1001	1050390137	58130.092	4582
1050390113	58058.117	3406	1050390138	58135.744	3258
1050390114	58063.983	245	1050390139	58145.699	2148
1050390115	58064.055	1282	1050390140	58151.311	2126
1050390116	58065.084	3052	1050390141	58162.110	3520
1050390117	58071.256	24	1050390142	58166.037	2802
1050390118	58072.678	420	1050390143	58169.884	1983
1050390119	58073.067	3936	1050390144	58175.811	2122
1050390120	58074.029	3962	1050390145	58176.004	7050
1050390121	58074.604	1638	1050390146	58181.857	1469
1050390122	58089.393	3832	1050390147	58202.238	1251
1050390123	58091.131	1313	1050390148	58204.606	1705
1050390124	58092.160	1766	1050390149	58217.662	5003
1050390125	58093.262	1913	1050390150	58218.107	2025

Continued on next page

Table A.1 – Continued from previous page

Obs. ID	Time (MJD)	Exp. (s)	Obs. ID	Time (MJD)	Exp. (s)
1050390151	58219.528	2278	1050390191	58369.045	7780
1050390152	58220.043	1606	1050390192	58370.656	737
1050390153	58221.970	500	1050390193	58372.778	1810
1050390154	58222.034	19208	1050390194	58373.036	3868
1050390155	58223.007	14521	1050390195	58374.001	1837
1050390156	58224.037	7735	1050390196	58375.029	1827
1050390157	58224.999	5955	1050390197	58375.998	3882
1050390158	58228.088	2785	1050390198	58377.866	393
1050390159	58231.951	492	1050390199	58378.897	228
1050390160	58232.381	643	1050390201	58379.025	2730
1050390161	58303.065	2723	1050390202	58380.163	2389
1050390162	58304.141	1387	1050390203	58381.778	503
1050390163	58305.442	735	1050390204	58383.197	202
1050390164	58306.407	2453	1050390205	58386.983	3080
1050390165	58307.112	7300	1050390206	58388.206	1461
1050390166	58308.009	3881	1050390207	58389.427	575
1050390167	58311.425	602	1050390208	58391.163	407
1050390168	58313.098	2357	1050390209	58392.643	1752
1050390169	58317.206	1495	1050390210	58393.157	3218
1050390170	58322.813	2220	1050390211	58393.995	7454
1050390171	58323.008	3405	1050390212	58397.146	255
1050390172	58325.565	4351	1050390213	58408.657	608
1050390173	58326.079	3788	1050390214	58410.001	1536
1050390174	58327.181	1526	1050390215	58411.098	1740
1050390175	58328.142	1889	1050390216	58412.451	2012
1050390176	58331.493	2214	1050390217	58414.193	83
1050390177	58333.667	746	1050390218	58418.164	1442
1050390178	58337.603	505	1050390219	58419.454	1551
1050390179	58339.319	64	1050390220	58420.548	879
1050390180	58344.025	3943	1050390221	58421.956	2108
1050390181	58350.580	4653	1050390222	58422.919	2145
1050390182	58351.932	1089	1050390223	58425.815	4417
1050390183	58351.997	2328	1050390224	58426.799	821
1050390184	58356.310	1567	1050390225	58427.250	1346
1050390185	58357.404	758	1050390226	58429.502	1890
1050390186	58358.682	2735	1050390227	58430.016	4704
1050390187	58360.226	1435	1050390228	58432.902	2413
1050390188	58363.649	2613	1050390229	58435.938	153
1050390189	58366.025	2757	1050390230	58436.002	967
1050390190	58368.597	3857	1050390231	58437.350	3655

Continued on next page

Table A.1 – Continued from previous page

Obs. ID	Time (MJD)	Exp. (s)	Obs. ID	Time (MJD)	Exp. (s)
1050390232	58438.442	908	1050390261	58495.399	2271
1050390233	58443.262	1405	1050390262	58496.107	4435
1050390234	58444.282	2190	1050390263	58497.795	1069
1050390235	58448.333	2320	1050390264	58498.616	2305
1050390236	58449.492	2305	1050390265	58499.323	4494
1050390237	58451.936	1655	1050390266	58500.417	2253
1050390238	58452.515	3450	1050390267	58501.905	1371
1050390239	58457.725	4521	1050390268	58502.034	5170
1050390240	58459.204	2754	1050390269	58503.836	1669
1050390241	58460.427	1318	1050390270	58505.306	2283
1050390242	58461.005	740	1050390271	58506.658	1509
1050390243	58462.035	794	1050390272	58507.050	4973
1050390244	58466.291	6288	1050390273	58509.040	2891
1050390245	58470.406	961	1050390274	58510.005	1264
1050390246	58471.178	3156	1050390275	58511.358	1719
1050390247	58472.335	1666	1050390276	58512.262	1669
1050390248	58473.226	2867	1050390277	58513.361	1638
1050390249	58474.454	1446	1050390278	58514.132	1771
1050390250	58475.417	105	1050390279	58515.159	2988
1050390251	58476.513	393	1050390280	58516.120	2958
1050390252	58479.130	414	1050390281	58517.216	2621
1050390253	58487.551	1676	1050390282	58520.063	136
1050390254	58488.196	2525	1050390283	58521.399	5092
1050390255	58489.416	1392	1050390284	58524.750	2503
1050390256	58490.188	4155	1050390285	58525.651	2992
1050390257	58491.475	2105	1050390286	58526.166	1004
1050390258	58492.183	4346	1050390287	58528.092	2279
1050390259	58493.739	1000	1050390288	58529.900	1744
1050390260	58494.564	3221	1050390289	58532.019	1781

Table A.2: The list of RXTE/PCA observations of MXB 0656–072 used in this thesis.

Obs. ID	Time (MJD)	Exp. (s)	Obs. ID	Time (MJD)	Exp. (s)
93032-15-01-00	54418.237	667	93032-15-03-03	54427.727	2927
93032-15-01-01	54419.493	958	93032-15-03-00	54428.985	1753
93032-15-02-00	54420.935	1563	93032-15-03-08	54430.106	1364
93032-15-02-01	54422.969	931	93032-15-03-07	54430.414	3326
93032-15-02-02	54424.857	2438	93032-15-03-06	54430.490	12654
93032-15-02-03	54426.446	883	93032-15-03-01	54431.018	1681

Continued on next page

Table A.2 – Continued from previous page

Obs. ID	Time (MJD)	Exp. (s)	Obs. ID	Time (MJD)	Exp. (s)
93032-15-03-02	54431.656	3382	93423-01-07-03	54496.513	3527
93032-15-03-05	54432.381	2796	93423-01-08-00	54498.542	3541
93032-15-03-04	54433.756	666	93423-01-08-01	54501.484	3412
93032-15-04-00	54434.337	13508	93423-01-09-00	54504.561	3438
93032-15-04-01	54434.612	7431	93423-01-09-01	54507.502	1570
93032-15-04-03	54435.319	3409	93423-01-09-02	54510.191	1459
93032-15-04-04	54435.389	3116	93423-01-10-00	54514.050	1163
93032-15-04-05	54435.453	3173	93423-01-10-01	54516.081	817
93032-15-04-02	54435.517	2839	93423-01-11-00	54518.172	1891
93032-15-04-06	54437.106	665	93423-01-11-01	54521.182	1958
93032-15-04-09	54438.609	5390	93423-01-12-00	54525.117	1016
93032-15-04-10	54439.384	6265	93423-01-12-01	54528.863	549
93032-15-04-11	54439.523	2192	93423-01-12-02	54531.064	1340
93032-15-04-12	54439.707	3012	93423-01-13-00	54532.509	2568
93032-15-04-13	54439.978	2169	93423-01-13-01	54534.474	2485
93032-15-04-14	54440.301	12702	93423-01-13-02	54536.435	2907
93032-15-04-15	54440.621	10345	93423-01-13-03	54538.464	2813
93032-15-04-16	54440.891	2511	93423-01-14-00	54540.307	2171
93032-15-05-00	54444.032	939	93032-15-06-00	54542.252	10282
93032-15-05-01	54446.975	2432	93423-01-14-01	54542.588	1937
93032-15-05-04	54447.975	1619	93032-15-07-00	54546.245	10005
93423-01-01-00	54449.142	1631	93032-15-07-01	54548.275	10024
93423-01-01-01	54451.944	2105	93423-01-15-00	54550.369	1120
93423-01-01-02	54454.828	2343	93423-01-16-00	54553.375	2111
93423-01-02-01	54461.760	1924	93423-01-16-02	54555.998	1645
93423-01-03-00	54462.550	2811	93423-01-16-03	54556.451	942
93423-01-03-01	54463.468	1917	93423-01-16-01	54559.989	471
93423-01-03-02	54466.735	4600	93423-01-17-00	54560.000	1018
93423-01-03-03	54468.431	2542	93423-01-17-01	54564.308	3306
93423-01-04-00	54472.431	1055	93423-01-17-02	54565.748	739
93423-01-04-01	54475.780	1695	93423-01-17-03	54566.925	1194
93423-01-05-00	54476.226	921	93423-01-18-00	54568.888	1075
93423-01-05-01	54479.298	1452	93423-01-18-01	54571.900	1003
93423-01-05-02	54482.644	1854	93423-01-19-00	54575.431	946
93423-01-06-00	54485.791	1719	93423-01-19-01	54577.134	1970
93423-01-06-02	54486.907	922	93423-01-19-02	54579.949	1677
93423-01-06-01	54489.982	971	93423-01-20-00	54583.286	2475
93423-01-07-01	54490.000	834	93423-01-20-01	54586.229	3365
93423-01-07-00	54491.467	3450	93423-01-21-00	54589.303	910
93423-01-07-02	54493.496	3467	93423-01-21-01	54592.183	849

Continued on next page

Table A.2 – Continued from previous page

Obs. ID	Time (MJD)	Exp. (s)	Obs. ID	Time (MJD)	Exp. (s)
93423-01-21-02	54594.211	1449	93423-01-32-01	54683.144	1384
93423-01-22-00	54596.305	966	93423-01-32-02	54685.897	1933
93423-01-22-01	54598.468	1135	93423-01-33-00	54687.975	1300
93423-01-22-02	54600.298	1117	93423-01-33-01	54689.229	2201
93423-01-23-00	54602.023	478	93423-01-34-00	54693.286	2266
93423-01-23-01	54604.247	1701	93423-01-34-01	54697.273	1238
93423-01-23-02	54606.181	1674	93423-01-35-00	54700.614	1426
93423-01-23-03	54608.805	1572	93423-01-35-01	54703.967	1025
93423-01-24-00	54610.768	1392	93423-01-36-00	54708.531	594
93423-01-24-02	54612.734	724	93423-01-36-01	54712.065	1125
93423-01-24-01	54615.806	1213	93423-01-37-00	54715.808	783
93423-01-25-00	54618.951	1401	93423-01-37-01	54720.633	925
93423-01-25-01	54622.088	981	93423-01-38-00	54722.665	921
93423-01-26-00	54625.441	957	93423-01-38-01	54725.615	498
93423-01-26-01	54629.837	682	93423-01-39-00	54728.552	1151
93032-30-01-01	54632.094	4463	93423-01-39-01	54731.581	896
93032-30-01-02	54632.235	1122	93423-01-39-02	54734.890	1022
93032-30-01-03	54632.831	5292	93423-01-40-00	54737.059	889
93032-30-01-04	54632.948	1477	93423-01-40-01	54740.203	917
93032-30-01-05	54634.262	2037	93423-01-40-02	54741.964	1374
93032-30-01-06	54634.337	1317	93423-01-41-02	54743.691	565
93032-30-01-07	54635.040	4935	93423-01-41-03	54743.757	419
93032-30-01-00	54635.755	28666	93423-01-41-00	54745.035	1373
93423-01-28-00	54638.118	1752	93423-01-41-04	54745.948	841
93423-01-28-01	54640.997	6871	93423-01-41-05	54746.795	1274
93423-01-28-03	54642.105	6238	93423-01-41-01	54747.662	1624
93423-01-28-02	54643.314	1172	93032-30-02-00	54748.627	14108
93423-01-27-03	54644.138	3214	93423-01-42-00	54749.807	1743
93423-01-27-00	54645.115	9057	93423-01-42-01	54752.883	1787
93423-01-27-01	54646.034	10139	93423-01-42-02	54754.061	642
93423-01-27-02	54647.150	3282	93423-01-43-00	54759.879	866
93423-01-27-04	54647.946	1683	93423-01-43-01	54762.795	500
93423-01-29-00	54662.063	3429	93423-01-44-00	54765.445	1487
93423-01-29-01	54664.814	2052	93423-01-44-01	54768.603	891
93423-01-30-00	54665.728	1626	93423-01-45-00	54772.995	1076
93423-01-30-01	54668.812	1284	93423-01-45-01	54776.566	1322
93423-01-30-02	54671.821	1331	93423-01-46-00	54779.863	839
93423-01-31-00	54674.249	970	93423-01-46-01	54782.454	1082
93423-01-31-01	54678.943	1222	93423-01-47-00	54788.895	966
93423-01-32-00	54680.735	1119			

Table A.3: The list of NICER/XTI observations of GRO J1008–57 used in this thesis.

Obs. ID	Time (MJD)	Exp. (s)	Obs. ID	Time (MJD)	Exp. (s)
3034050101	58947.529	526	3034050124	58989.976	10608
3034050102	58948.867	1701	3034050125	58991.023	7999
3034050103	58949.783	625	3034050126	58992.042	11715
3034050104	58950.802	1243	3034050127	58993.012	7274
3034050105	58951.126	950	3034050128	58994.052	5618
3034050106	58953.191	2314	3034050129	58995.077	650
3034050107	58955.709	1182	3034050130	58996.505	463
3034050108	58957.580	1917	3034050131	58997.018	62
3034050109	58959.645	1388	3034050132	59002.090	2939
3034050110	58961.196	1619	3034050133	59002.994	3816
3034050111	58963.259	1667	3034050134	59004.093	2516
3034050112	58965.066	1445	3034050135	59005.062	1215
3034050113	58967.004	2018	3034050136	59006.031	937
3034050114	58977.222	2067	3034050137	59007.130	1565
3034050115	58978.892	1294	3034050138	59008.355	728
3034050116	58979.227	175	3034050139	59010.341	3581
3034050117	58981.021	1701	3034050140	59011.759	1382
3034050118	58983.003	2335	3034050141	59012.018	1183
3034050119	58985.003	9102	3034050142	59018.152	744
3034050120	58986.186	5689	3034050143	59020.220	1313
3034050121	58987.003	14810	3034050144	59022.092	715
3034050122	58988.041	13330	3034050145	59024.593	603
3034050123	58989.007	11860	3034050146	59026.465	1623

CURRICULUM VITAE

PERSONAL INFORMATION

Surname, Name: Dönmez, Çağatay Kerem

EDUCATION

Degree	Institution	Grad. Year
PhD	Department of Physics, METU	2025
M.S.	Department of Physics, METU	2019
B.S.	Dept. of Electrical and Electronics Eng., Bilkent Univ.	2015

WORK EXPERIENCE

Year	Place	Enrollment
2019–ongoing	Department of Physics, METU	Teaching Assistant
2017–2019	Department of Physics, METU	Student Assistant

LANGUAGES

English (advanced), Spanish (pre-intermediate)

PUBLICATIONS

1. *Pulse frequency variations and timing noise of MXB 0656-072 during the type I outbursts in 2007–2008 and implication of its magnetic field*

   Serim M. M., Serim D., Dönmez Ç. K., Tuo Y., Ducci L., Baykal A., Santangelo A., *Astronomy and Astrophysics*, 690, A5

2. *Timing analysis of Swift J0243.6+6124 with NICER and Fermi/GBM during the decay phase of the 2017–2018 outburst*

   Serim M. M., Dönmez Ç. K., Serim D., Ducci L., Baykal A., Santangelo A., *Monthly Notices of Royal Astronomical Society*, 522, 6115

3. *Timing and spectral analysis of 2S 1417-624 during its 2018 outburst*

   Serim M. M., Özüdoğru Ö. C., Dönmez Ç. K., Şahiner Ş., Serim D., Baykal A., İnam S. Ç., *Monthly Notices of Royal Astronomical Society*, 510, 1438

4. *Comprehensive analysis of the transient X-ray pulsar MAXI J1409-619*

   Dönmez Ç. K., Serim M. M., İnam S. Ç., Şahiner Ş., Serim D., Baykal A., *Monthly Notices of Royal Astronomical Society*, 496, 1768